POLITECNICO DI TORINO

Master's Degree in Aerospace Engineering

Low Thrust, Minimum-Propellant Optimization for Multi-Orbit Rendezvous with Uncooperative LEO Space Debris using Indirect Methods

Supervisor:

Prof. Manuela BATTIPEDE

Co-Supervisor:

Dr. Luigi MASCOLO

Author:

Christian CARONE

Academic Year 2023/24

To my loving parents and my dear brother.

Summary

Since the beginning of space exploration, thousands of satellites have been launched into Earth orbit. Over the years, however, the increasing number of artificial satellites placed in orbit has been matched by an increase in the probability of collisions between the satellites themselves. Such events would produce orbiting fragments, each of which would exponentially increase the probability of further collisions occurring in the future. The criticality of the Kessler Syndrome, acknowledged by researchers since the 1980s, has led to the formation of a space debris belt around Earth, particularly in Low Earth Orbits (LEO) below 2000 km.
This creates a severe threat to both the safety and functionality of space assets, as collisions with space debris can cause substantial damage or complete destruction of spacecraft; in recent decades, therefore, mission disposal operations have increasingly become relevant. Notably congested regions include the Sun-Synchronous Orbits (SSO) and Polar Orbits (PEO) at altitudes of 600-1200 km and inclinations of 80-105 degrees, particularly around 800-900 km. These orbits, critical for Earth observation, necessitate effective debris removal solutions for non-functional or undesirable objects.

This paper proposes evaluating an optimal trajectory for a Space Debris Removal (SDR) mission utilizing electric propulsion (EP) to remove debris from such orbits. The indirect method is well suited for very high accuracy in solving the optimal EP trajectories, exploiting the Pontryagin's minimum Principle and ensuring minimum-propellant expenditure through the extremization of the Hamiltonian and the application of bang-bang control. An essential aspect of SDR missions is the capability for controlled de-orbit and re-entry into the Earth's atmosphere within 25 years, according to current space regulations.
The mission is divided into two key phases: 1) a propulsive phase, where the spacecraft transitions from an initial parking orbit to the targeted debris using low-thrust EP arcs, and 2) a de-orbiting phase, which involves a controlled spiral descent and re-entry into Earth's atmosphere at an altitude of 100 km, utilizing the remaining propellant with the throttle set at 10%.

The dynamic model is based on the two-body problem, accommodating additional perturbations such as Earth's non-sphericity and atmospheric drag during the de-orbiting phase.

Contents

List of Figures

List of Tables

Acronyms

$\mathcal{S}_F$	Switching Function
2BP	2 Body Problem
ADR	Active Debris Removal
BCs	Boundary Conditions
BVP	Boundary Value Problem
COCPs	Continous Optimal Control Problems
CoV	Calculus of Variations
DCM	Direction Cosine Matrix
DRAMA	Debris Risk Assessment and Mitigation Analysis
ECEF	Earth-Centred Earth-Fixed
ECI	Earth-Centred Inertial
EME2000	Earth Mean Equator and Equinox of Epoch J2000
ESA	European Space Agency
GEO	Geostationary Earth Orbit
HBVP	Hamiltonian Boundary Value Problem
IADC	Inter-Agency Space Debris Committee
ISS	International Spce Station
KKT	Karush-Kuhn-Tucker
LEO	Low Earth Orbit

MMOD	Micrometeorids and Orbital Debris
MPBVP	Multi Point Boundary Values Problem
NASA	National Aeronautics and Space Administration
NL	Non-Linear
NLP	Non Linear Programming
OCP	Optimal Control Problem
OCT	Optimal Control Theory
ODE	Ordinary Differential Equation
PMP	Pontryagin's Maximum Principle
PmP	Pontryagin's minimum Principle
RAAN	Right Ascension of the Ascending Node
RF	Reference Frame
SATCAT	(SATellite CATalog
SDWG	Space Debris Working Group
SSO	Sun-Synchronous Orbit
TPBVP	Two Point Boundary Value Problem
Vega	Vettore Europeo di Generazione Avanzata
VESPA	Vega Secondary Payload Adapter
VNC	Velocity-Normal-Conormal
ZEN	Zenit-East-North

Chapter 1

Introduction

> *There are places where litter is acceptable, and others where is not.*
>
> Alice Gorman

1.1 Preface

In the collective imaginary, the epic vision of a spacecraft forced to avoid dangerous asteroids to achieve a specific mission objective is an indelible icon associated with space and movies about it.

Cinephiles with *sci-fi* passion will undoubtedly recall such episodes in various films or sagas devoted to adventures among the stars and planets. In *Passengers*, Jennifer Lawrence and Chris Patt awaken from cryogenic sleep ninety years earlier than expected due to the impact of their spaceship with a meteor shower field; in *Gravity*, the protagonists find themselves in a race against time to get back into their spacecraft before a wave of debris, caused by the chain destruction of some satellites, overtakes them. Memorable, then, are the scenes in *Star Trek* in which the *Enterprise* goes to great lengths to avoid debris and meteorites with extreme maneuvers. Although such scenes take one's breath away upon viewing them, a competent viewer can look beyond the mere cinematic representation, as one is aware that space travel is not exempt from real dangers of this kind.

Indeed, coming back to reality, it is clear how the topic of space debris is of paramount importance in today's frontier of space exploration and, unfortunately, still too underestimated. In the minds of the average population, the idea of the space race over the past seventy years, from the moon landing onward, might seem almost like science fiction. However, for those who enjoy this discipline and study its history, it is evident that modern technological limitations place today's spacecraft in an unequal comparison with the *Enterprise*'s maneuvering capabilities and performance. Similarly, if our beloved astronauts on the International Spce Station (ISS) were to face a debris storm, it would be in the best interest of all of us to prevent them from drifting into the solar system like Commander Kowalsky played by George Clooney.

So, the conquest of space, though often portrayed in epic narratives, is not devoid of real and serious challenges: testimony to this, aided by Hollywood filmography, is the fact that the most famous phrase in space travel, even now is probably:

"Houston, we have a problem !"

Thus, the presence of such Micrometeorids and Orbital Debris (MMOD), whose dangerousness has been repeatedly demonstrated, is a constant and insidious threat to space missions, both present and future. In this introduction, an attempt will not only be made to characterize this phenomenon but the crucial importance of their monitoring and possible management will be explored, an issue that, if neglected, could jeopardize not only space missions *per se* but also the understanding and advancement of knowledge of the universe around us.

1.2 Optimization concept in space missions

Throughout the space programs, optimization has been the keystone, an art that has proven to be as simple as incredibly elegant. Reflecting on how such concepts fit into the context of a mission of any kind to space leads to the discovery of an extraordinary symphony of precision and vision.

In the Golden Era of the space race in the 1960s and 1970s, one name stands out with unquestioned mastery: the *dominus aevi* Wernher Von Braun (figure 1.1)[1], the one who indelibly branded that epoch. German engineer by profession, he emerged as one of the leading figures in the development of rocketry during the period of Nazi Germany, being the designer of the V2 rockets that bombed London during World War II. At the end of the conflict, the Americans and Russians successfully managed to reach the Peenemünde research center where he was located and gain possession of Nazi knowledge. Along with 1,600 other engineers and scientists, Von Braun and his team were deported to America and recruited by the government through the secret Operation Paperclip, a program whose purpose was to give the U.S. military an advantage over the Soviet one in the Cold War and the space race (the Russians responded similarly with Operation Osoaviachim). After arriving at

---

[1] Source: Cortright, Edgar M., ed. *Apollo expeditions to the Moon.* Vol. 10. Scientific and Technical Information Office, National Aeronautics and Space Administration, 1975, page 43.

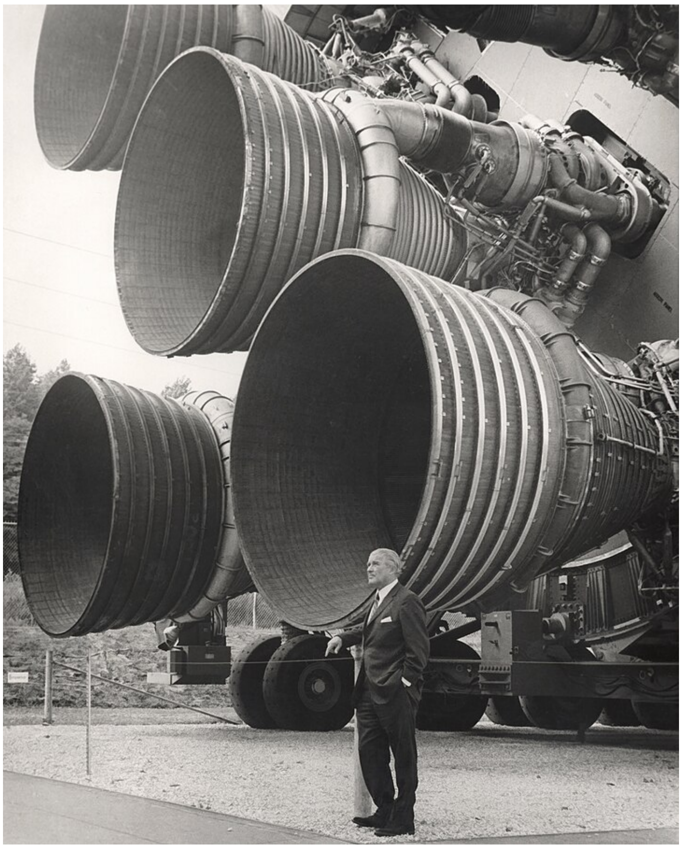

Figure 1.1: Dr. Wernher Von Braun standing next to one of the five engines at the after end of the Saturn V vehicle's first stage.

National Aeronautics and Space Administration (NASA), he was destined to make history with the design and development of the Saturn V, the launcher that took the Apollo missions to the Moon, the true crowning glory of all his scientific work.

If Von Braun, then, is the one who best identifies the idea of the space mission and scientific revolution that has enabled mankind to arrive at the successes of today, the link between him and the elementary concepts of *optimization* is personified by the personage of Konstantin Ėduardovič Tsiolkovsky (figure 1.2)[2]. Counted among the most brilliant Russian minds of all time and as one of the greatest geniuses in scientific history, he is regarded as the father of spaceflight and a pioneer of astronautics, a field in which he theorized several aspects in advance. The distinctive formula for which he is remembered, and which precisely carries

---

[2] Source: Photographer Feodosius Andronikovich Chmil, catalog *Photo documents about the life and work of K.E. Tsiolkovsky*, Kaluga, "Golden Alley", 2004, p.92-93.

Figure 1.2: K.E. Tsiolkovsky in his office looking through magazines.

the name *Tsiolkvsky's equation* (but also called the *rocket equation*), is the one that links the mass of propellant required by the spacecraft to accomplish a specific mission with the change in velocity Δv that must be carried out by the engine:

$$\Delta v = c \ln\left(\frac{m_0}{m_f}\right) \Longleftrightarrow \frac{m_f}{m_0} = e^{-\frac{\Delta v}{c}} \tag{1.1}$$

with $m_p = m_0 - m_f = m_0(1 - e^{-\frac{\Delta v}{c}})$ mass of propellant expended and $c = I_{sp} \cdot g_0$ effective discharge velocity, assumed constant to obtain the (1.1) and a function of sea-level gravitational acceleration g_0 and specific impulse I_{sp}[3]. The latter is a measure of how effectively the thruster is utilizing the propellant. Consequently, it is clear that, in a mission, one always tries to maximize this parameter because it will mean that the same useful effect can be achieved with less expense (or, dually, a larger effect can be gained with the same propellant).

Thus, one can see how, from this simple and elegant expression, it is possible to derive the first requirements to be fulfilled during a space mission. Of course, the I_{sp} cannot grow at will, but it is necessary to take into account the technological and performance limitations of the various existing classes of thrusters, of which the major ones are seen below:

- chemical propulsion, although it can release a large amount of energy in a short time and is an easily scalable solution, has the primary drawback of

---

[3] Dimensionally it is a time, and from a physical point of view, it can be interpreted as the time in which an assigned mass of propellant can provide thrust equal to its weight at sea level.

having a moderately limited specific impulse. This is because the energy used for acceleration is contained within the propellant and is, therefore, limited by the choice of the same.

Currently, the best combination is the oxygen and cryogenic hydrogen reagents for a liquid rocket engine, with an $I_{sp} = 300 - 450\ \text{s}$;

- in electric propulsion, by contrast, the energy source is separated from the propellant and developed using a generator, which will require a certain amount of power delivered by an electrothermal, electrostatic, or solar panel generation system. Consequently, the I_{sp} is considerably higher in orders between $200 - 1000\ \text{s}$, up to $5000\ \text{s}$ and even beyond, thus being able to use less propellant for the same mission. However, from the expression of the effective discharge velocity in the case of electric propulsion:

$$c = \frac{2\eta P_E}{T} = \sqrt{\frac{2\eta P_E}{\dot{m}_p}} \tag{1.2}$$

  Where η is the efficiency denoting the fraction of thermal power developed. From the equation, one can observe how, wanting to reduce the thrust T to maximize I_{sp}, the same Δv will require longer times, going from accelerations obtained in the order of seconds and minutes to hours, days, or even weeks. In addition, the power generator has a certain weight, bulk, and cost, so it cannot be as large as desired (to achieve high P_E), imposing another limitation. Moreover, since that class of propulsion has thrust-to-weight ratios that are too low to allow takeoff (a rocket would require P_E in the GigaWatt range, which would be impossible to provide with simple solar panels, but nuclear generators would be needed, which are banned for environmental issues), the chemical counterpart is the only one currently used to make the ascent into orbit.

It is clear how a simple expression such as (1.1) goes to significantly constrains the requirements of a space mission. In the present thesis, electric propulsion will take the lead, and the primary objective will be the maximization of the final spacecraft mass m_f or, conversely, minimizing the amount of propellant consumed.

From the above, an optimization problem that can maximize the m_f fixed initial mass m_0 of the spacecraft must be solved.

This goal will be pursued through the use of a numerical method. In general, for boundary value problems of this type, two different approaches have historically been used: direct and indirect methods. Without going into too much detail, for the sake of brevity, in general, it can be said that indirect methods describe the system with a set of differential equations with assigned boundary conditions exploiting the principles of variational calculus (calculus that deals with the search for and analysis of maxima and minima of functions whose, in turn, is a set of functions). They introduce, in fact, a state vector and optimize the control variables by changing their initial values. Then, the resulting problem is based on the calculus of variations, and the optimal control law is formulated as a boundary problem at the initial and final points. This approach requires the addition of certain variables, called Lagrange multipliers (or co-state variables) equal in number to the state variables and evolving along with the associated vector.

On the other hand, direct methods reduce the optimal control problem to a parameter optimization one, dividing the trajectory into many shorter arcs/steps. In this way, the solution of the system equations is obtained by integrating them in each step but making the computational calculation very time-consuming. Such methods, by the way, cannot be used for an orbital transfer problem, or rather, they can be applied only in a few simple cases of little practical interest due to the simplifications involved. The use of the indirect strategy for the optimal problem, by contrast, allows high numerical accuracy and important theoretical content, but they require high specificity and a solid background of knowledge for those who use them.

A much more in-depth and comprehensive comparison is given in section (3.1).

1.3 Space Debris: population and mitigation

As could be understood from the preface, the conceptual core of this thesis concerns the sensitive topic of MMODs and the key concepts involved in terms of the problems and variety of methodologies to deal with it.

Consequently, it is incumbent in this context to reserve a section dedicated to this topic, as it is crucial for fully appreciating the value and potential of the work produced, grasping its full significance and any implications that may arise from it within the scientific community.

1.3.1 What are space debris and why are they a problem?

Since the dawn of the space age in the 1950s, the various missions conducted by humans beyond the Earth's atmosphere have followed one another over time to the present day in a wide variety of purposes and goals. The story of each of them can be told in a thousand different ways: from the political and military background surrounding space events to the great failures that cost the lives of brave men, to the objects of the time (e.g., newspapers or postage stamps) to show how society received the exploits of spaceships that plied the skies. The downside that is too often not addressed, however, is that the more than 70 years of space launches and activities have led to an accumulating amount of anthropogenic objects orbiting the Earth ranging from non-operational craf to smaller materials, including, for example, discarded camera lens camp or propellant fuel. Let it be specified how the term *micrometeeroid* refers to natural objects (metorites, dusts, comet pieces), while *space debris* means any man-made object in space, which does not now, nor in the foreseeable future, serve a useful purpose: from here on, only the latter will be discussed.

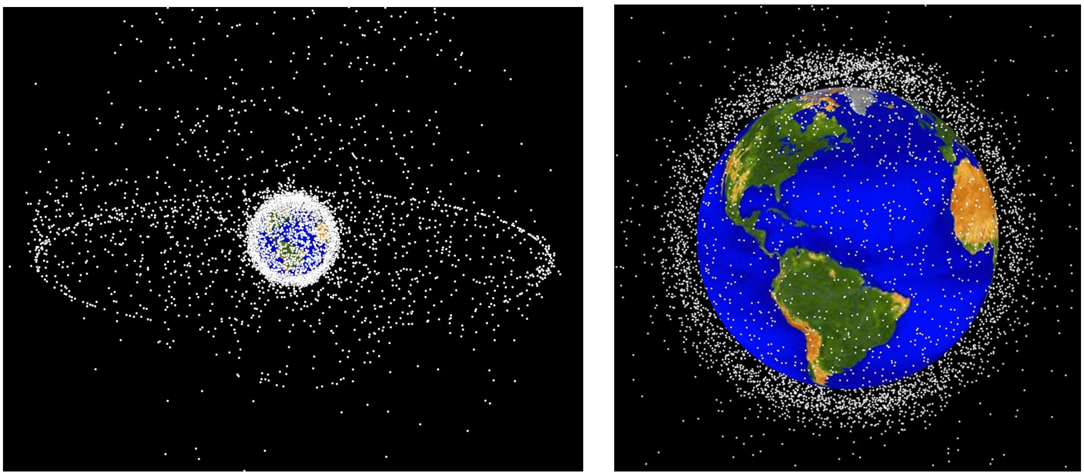

Figure 1.3: A computer-generated image depicting the population and distribution of space debris around Earth. Note the detail of the LEO object cloud on the right.

From figure (1.3)[4] it can be seen that in addition to a kind of envelope around the Earth, there is also an assemblage of waste on the Geostationary Earth Orbit (GEO), characterized mainly by old satellites or fragments of them. Such an area is not of interest here. The subject site of study where debris is most troublesome is Low Earth Orbit (LEO)[5], where there is a significant risk of impact with objects orbiting at very high speeds. In detail, Sun-Synchronous Orbit (SSO) will be of interest, and the reasons for this will be addressed later.

So, as one can clearly understand, the tragedy of debris in space is becoming more and more evident as the years go by, unfortunately, and this can lead to devastating consequences. Indeed, when such debris should reach a density such that the probability of impact is higher than the likelihood of no impact/avoidance, all space activities will be prevented. This cascading effect is known as *Kessler's*

---

[4] Source: NASA image, *Astromaterials Research* & *Exploration Science NASA ORBITAL DEBRIS PROGRAM OFFICE*, photo gallery.

[5] A LEO orbit is, as the name suggests, an orbit that is relatively close to Earth's surface. It is normally at an altitude of less than 1000 km but could be as low as 160 km above Earth.

syndrome, named after the first scientist who became interested in calculating the *critical population density.* Upon reaching such a condition, fragment numbers will increase exponentially due to mutual collisions, even without adding new objects through launches. Analyses indicate that in some densely populated regions, the critical density is only about 2 to 3 times the current population [**1**].

Thus, it is essential to study the phenomenon to comprehend it thoroughly, to understand how to intervene through the proper techniques and procedures to make sure that this critical situation is not reached in any orbital belt around our planet, as will be briefly explained in the next section (1.3.2).

1.3.2 Debris Mitigation: strategies and policy

Considering the previous problems inherent in the space debris phenomenon, it seems clear that this global problem can only be effectively solved by international cooperation. Firstly, it is useful to understand how the critical issue can be addressed: broadly speaking, three strategies that either mitigate debris generation and/or adapt to collision risk are defined to follow.

- *shielding*: typically aimed at mitigating impact with debris, representing design features in spacecraft (such as reinforcement with stronger materials) that reduce both own damage risk and debris generation in collisions. A well-known example is the protective shield called *Whipple Shields* covering the exterior of the ISS, which absorbs the energy of an impact with debris. Such a shielding system, however, is effective for protection from particles less than 1 cm in diameter and also belongs to passive techniques, so it is not of interest to this thesis.

- *graveyarding capability*: which enhances the possibility of safely and instantly retiring spent vehicles to a high-altitude orbit (called precisely 'graveyard orbit'). This strategy is not of interest here and, consequently, will not be explored in depth. This is easily guessed for two reasons: first, as one is said to be interested in analyzing debris on SSO orbits and thus, in an altitude range of no more than 1,000 km altitude, it is not feasible to consider resigning the vehicle by taking it to higher altitudes, as it would create problems with functioning satellites operating in their proper orbits. In addition, the work focuses on the so-called *active removal* of space debris, hence the design of special missions using dedicated space cleaning vehicles, where the target debris is to be considered no longer capable of maneuvering or operational functionality.

- *controlled reentry*: will be the removal strategy used in the mission under analysis, as the target debris is placed on a sufficiently low orbit. Therefore, after the first phase of approaching and capturing the decommissioned satellite, it will be followed by a second phase of lowering its altitude to place it into decaying orbit, allowing its controlled reentry into the atmosphere. An overview of current state-of-the-art active technologies and their development status can be found in [**2**] and not reported for the sake of brevity.

The controlled reentry option is also advantageous from a cost-benefit estimation perspective on debris mitigation, as discussed interestingly by M.K. Macauley in [**3**], which further justifies the preference for this option.

Whatever strategy one chooses, it goes without saying that it must be subject to existing policies on debris mitigation. The main problem is that today's international space laws do not explicitly address the space debris issue: in fact, they mainly speak of "*regulations*" of the various International entities, but these do not constitute a *de facto* law and, therefore, may not even be recognized by all, or interpreted differently. Instead, the constitution of space laws dedicated to the topic could undoubtedly benefit the sustainability and management of space, becoming a proper Code of Conduct to be adhered to from the very beginning in the study and feasibility stage of a mission. Driven by these reasons, as early as 1986 the European Space Agency (ESA) created a section specifically dedicated to this objective: the Space Debris Working Group (SDWG) with the mandate to assess the various issues of space debris. The outcome of the work of this research group is briefly summarized in [**4**] and not reported for the sake of brevity. The useful notions to remember are the objectives that ESA's Council decided to adopt in 1989 after receiving the recommendations of the SDWG:

- to minimize the creation of space debris;
- to reduce the risk for manned and unmanned space flight;
- to reduce the risk on the ground due to the re-entry of space objects;
- to acquire data on the debris population as needed for the execution of its programs;
- to study the legal aspects of space debris and, consequently, to approve activity plans.

Pursuing and seeking to enhance these goals, the Space Debris Research Program aims to take action in three main areas: knowledge of the debris and particulate environment on Earth, the risk posed by space debris, and instating preventive and protective measures. One of the most significant rules that ESA has decided to impose toward its member states is the 25-year limit on the presence of debris in LEO, initially proposed in 2007 by the Inter-Agency Space Debris Committee (IADC) Guidelines for Space Debris Mitigation [**5**] and is now adopted by a large number of space agencies around the world, including the NASA. Compliance or non-compliance with this constraint is the discriminating factor on the authorization of a European mission by ESA, which requires that it be in line with this time limit[6]. Hence, at the end of the generic satellite's operational mission, the so-called end-of-life phase takes over, in which one must properly passivate all onboard systems, deplete the residual fuel, and, within 25 years, remove it from the orbit it naturally or artificially occupies. In particular, ESA is considering a mission in this field as part of the *Clean Space* project, within which this thesis work is sought to be placed.

1.4 Motivations and Objectives

The availing of space trajectory optimization and design concepts in this thesis aims to minimize the propellant required to pursue the chosen mission through the use of electric propulsion in a fidelity dynamic model. The selected scenario, as mentioned earlier, will place the focus on the topic of space debris, with particular interest in the SSO region. The reason behind this specific scenario is the result of an integrated assessment of various factors and issues, the matching of which opened a window of analysis that this thesis sought to investigate.

Primarily, the choice to work on the issue of space debris arose from a careful analysis of the current challenges related to it, as previously seen.

Interest in the work done in this thesis stemmed from a desire to contribute to the search for solutions to counter the dangerous trend of the exponential increase of debris in Earth's orbit. This trend has been further fueled by the attention paid to ESA major initiatives in this regard, including *Clean Space*. The tragic nature of the phenomenon is visible from the figure(1.4)[7], with an estimated number of about 36500 debris objects in orbit according to the latest ESA environmental report updated as of December 06, 2023. The major *Clean Space* project aims, therefore, to develop new technologies and new practices to be adopted and implemented to limit the effect of the debris already present, to zero the generation of new ones by future missions, and to try to capture the large debris unfortunately still present in LEO.

---

[6] Actually, in recent years, there are even plans to make this limit more stringent by decreasing the years, both because they are not few and to respond to the rate at which space activity is growing.

[7] Source: ESA Space Debris Office, *ESA's Annual Space Environment Report*, Revision 7.1, September 12, 2023, page 4.

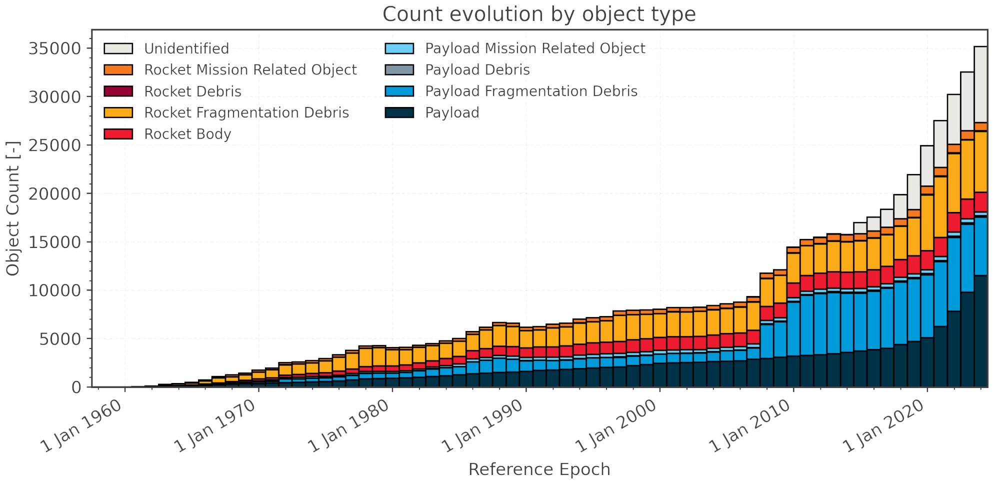

Figure 1.4: Evolution over the years of the taxonomy of objects in the spatial environment done according to debris type.

Precisely, such research falls into the latter branch of in-orbiting servicing, through appropriate Active Debris Removal (ADR) techniques, which can undoubtedly benefit the space environment. Among all the potential areas of intervention around the Earth, this work focuses on the range of LEO orbits, and the reasons for this are presented next.

1.4.1 The situation in Low Earth Orbit (LEO)

The reason for analyzing a debris intervention mission in LEO orbit is perceptible. First, low near-Earth orbits are functional for several purposes: they are the most commonly used for satellite imaging (since proximity to the surface allows for high-resolution images) or for communication purposes through a large combination or constellation of multiple satellites to give a constant coverage. LEO orbit is also used by the ISS since it is easier for astronauts to travel to and from it at a shorter distance. The great potential offered by this range of orbits has long made them the preferred target of the scientific and space community because of their ability to support a wide range of purposes. Moreover, the combination of practicality and speed in positioning satellites at such altitudes still enhances their appeal. The counterbalance to all these advantages is caused by the various decades of launches to such orbits have resulted in a significant accumulation of debris and decommissioned satellites, making this space region dangerously congested and seriously threatening its usability.

This risk is readily apparent by looking at the figure (1.5)[8], which shows not only how densely crowded LEO orbits are, but also that there is an unquestionable and imperative urgency to intervene with immediate actions to counter the phenomenon and attempt to reverse the current trend.

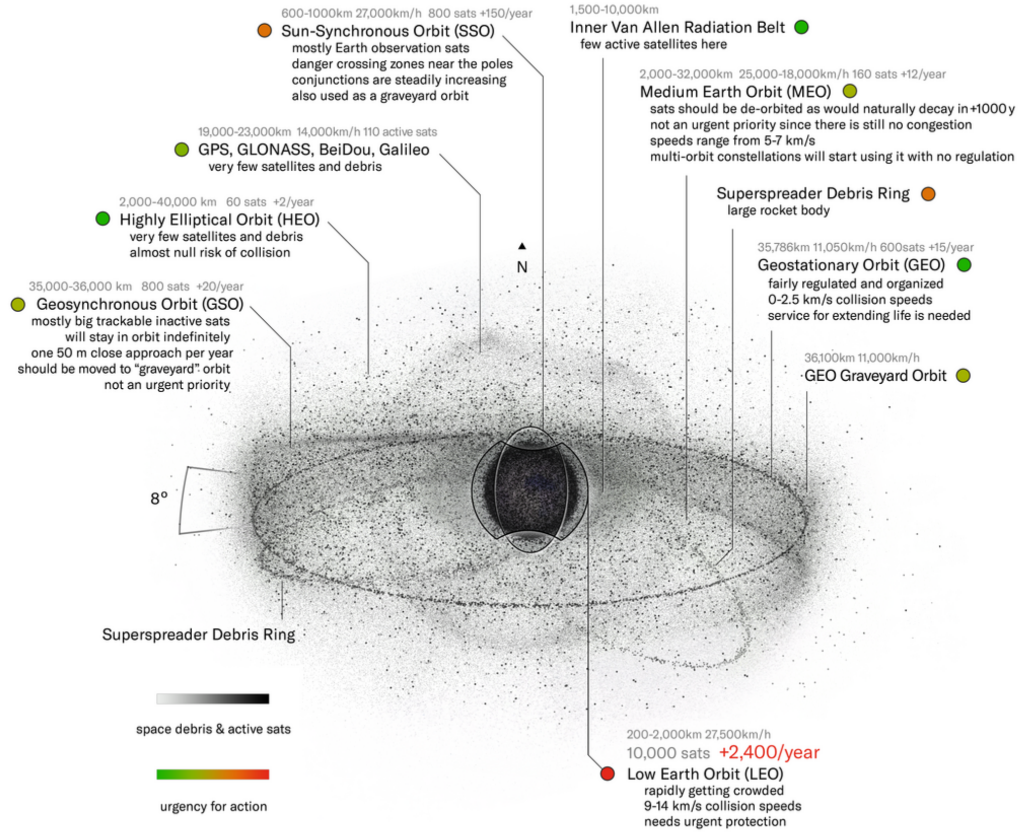

Figure 1.5: Space sustainability urgency in Earth orbits.

The situation, as appreciable in the figure, is also quite critical for SSO orbits. Several studies (e.g., [**6**]) prioritize the altitude region between 600 and 1000 km, where the mass of debris is greater than 50 kg.

In detail, a significant debris peak was detected near the 800 km altitude, with a range of inclination from 98° to 100° (figure 1.6)[9], thus in the region of SSOs,

---

[8] Source: Pablo Carlos Budassi, *An axonometric view displays various Earth orbits, illustrating space debris and active satellites*, Own work for Wikimedia Commons, August 9, 2023.

[9] Source: ESA Space Debris Office, *ESA's Annual Space Environment Report*, Revision 7.1, 12 September 2023, page 58.

which consequently fall among the typical targets for ADR missions proposed by ESA (table intervention regions), according to [**7**].

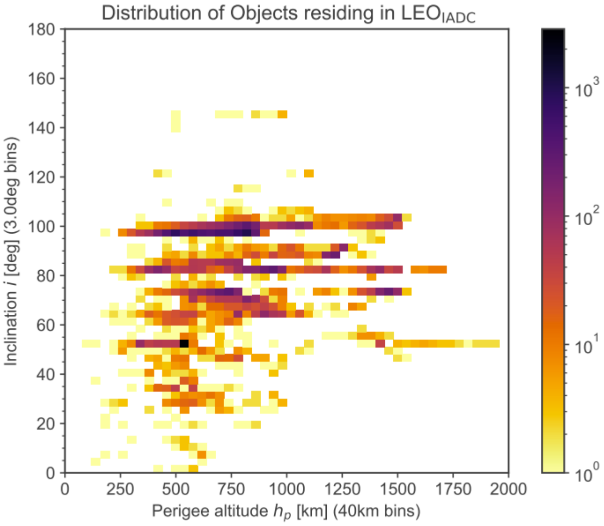

Figure 1.6: Distribution of number of objects residing in LEO as a function of inclination and perigee altitude.

The SSOs are of great interest and are the focus of this thesis work for two main reasons: first, they are extensively used for Earth observation purposes due to their peculiar property of transiting the same point on Earth at the same time of day; second, any maneuver to deorbiting or reducing the operational lifetime of a satellite placed on such an orbit is too expensive to be seriously considered, as accurately described in [**8**].

Table 1.1: ESA Candidates Regions for ADR missions.

Region	*Altitude* [km]		*Inclination*[°]	
	From	*To*	*From*	*To*
1	900	1100	81	83
2	700	900	98	100
3	750	950	70	72
4	650	850	85	87

The second characteristic was the determining factor that gave rise to the mission study presented here: since, once they reach their end of life, satellites in SSO cannot be deorbited for the reason described earlier, the only strategy to remove them is to carry out an ADR mission.

It is in this context, therefore, that this thesis is set. The scenario analyzed is emblematic of a debris removal mission in SSO orbit, articulated in two consequential phases: the first phase involves the transfer of the spacecraft from the starting orbit to the one containing the target debris; subsequently, the second phase will be characterized by deorbit via a lowering of altitude such that reentry into the atmosphere is possible. More specifically, during the analysis of the optimal mission strategy, it turned out to be necessary to further subdivide the first phase into two distinct sub-phases, in which an initial global variation of parameters is followed by a rendezvous with the debris, as will be better discussed in Chapter 5.

In this thesis, the optimization of electric propulsion trajectories is carried out with an indirect method based on the theory of optimal control and transforms the propellant minimization problem into a multipoint boundary value problem. The boundary value problem is then solved with an iterative *single-shooting* procedure based on Newton's method. Specifically, the study belongs to a particular subclass of optimal control law problems called *bang-bang* controls, as will be explained later.

1.5 Dissertation Overview

A brief overview of the main contents of this thesis is summarized below.

Chapter 2 discusses the dynamic model within which the spacecraft will move through time throughout the mission. The main reference systems that were worked with and also how, through appropriate transformations and mathematical steps, it is possible to move from one reference system to another will be discussed. In addition, a summary of the basic concepts of astrodynamics is outlined.

Chapter 3 introduces the optimal control theory that frames the entire work. After a brief introduction to understand the potential of this discipline, there follows a comparison of the principal methods, direct and indirect, by which the problem can be set up; and why, through a comparative analysis of pros and cons, the latter rather than the former has been opted upon. The entire mathematical treatment of optimal control theory and how it can be applied to the topic of space trajectory optimization is then explained. Strategies to comply with the optimality conditions and the fulfillment of Pontryagin's Maximum Principle are here outlined in detail, with a comprehensive discussion regarding thrust strategies, optimal thrust directions, and switching functions.

Chapter 4 presents the debris removal problem that was decided to be tackled, illustrating how it was set up and justifying the choices made in the analysis process. The work done is retraced step by step, from how the implementation of the problem started to the strategies and methodologies used to reach the convergence of the solution.

Chapter 5 analyzes the results obtained from the various simulations, discussing the solution of the optimal trajectory found. Detailed analysis of the switching function defining the optimal thrust phases is performed.

Chapter 6, in conclusion, presents a summary of the most important results achieved and proposes interesting insights on more in-depth studies that could be conducted on some areas of the analyzed mission to improve its prediction and overall accuracy. Finally, it is discussed how the work produced could potentially help future research topics.

Chapter 2

Dynamic model

The following chapter describes the dynamic model implemented to perform the various optimization analyses of the ADR mission trajectory sought. The aim is to provide a sufficiently intelligible overview of the physical and mathematical concepts that form the basis of the applied model. After a brief reminder of the principal reference systems used for the analysis and the transformations that allow switching from one system to another, the 2BP Equations of Motions will be presented, which constitute the heart of this chapter. To improve the fidelity of the model and, consequently, of the outputs it produces, the most relevant perturbative effects within it are also accounted for: the Earth's non-sphericity and atmospheric drag. Basic concepts of celestial mechanics, such as classical orbital elements and some insights into SSO, complete the theoretical background contained in this chapter of the thesis.

2.1 Reference systems

A generic Reference Frame (RF) is uniquely defined by:

- the origin of the system;
- a fundamental plane;
- an orthonormal right-handed triad, with the direction closing the triad perpendicular to the fundamental plane.

RFs defined in this way are generally referred to as detrended systems.

Depending, then, on the analysis a user wishes to perform, it may be convenient to opt for an inertial or a non-inertial RF: the choice of one or the other could have an impact as a benefit on the simplification of the equations of motion describing the system's dynamics. The main discriminator between the two is the presence/absence of additional pseudo-accelerations due to relative motion, such as the Coriolis force or centrifugal acceleration. In an inertial RF, a body moves with uniform or stationary motion in time since no external forces act on it. On the other hand, in a non-inertial RF, a body is subject to external forces that cause it to accelerate/decelerate concerning an inertial reference.

Since this work aims to characterize the motion of bodies orbiting the Earth, opting for an inertial RF proves to be the most appropriate choice, allowing the use of different coordinate systems that benefit the representation of bodies in space. In detail, the three different reference systems used are described below and shown in the figure (2.1)[1].

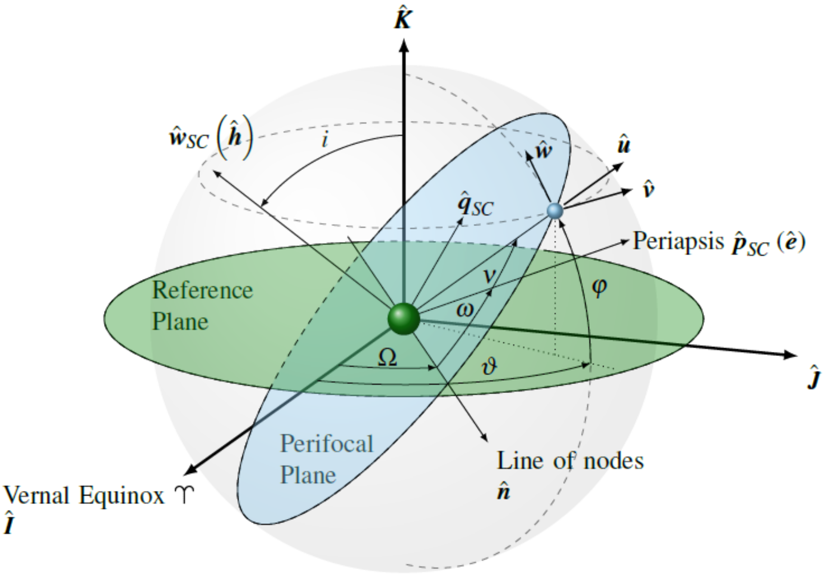

Figure 2.1: EME2000 $\left\{\hat{I}, \hat{J}, \hat{K}\right\}$, perifocal $\{\hat{p}_{SC}, \hat{q}_{SC}, \hat{w}_{SC}\}$, and ZEN $\{\hat{u}, \hat{v}, \hat{w}\}$ RF.

2.1.1 EME2000 RF

In this thesis, the geocentric-equatorial reference system coincides with the Earth Mean Equator and Equinox of Epoch J2000 (EME2000) and is the one generally used for a 2BP. The system is defined as originating in the center of the Earth,

---

[1] Source: Mascolo, Luigi. *Low-Thrust Optimal Escape Trajectories from Lagrangian Points and Quasi-Periodic Orbits in a High-Fidelity Model.* PhD thesis, Diss. Tesi di dott. Torino: Politecnico di Torino, 2023, page 14.

while the fundamental plane corresponds to the equatorial one. Finally, the positive direction of the z-axis that completes the right-hand triad is directed towards the hemisphere containing Polaris (northern hemisphere), as shown in the figure (2.1).

The unit vectors $\left\{\hat{I}, \hat{J}, \hat{K}\right\}$ are defined as follows:

- $\hat{I}$ is aligned with the direction of the Vernal Equinox pointing towards the Aries constellation;
- $\hat{K}$ is perpendicular to the reference plane;
- $\hat{J}$ completes the right-handed triad.

Finally, it is worth specifying how the EME2000 RF represents a specific case of the Earth-Centred Inertial (ECI) RF, which includes the nutation and libration effects of the planet Earth and is generally exploited for the determination of celestial bodies on a global scale in the field of radio astronomical observations. Therefore, the EME2000 RF should be considered as a quasi-inertial reference system. However, since the rotational offset between these two systems is of the order of 0.01 arc second, this difference is neglected, allowing the EME2000 RF to be considered an inertial system.

2.1.2 Perifocal RF

The motion of a satellite around a primary body can be described within the perifocal reference system (2.2)[2]. This system is defined as follows:

- centred origin of the primary gravitational body, i.e. the Earth;
- fundamental plane containing the trajectory of the satellite;
- direction of the z-axis perpendicular to the fundamental plane to complete the right-handed triad.

The triad of unit vectors of this plane $\{\hat{p}_{SC}, \hat{q}_{SC}, \hat{w}_{SC}\}$ is denoted. In the perifocal plane, the unit vector $\hat{p}_{SC}$ is identified as having direction towards the periastrum of the trajectory and parallel to the eccentricity vector $\vec{e}$, while $\hat{q}_{SC}$ is parallel to the direction individuated by the semilatus rectum p of the orbit. Finally, $\hat{w}_{SC}$ is normal to the plane containing $\hat{p}_{SC}$ and $\hat{q}_{SC}$, directed in the direction of the momentum vector $\vec{h}$ completing the right-handed triad.

---

[2] Source: Mascolo, Luigi. *Low-Thrust Optimal Escape Trajectories from Lagrangian Points and Quasi-Periodic Orbits in a High-Fidelity Model.* PhD thesis, Diss. Tesi di dott. Torino: Politecnico di Torino, 2023, page 15.

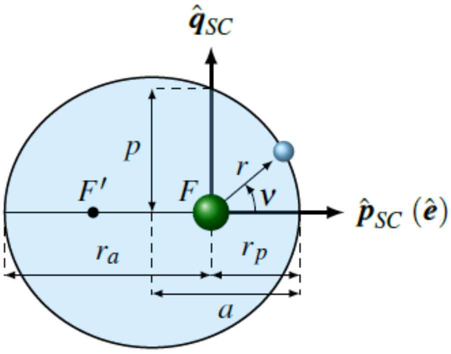

Figure 2.2: Perifocal RF considering an orbit with eccentricity $e = 0.4$.

The perifocal reference system constitutes a crucial support point for carrying out the analyses that allowed to reach the results in this thesis. In fact, during the simulations, it was deemed necessary to implement a switch from the classical orbital parameters used to characterize the initial and final orbits to the Cartesian coordinates used to define the position vectors $\bar{r}$ and velocity $\bar{v}$ of the spacecraft and debris. Given a point on the trajectory and the position vector $\bar{r}$ defined, the angle it forms with the axis of direction p is called the true anomaly ν. Depending on the value of ν, the satellite will be at a specific position in the orbit with a specific velocity:

$$\bar{r} = (r\cos\nu)\hat{p}_{SC} + (r\sin\nu)\hat{q}_{SC} \tag{2.1}$$

$$\bar{v} = (\dot{r}\cos\nu - r\dot{\nu}\sin\nu)\,\hat{p} + (\dot{r}\sin\nu + r\dot{\nu}\cos\nu)\,\hat{q} \tag{2.2}$$

with $\bar{v}$ vector tangent to the trajectory. Using certain concepts and expressions from orbital mechanics, not given here for the sake of brevity, it is possible to redefine the two previous expressions in their respective components as follows:

$$\bar{r}_{pqw} = \left\{ \begin{array}{c} r\cos\nu \\ r\sin\nu \\ 0 \end{array} \right\} \tag{2.3a}$$

$$\bar{v}_{pqw} = \left\{ \begin{array}{c} -\sqrt{\frac{\mu}{p}}\sin\nu \\ \sqrt{\frac{\mu}{p}}(e+\cos\nu) \\ 0 \end{array} \right\} \tag{2.3b}$$

By doing the scalar product, a significant relationship between the two quantities can be derived:

$$r \cdot v = rv\cos(90 - \varphi) = rv\sin(\varphi) \tag{2.4}$$

With φ *flight path angle*[3].

From the relationship obtained, one can essentially observe that ϕ and ν have the same sign, and this helps to understand where the satellite is along the orbit at a generic instant:

- if $rv > 0$, $\varphi > 0$. The flight path angle is positive when the body moves from the periastrum to the apoastro of the orbit, and the same is true for ν;
- If $rv < 0$, $\varphi < 0$. The flight path angle is negative when the body moves from the apoastro to the periastrum of the orbit, and the same is true for ν.

Obviously, the information given so far cannot provide details on the orientation and geometric shape of the orbit contained in the perifocal plane. This task is performed by the classical Keplerian elements $\{a, e, i, \Omega, \omega, \nu\}$, which will be analyzed later in the section (2.4) and which allow an orbit to be univocally characterized in space. In detail, only a subset of these parameters is sufficient for perifocal representation by the conic equation:

$$r = \frac{a(1 - e^2)}{1 + e\cos\nu} \tag{2.5}$$

Where a is the semi-major axis and e is the eccentricity of the conic.

2.1.3 ZEN RF

A third reference system can be defined around the spacecraft orbiting the central body: this is the Zenit-East-North (ZEN) RF. In relation to the figure (2.1) it consists of a triplet of vectors $\{\hat{u}, \hat{v}, \hat{w}\}$ that conventionally indicate the three velocity components of the spacecraft in the radial, tangential, and normal directions, respectively. In particular, this system has:

- origin in the center of mass of the spacecraft;
- radial direction $\hat{u}$ continuing the radius vector from the center of the Earth pointing to the spacecraft;

---

[3] The flight path angle is defined as the angle between the velocity vector and the local horizon. It provides information on how high the velocity vector is in relation to the horizon plane. Its $90 - \varphi$ complement is called the *zenith angle* and tells how much the velocity vector $\bar{v}$ is inclined with respect to the radial direction.

- normal direction $\hat{w}$ exiting the plane swept at that instant by the spacecraft, coincident with the meridian of the celestial sphere;
- tangential direction $\hat{v}$ found with the right-hand rule and coincident with the parallel of the celestial sphere.

It should be carefully specified that none of the velocity components in such a system coincides with or is parallel to the spacecraft's velocity vector, which is tangent to the orbital plane. In essence, such a reference system is not to be confused with the Velocity-Normal-Conormal (VNC) RF[4], with which it coincides only in the case of circular orbits. The use of the ZEN RF is advantageous since it allows for the absence of a velocity phase-shift component: whatever orbit is considered, the tangential velocity $\hat{v}$ and radial velocity $\hat{u}$ remain independent of each other.

2.1.4 Time-invariant coordinate trasformation

This is a very important topic in the field of space flight mechanics in which the geometry of spherical triangles is exploited. It makes it possible to perform a transformation of co-ordinates by projecting them from one initial reference system to another target, allowing the equations describing the dynamics to be simplified. In general, to perform these transformations, matrices composed of a series of elementary Direction Cosine Matrix (DCM) and called rotation matrices are used, each of which has a dimension of 3x3. An example, written in matrix form, could be the following, where a coordinate transformation is performed from Perifocal RF to EME2000 RF:

$$\left\{ \begin{array}{c} r_I \\ r_J \\ r_K \end{array} \right\}_{ijk} = \left[\begin{array}{ccc} \hat{I}\cdot\hat{p} & \hat{I}\cdot\hat{q} & \hat{I}\cdot\hat{w} \\ \hat{J}\cdot\hat{p} & \hat{J}\cdot\hat{q} & \hat{J}\cdot\hat{w} \\ \hat{K}\cdot\hat{p} & \hat{K}\cdot\hat{q} & \hat{K}\cdot\hat{w} \end{array} \right] \left\{ \begin{array}{c} r_p \\ r_q \\ r_w \end{array} \right\}_{pqw} \tag{2.6}$$

which in compact form is written as $\bar{r}_{ijk} = L\bar{r}_{pqw}$. Since the reference systems are then orthogonal, the rotation matrix L is orthogonal and its inverse is equal to its transpose $L^{-1} = L^T$. Consequently, the dual transformation $\bar{r}_{pqw} = L^T\bar{r}_{ijk}$ applies.

---

[4] The VNC RF is a coordinate system commonly used in orbital dynamics to describe the motion of a satellite around a central body and to analyze the forces and velocity variations along the orbit. The $\hat{V}$-axis is aligned with the direction of the instantaneous velocity of the orbiting object and is tangential to the trajectory; the $\hat{N}$-axis is perpendicular to the orbital plane and points in the direction of the angular momentum $\vec{h}$ of the orbit (defined with the right-hand rule); the $\hat{C}$-axis is perpendicular to $\hat{V}$ and $\hat{N}$ and is contained in the orbital plane and points outwards from the orbit.

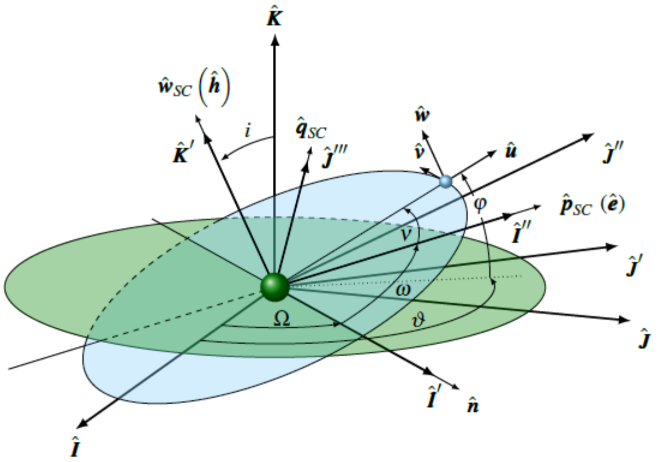

Figure 2.3: Transformation steps from the EME2000 RF $\left\{\hat{I}, \hat{J}, \hat{K}\right\}$ to the Perifocal RF $\{\hat{p}_{SC}, \hat{q}_{SC}, \hat{w}_{SC}\}$.

The scalar products constituting the matrix L are specified in more detail below: first of all, the required transformation is carried out by means of the succession of three elementary rotations called *Euler rotations* or also referred to as 3-1-3 rotations (this is why these angles are also called *Euler angles*).

Analysing them in detail:

1. Rotation of Ω around $\hat{K}$: rotating $\hat{I}$ and $\hat{J}$ by an angle equal to RAAN brings them onto the $\hat{n}$ and $\hat{m}$ transition versors.

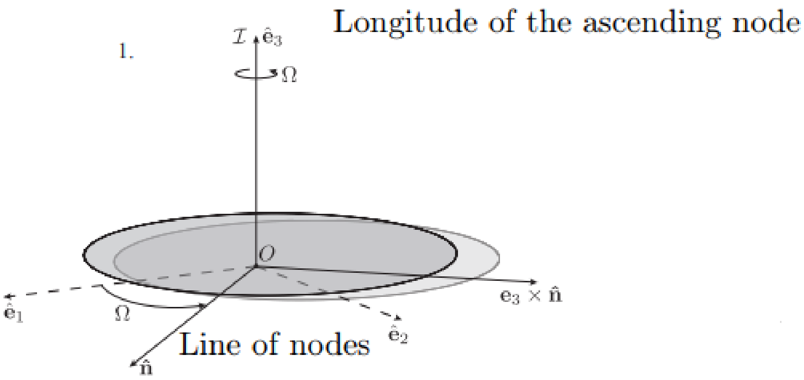

Figure 2.4: First Euler rotation.

In doing so, one has a rotation matrix L_1^T equal to:

$$L_1^T = \begin{bmatrix} \hat{I}\cdot\hat{n} & \hat{J}\cdot\hat{n} & 0 \\ \hat{I}\cdot\hat{m} & \hat{J}\cdot\hat{m} & 0 \\ 0 & 0 & 1 \end{bmatrix} \longrightarrow L_1^T = \begin{bmatrix} \cos\Omega & \sin\Omega & 0 \\ -\sin\Omega & \cos\Omega & 0 \\ 0 & 0 & 1 \end{bmatrix} \tag{2.7}$$

So with the first rotation one has $\bar{r}_{nmk} = L_1^T \bar{r}_{ijk}$.

2. Rotation of i around $\hat{n}$: according to the study of the classical orbital parameters that will be seen later, performing such a rotation means tilting the versor $\hat{K}$ by an angle i bringing it to $\hat{w}$.

   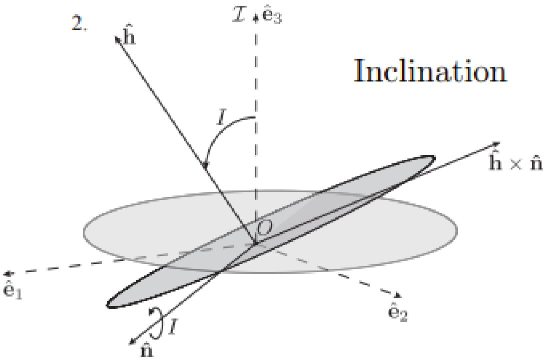

   Figure 2.5: Second Euler rotation.

   The associated rotation matrix L_2^T to go from $\widehat{nmk}$ to $\widehat{niw}$ will be:

   $$L_2^T = \begin{bmatrix} 1 & 0 & 0 \\ 0 & \hat{m}\cdot\hat{i} & \hat{K}\cdot\hat{i} \\ 0 & \hat{m}\cdot\hat{w} & \hat{K}\cdot\hat{w} \end{bmatrix} \longrightarrow L_2^T = \begin{bmatrix} 1 & 0 & 0 \\ 0 & \cos i & \sin i \\ 0 & -\sin i & \cos i \end{bmatrix} \tag{2.8}$$

   And so $\bar{r}_{niw} = L_2^T \bar{r}_{nmk}$.

3. Rotation of ω around $\hat{w}$: with this last rotation one operates on the line of nodes $\hat{n}$ by rotating it by an angle equal to the argument of the periastrum w to identify the verse $\hat{p}$ (pointing to the periastrum), while the verse i will identify $\hat{q}$.

   The last rotation matrix L_3^T allowing the transition from $\widehat{niw}$ to $p\hat{q}w$ will have as its directing cosines:

   $$L_3^T = \begin{bmatrix} \hat{p}\cdot\hat{n} & \hat{p}\cdot\hat{i} & 0 \\ \hat{p}\cdot\hat{n} & \hat{q}\cdot\hat{i} & 0 \\ 0 & 0 & 1 \end{bmatrix} \longrightarrow L_3^T = \begin{bmatrix} \cos\omega & \sin\omega & 0 \\ -\sin\omega & \cos\omega & 0 \\ 0 & 0 & 1 \end{bmatrix} \tag{2.9}$$

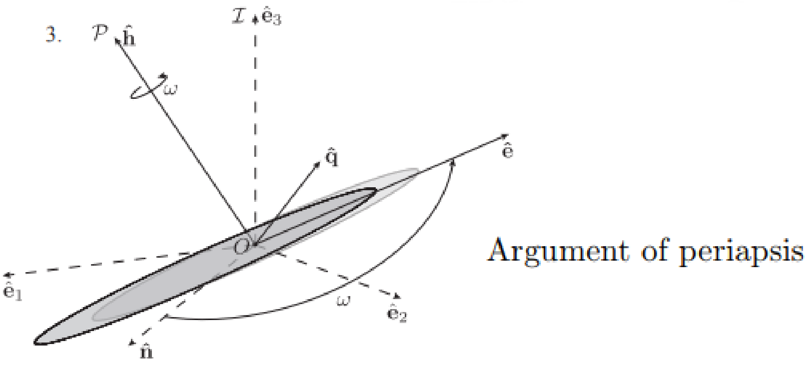

Figure 2.6: Third Euler rotation.

And this consequently results in $\bar{r}_{pqw} = L_3^T \bar{r}_{niw}$.

Thus, at the end of it all, one obtains the complete rotation matrix L^T, which allows the transfer of coordinates from the perifocal reference system to the geocentric-equatorial reference system EME2000 via the *Euler rotations* described:

$$\bar{r}_{pqw} = L_3^T L_2^T L_1^T \bar{r}_{ijk} \longrightarrow \bar{r}_{pqw} = L^T \bar{r}_{ijk} \tag{2.10}$$

with $L_3^T L_2^T L_1^T = L^T$. The inverse rotations can be easily determined through the transpose of L^T being, as mentioned before, an orthogonal matrix.

In essence, with the procedures described, it is possible to move from defining the state of the system as classical Keplerian parameters to a system of Cartesian co-ordinates. In fact, having assigned the orbital parameters $\{a, e, i, \Omega, \omega, \nu\}$ and determined the semilatus rectum $p = a(1 - e^2)$ and the equation of the conic (2.5), one first derives the components of the vector radius $\bar{r}$ and velocity $\bar{v}$ in the perifocal RF according to the expressions in (2.3a) and (2.3b). Having done this, the three elementary rotations seen above are applied to these vectors, knowing the values of Ω, ω and i, which allow the state to be derived in terms of positional coordinates and velocity in the EME2000 reference system.

2.2 2-body problem

The 2BP two-body problem constitutes a sub-case of the N-body problem (when $N = 2$) and represents one of the fundamental foundations of orbital mechanics. It describes with a very good approximation the motion of two mutually attracting objects according to Newton's law of universal gravitation. In particular, this problem makes it possible to analyse the orbits of satellites around planets, as well as planetary motions around the Sun. The solution to the problem is obtained by reducing the system to a reduced mass and considering the centre of mass as an inertial system, thus allowing equations for elliptical, parabolic and hyperbolic orbits to be derived. This section provides a detailed description of the problem, its solutions and applications in astrodynamics, as well as presenting a closed-form analytical solution.

The spaceflight case under discussion here sees a relatively small body of mass m (the spacecraft) under the influence of a very massive body M or primary (the Earth), with $M >> m$, and subject only to the mutual force of gravitational attraction. The presence of any other celestial body outside the primary and secondary is neglected (the presence of a third body is therefore neglected). As a simplifying assumption, one considers the two bodies under analysis as point-like, homogeneous and constant masses.

To derive the equations describing the problem, one considers an inertial reference system X, Y and Z.

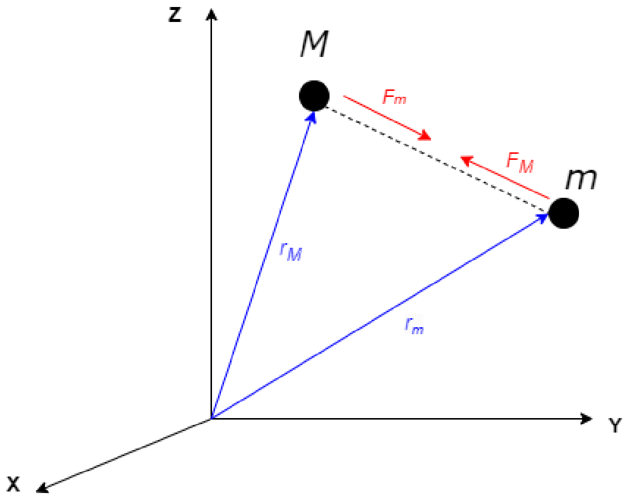

Figure 2.7: System for defining 2BP.

Earth M and spacecraft m are shown, whose respective position vectors from the origin of the system are denoted $\vec{r}_M$ and $\vec{r}_m$. From Newton's second law, the gravitational forces between the two are equal and opposite, and directed along their conjunction:

$$m\ddot{\vec{r}}_m = -G\frac{mM}{r^2}\frac{\vec{r}}{r} \tag{2.11a}$$

$$M\ddot{\vec{r}}_M = +G\frac{mM}{r^2}\frac{\vec{r}}{r} \tag{2.11b}$$

with G the universal constant of attraction. Since one is interested in studying the motion of body m with respect to body M, one defines the relative distance between the two by subtracting (2.11b) from (2.11a), obtaining:

$$\ddot{\vec{r}} = \ddot{\vec{r}}_m - \ddot{\vec{r}}_M = -G\frac{m+M}{r^2}\frac{\vec{r}}{r} \tag{2.12}$$

According to the above, $m << M$, so it can be neglected by assuming m to be approximately null and one has:

$$\ddot{\vec{r}} + \frac{GM}{r^2}\frac{\vec{r}}{r} = 0 \tag{2.13}$$

The GM parameter, by definition, is the gravitational parameter of the Earth (in general of the primary body):

$$GM = \mu_{\oplus} \tag{2.14}$$

with $\mu_{\oplus} = 398600\ km^3/s^2$.

Substituting in the (2.13) one obtains:

$$\ddot{\vec{r}} + \frac{\mu_{\oplus}}{r^2}\frac{\vec{r}}{r} = 0 \tag{2.15}$$

which represents the equation of motion of the secondary body m with respect to the main body M in 2BP. This is a second-order vector differential equation written with respect to the inertial reference system which, when integrated, allows the position (and therefore the trajectory) of body m with respect to M to be determined.

It can be shown that the solution of (2.15) shows the existence of two prime integrals, called *constants of motion*, which remain unchanged along the orbit:

- Total specific energy

  $$\mathcal{E} = \frac{v^2}{2} - \frac{\mu_{\oplus}}{r} = \text{cost} = -\frac{\mu_{\oplus}}{2a} \tag{2.16}$$

  The expression states that in a gravitational field the sum of kinetic energy and potential energy, both referring to the unit mass of the spacecraft, is constant (as one increases, the other decreases, and vice versa). In fact, the relationship just written translates into decreases in velocity moving away from the body and increases in velocity approaching it. It is assumed that gravitational potential energy, defined minus a constant, is zero when the distance from the primary body tends to infinity: in this condition, thus, the integration constant is zero.

The value of $\mathcal{E}$ determines the nature of the orbit under analysis: for closed orbits $\mathcal{E} < 0$, while for open orbits there is $\mathcal{E} = 0$ for parabolic orbits and $\mathcal{E} > 0$ for hyperbolic orbits.

- Momentum angular momentum By vector multiplying (2.15) with the vector $\vec{r}$, one can write:

  $$\vec{r} \times \ddot{\vec{r}} + \vec{r} \times \frac{\mu_\oplus}{r^3}\vec{r} = 0, \tag{2.17}$$

  which can be reformulated as

  $$\frac{d}{dt}\left(\vec{r} \times \dot{\vec{r}}\right) = 0. \tag{2.18}$$

  Consequently, one has that the product within the derivative is constant:

  $$\vec{h} = \vec{r} \times \vec{v} = \text{constant} \tag{2.19}$$

  Again, this is commonly expressed per unit mass. The quantity just obtained is called the *angular momentum* $\vec{h}$ and is a constant vector in modulus, direction, and direction. This means that the trajectory of the body m is contained in the plane (it is called a *plane motion*): being a central force, gravity does not vary the angular momentum of the orbiting body.

At this point, integrating the equation of motion (2.15) yields the body's trajectory $\vec{r}$. Leaving aside the various mathematical steps, not given here for the sake of clarity, it can be shown that the result following integration is:

$$\vec{r} = \frac{\frac{\vec{h}^2}{\mu_\oplus}}{1 + \frac{B}{\mu_\oplus}\cos\nu} \tag{2.20}$$

where B is a vector constant of integration. The expression obtained represents the trajectory that the secondary body m follows with respect to the main body M in a 2BP.

Analysing carefully what has been obtained, it is immediate to observe a similarity between (2.20) and the equation of the conic in polar coordinates (2.5). This essentially confirms Kepler's first law, i.e. the body moves through space tracing a trajectory that is nothing more than an ellipse.

In conclusion, the 2BP model just described is used in this thesis to determine the optimal trajectory to reach the selected debris. It is specified, however, how in the second part the model was made more faithful by the addition of perturbations, which will be discussed later.

2.2.1 Equation of motion

Having introduced the dynamic model that will be used to describe the motion of the bodies involved in the study, it is obviously necessary to present the equations of motion that illustrate their evolution in terms of velocity and position throughout the mission. The state of the spacecraft is described by the following set of ODEs, written in an inertialRF centered on the Earth:

$$\frac{d\vec{r}}{dt} = \vec{v} \tag{2.21a}$$

$$\frac{d\vec{v}}{dt} = \vec{g} + \frac{\vec{T}}{m} + \vec{a}_p \tag{2.21b}$$

$$\frac{dm}{dt} = -\frac{\vec{T}}{c} \tag{2.21c}$$

Where (2.21a) and (2.21b) represent how the spacecraft's position and velocity vary, respectively. It can be seen that the derivative of the velocity vector is generally given by the sum of the gravitational acceleration $\vec{g}$ and thrust $\vec{T}$ vectors, to which the perturbative contribution $\vec{a}_p$ is added. Alongside these, one also appends the (2.21c), which expresses the spacecraft's mass variation and, thus, allows a trace of the propellant consumption over time.

In general, other forces could be present, such as gravitational effects due to the presence of additional bodies, but these are neglected in 2BP. The same equations, but expressed in Cartesian coordinates used for the optimization, are given in section (3.5).

2.2.2 Classical orbital parameters

The shape and orientation of the orbit are completely contained in the position and velocity vectors of the body at an instant in time. However, using these vectors is extremely impractical for identifying an orbit. Therefore, given an initial instant, a Keplerian trajectory traced by the motion of a secondary body around a primary body is univocally described by 6 parameters, which are called *classical orbital parameters* and are listed in the table (2.1). These parameters are obviously dependent on the position and velocity vectors and are directly calculable from them.

Of the 6 parameters in the table (2.1), 4 of them are necessary for the 2-dimensional problem: in particular, 3 parameters are required to describe the shape and size of the orbit and the direction of the apsidal line (i.e., the position of the periastrum); a fourth is required to locate the position of the secondary body

Table 2.1: Classical orbital parameters.

a	Semi-major axis
e	Eccentricity
i	Inclination
Ω	RAAN
ω	Argument of Periastrum
ν	True Anomaly

along the orbit with respect to the periastrum at a given instant. Then, 2 more parameters are essential in three-dimensional space to describe the orientation of the orbit plane with respect to the chosen reference system.

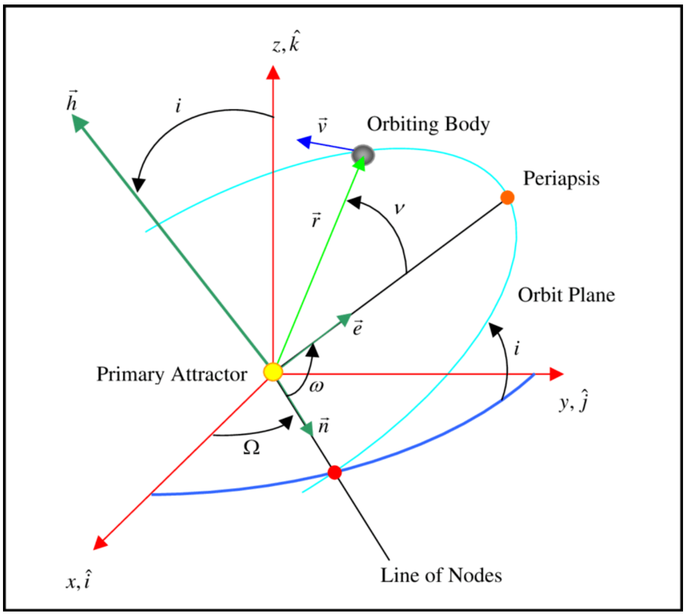

Figure 2.8: Keplerian orbital elements.

With reference to the figure (2.8), the classical orbital parameter set is defined as follows:

- Semi-major axis a
  Defines the size of the orbit. For the ellipse, it is easy to identify, while for the parabola it tends to infinity and for the hyperbola it takes on a negative value and represents half the distance between the two periaxes of the mathematically admissible orbits. The geometric significance for the hyperbola is unimportant, as one of the two branches is not physically traversed. The semi-major axis can be related, as seen in (2.16), to the energy content of the orbit:

$$a = -\frac{\mu_\oplus}{2\mathcal{E}} \tag{2.22}$$

Having then $\mathcal{E}$ expression (2.16), if the energy is positive, in the case of the hyperbola, when r goes to infinity the spacecraft has a certain velocity called hyperbolic excess velocity:

$$v_\infty = \sqrt{2\mathcal{E}} \tag{2.23}$$

If the energy is zero, in the case of the parabola, the hyperbolic excess velocity is zero, i.e, one reaches infinity with zero velocity. If energy is negative, in the case of the ellipse, the hyperbolic excess velocity is an imaginary number, so infinity cannot be reached. As an alternative to the semi-major axis, when for example it is infinite and undefined, the semilatus rectum p can be used:

$$p = \frac{\vec{h}^2}{\mu_\oplus} \tag{2.24}$$

This is related to the angular momentum of the orbit and geometrically represents the distance between the primary body and the point on the orbit where the true anomaly is 90° or 270°.

- Eccentricity e
  Defines the shape of the orbit. It can be expressed as:

  $$e = \sqrt{1 + 2\mathcal{E}\left(\frac{\vec{h}}{\mu_\oplus}\right)^2} \tag{2.25}$$

  and its direction points towards the periastrum.

- Inclination i
  Defined by the angle between the plane of the orbit and the normal to the reference plane, in this case the equatorial plane. It is calculated as:

  $$i = \cos^{-1}\left(\frac{h_K}{h}\right) \tag{2.26}$$

  with h_K being the component of $\vec{h}$ along the verse $\hat{K}$.

- Right Ascension of the Ascending Node (RAAN) Ω
  Defined by the angle between the node line and the $\hat{I}$-axis in the fundamental plane. The mathematical definition is:

$$\Omega = \cos^{-1}\left(\frac{n_I}{n}\right) \tag{2.27}$$

  with $\hat{n} = \hat{K} \times \hat{h}$ vector of the node line, pointing towards the ascending node. It represents the point at which the satellite crosses the fundamental plane from below to above.

- Argument of periastrum ω Defined by the angle between the node line and the eccentricity vector (pointing towards the periastrum) measured in the direction of the satellite's motion. It is defined as:

$$\omega = \cos^{-1}\left(\frac{n \cdot e}{en}\right) \tag{2.28}$$

- True Anomaly ν
  Defines where the spacecraft is located along the orbit and is given by the angle between the eccentricity vector and the position vector. It is defined with a time reference t_0 called the epoch (sometimes replaced by the time of transition to periastrum T). The mathematical definition is:

$$\nu = \cos^{-1}\left(\frac{e \cdot r}{er}\right) \tag{2.29}$$

The orbital parameters a and e define the geometry of the orbit (shape and size). The parameters i, Ω and ω define how it is oriented in space. Finally, the parameters seen are not the only way to characterise an orbit, as there may be conditions in which some of these elements are indeterminate: in this case, for example, other sets of parameters, such as *equinoctial parameters*, can be used.

2.3 Sun-Synchronous Orbit

As discussed in Chapter 1, SSO orbits form the heart of this work, given the importance of these orbits due to their particular characteristics as seen. Such orbits, in fact, exploit in some way the precession of the line of nodes in a retrograde manner (i.e., in the opposite direction of the Earth's rotation) for purposes of Earth surveillance, which must be done in a systematic manner. In detail, it is relevant that the area in question is constantly and continuously monitored so that from a possible comparison of the images obtained, a user is able to tell whether or not something has happened in the time between two observations (image processing algorithms are used).

Since it is crucial to monitor the area concerned under the same lighting conditions, SSO orbits prove purposeful for this task, presenting an inclination of 95-100 degrees on the equatorial plane and a variant altitude between 600-800 km (being a particular LEO), with an orbital period of around 90-100 minutes.

For this to be feasible, the plane of the orbit is rotated by exploiting the phenomenon of the precession of the line of nodes, which must rotate a certain number of degrees per day for the orbital plane to have the exact incidence with respect to the Earth-Sun conjunction. In essence, the precession velocity due to the $J2$ perturbation will have to be:

$$\dot{\Omega} = -\frac{3}{2} J_2 \left(\frac{R_\oplus^2}{a^2} \right) \frac{\cos i}{(1-e^2)^2} \sqrt{\frac{\mu_\oplus}{a^3}} \tag{2.30}$$

This $\dot{\Omega}$ will be an input to the problem: the selection of orbital parameters defining an SSO, in fact, is closely linked to mission objectives, which determine the design requirements and constraints. If one wants to understand what the heats of a and i of the satellite's orbit on the SSO must be, one must impose $\dot{\Omega}$, which will be given by the design requirement to meet the condition discussed earlier. Specifically, the line of nodes will have to rotate 360° in a year, which means it must make a daily variation of 0.9856 °/day, which corresponds to $1.991 \cdot 10^{-7}$ rad/sec: this will be the mission target. By imposing this value in the (2.30), the values of a and i of the SSO orbit in question are determined, knowing the values of $\mu_\oplus$, $R_\oplus$, and $J2$.

2.4 Perturbing accelerations

So far, when discussing celestial mechanics and orbits, one has considered ideal Keplerian orbits, which are obtained through fairly simplifying assumptions, but which are not possible. By conducting a more realistic treatment now, these assumptions of the 2BP fall away, leading to actual orbits in which the results obtained can still be maintained, but it must be admitted that there will certainly be perturbative actions: one will in fact speak of perturbed Keplerian orbits.

The dynamic model used in the propagator for the deorbiting phase implements two of the main perturbations affecting the motion of a satellite orbiting in the LEO region: the Earth's non-sphericity $J2$ and atmospheric drag D. Therefore, the vectorial form of the cumulative combined perturbing acceleration from the system in equation (2.21b) is:

$$\vec{a}_p = \vec{a}_{j2} + \vec{a}_D \tag{2.31}$$

These perturbations have been identified as the most significant ones in the LEO environment. Obviously, for a more refined model and even more faithful results, additional perturbative effects, such as lunar-solar attraction or solar radiation pressure, could be implemented.

The perturbations that make up the vector (2.31) are discussed below.

2.4.1 Earth asphericity J2

The gravitational perturbation associated with the $J2$ coefficient is one of the most relevant corrections in the study of orbits around the Earth and geodesy, necessary to take into account its actual shape, which deviates from a perfect sphere. Indeed, the Earth is an oblate ellipsoid, with a bulge at the equator due to its rotation. This flattening at the poles, quantified by the parameter $J2$, introduces variations in the gravitational field compared to that of a uniform sphere. Although potential energy has previously been defined as:

$$\mathcal{U} = -\frac{\mu_{\oplus}}{r} \tag{2.32}$$

the fact that the Earth has a non-homogeneous mass distribution causes gravitational anomalies to arise on its surface that will greatly influence the orbital motion of the satellite. For this reason, the expression just written does not correctly model the Earth's potential: to this main contribution, it will be necessary to add a series of terms that take into account various factors (e.g. flattening at the poles, bulging at the equator, etc...). Therefore, the potential expression is broken down into several terms, the quantitative value of which is the subject of geodesy studies. The expression will be:

$$\begin{aligned} U = \frac{\mu}{r}\{1 - \sum_{l=2}^{\infty} J_l \left(\frac{R_{\oplus}}{r}\right)^l P_l(\sin\phi) + \\ + \sum_{l=2}^{\infty}\sum_{m=1}^{l} \left(\frac{R_{\oplus}}{r}\right)^l P_{l,m}(\sin\phi)\left[C_{l,m}\cos(m\theta_{LO}) + S_{l,m}\sin(m\theta_{LO})\right]\} \end{aligned} \tag{2.33}$$

Where $P_{l,m}$ are the associated Legendre polynomials of degree n and order m, while $C_{l,m}$ and $S_{l,m}$ are the coefficients of the spherical harmonics. The Earth's rotation speed is then assumed to be constant, neglecting nutation and precession. The (2.33) shows the various contributions made to the Earth's potential:

- Zonal harmonics, defined by polynomials of order zero ($m = 0$). The harmonics of degree n even somehow represent the Earth's symmetry with respect to the equatorial plane, while those of degree n odd are indices of asymmetries. Of all these, the most significant contribution that will be considered in the study is the $J2$ term ($n = 2$, $m = 0$) that indicates the Earth's flattening at the poles and, therefore, its non-sphericity;

- The tesseral harmonics, when $n \neq m$ and the sectoral harmonics, when $n = m$, with n and m different from zero. All these harmonics are indices of the variety of the Earth's gravitational field. As order and degree increase, their contributions become smaller and smaller and negligible.

The Earth's longitude in the (2.33), then, is obtained as:

$$\theta_{LO}(t) = \theta - \theta_G(t) = \theta - [\theta_{Gref} + \omega_E \, (t - t_{ref})] \tag{2.34}$$

The reference time t_{ref} is the J2000 epoch, January 1, 2000 at 12:00:00 UTC (51544.5 MJD), and $\theta_{G0} = 280.46061837504$ deg; ω_E is evaluated assuming the sidereal day equal to 86164.098903690351 s (no precession is considered).

Accelerations caused by Earth's irregular gravitational field are obtained by calculating the gradient of the potential function. In order to compute the perturbations that deviate Earth's potential function from that of a sphere ($\mu_\oplus/r$), the function that is partially derived is $\Phi = \mathcal{U} + \mu_\oplus/r$; in the ZEN RF:

$$(a_j)_u = \frac{\partial \Phi}{\partial r} \tag{2.35a}$$

$$(a_j)_v = \frac{\partial \Phi}{\partial \theta} \frac{1}{r \cos \varphi} \tag{2.35b}$$

$$(a_j)_w = \frac{\partial \Phi}{\partial \varphi} \frac{1}{r} \tag{2.35c}$$

The calculation of the first two derivatives with respect to r and θ is fairly straightforward. The third derivative with respect to φ, on the other hand, requires the derivation of the associated Legendre polynomials, which are obtained recursively, exploiting the properties of Legendre polynomials.

The complexity of working with this derivative and the difficulty of implementing it in the propagator are some of the reasons for choosing to work in Cartesian coordinates in order to calculate the perturbative accelerations related to the $J2$ contribution, and reported in section (5.2). The main effects related to this perturbation that affect the orbital mechanics are:

- *Regression of the satellite orbit node line*: this is manifested through a variation in time of the RAAN Ω, which will be negative in the case of direct orbits and positive in the case of retrograde orbits. This means that, given the line of nodes, if the satellite in its orbit is directed towards the east, the line of nodes will move in the opposite direction towards the west.

  The effect can be quantified by evaluating the rate of change of Ω:

$$\dot{\Omega} = -3\pi J_2 \left(\frac{R_\oplus}{p}\right)^2 n_0 \cos i \quad \text{[rad/day]} \tag{2.36}$$

with n_0 a parameter indicating how many revolutions there are in a day. It can be seen from the relationship that the perturbative effect is greatest, in absolute value, at low altitudes and inclinations. However, it is widely used in mission analysis to save propellant: the different regression rate of two planes at different altitudes and/or inclinations causes them to align after a certain time interval.

- *Precession of the apsides line*: this phenomenon implies that if, for example, the satellite is rotating eastwards, this line will also rotate in the same direction, causing a change in the argument of the periastrum ω. It is therefore quantified as:

$$\dot{\omega} = \frac{3}{4}\left(\frac{R_\oplus}{p}\right)^2 \sqrt{\frac{\mu_\oplus}{a^3}}(5\cos i^2 - 1) \tag{2.37}$$

and the perturbation cancels out for two specific inclinations, $i = 63.4°$ and $i = 106.6°$, with the former exploited by the Molniya orbits[5].

2.4.2 Atmospheric Drag

Atmospheric drag D represents one of the main perturbations affecting the motion of satellites in LEO and, at this point, on the satellite investigated in this thesis. This phenomenon is due to the presence of the outermost layers of the Earth's atmosphere, which, although extremely rarefied at those altitudes, exert a resistance force on the moving satellite (it vanishes completely around 100 km altitude). This atmospheric resistance acts in the opposite direction to the satellite's motion, causing a gradual dissipation of orbital energy by changing its momentum.

$$\vec{a}_D = -\frac{1}{2} c_D \rho \frac{S}{m} |\vec{v}_{rel}| \vec{v}_{rel} \tag{2.38}$$

where velocity is evaluated in relation to the Earth's rotational velocity as:

$$\vec{v}_{rel}(t) = \vec{v}(t) - \vec{\omega}_E \times \vec{r}(t) \tag{2.39}$$

---

[5] These are highly elliptical orbits with an orbital period of half a sidereal day, allowing them to cover the northern hemisphere for a long time.

This force is resistive, which explains the presence of the sign ‘-’, as it decreases the velocity; S represents the spacecraft’s exposed cross sectional area (which depends on the attitude of the satellite); c_D is the drag coefficient, and is typically about 2 (so high because it is related to different mechanisms than those occurring on Earth at sea level); ρ is the density of the atmosphere, which can vary depending on solar activity.

The main effect of atmospheric drag is a decrease in orbital altitude over time, resulting in a reduction in the semi-major axis of the orbit and hence the orbital period. This leads to a progressive spiral towards Earth, which can culminate in the atmospheric re-entry of the satellite if corrective manoeuvres are not applied.

Therefore, this perturbation represents a critical aspect for the design and maintenance of satellite orbits, requiring the use of accurate atmospheric models to predict orbital evolution. Within the developed propagator, the atmospheric model implemented for the density is that of the exponential trend:

$$\rho(h) = \rho_{sl} e^{-\frac{h}{H}} \tag{2.40}$$

with H density factor of scale, representing the height at which the atmospheric density decreases by a factor e (approximately 2.718), and depends on the composition and temperature of the atmosphere at those altitudes. The use of this model makes it possible to simplify the calculation of perturbations due to atmospheric drag for satellites in low orbits, giving a useful approximation for predicting orbital decay, which is what we actually want to study by implementing this perturbation.

Chapter 3

Optimal Control Theory

This chapter aims to illustrate the mathematical concepts that form the foundation of the optimization problem related to space trajectories in the broadest sense, briefly investigating the most common numerical methods used to solve it.

Firstly, it is interesting to understand why this discipline is now essential in the feasibility study of a mission and is a cornerstone in the astrodynamics research field. Since the dawn of space conquest, the various efforts to reach beyond the Earth's atmosphere have had as a common goal to carry a specific payload (manned or unmanned) into orbit, necessary to accomplish a generic mission.

This purpose entails a cost from the point of view of the propellant that the spacecraft will have to board: in fact, the propulsive effort m_p to be carried out will strictly depend on the specific mission to be achieved through the total I_t impulse. A scenario may also arise in which, as analyzed in Section 1.2, in the field of electric propulsion, to increase the specific impulse I_{sp}, one goes to decrease the thrust T: the same desired ΔV, therefore, will require longer times, and this may conflict, for example, with time constraints imposed by the mission. In this context, reducing the cost and time to access and use space without compromising quality and safety becomes a key objective.

Thus, this is how trajectory optimization meets such needs. The subject can be stated as the determination of a trajectory for a spacecraft that satisfies specific initial and terminal conditions, i.e., that leads to the realization of the required mission, while extremes a quantity of interest (maximizing or minimizing it).

The most common goal is the minimization of the demanded propellant or, equivalently, the maximization of the payload fraction: doing so will accomplish the same maneuver while spending less propellant mass, with an undoubted benefit on the overall mission mass budget.

There are also spacecraft trajectory problems, as mentioned, where it is relevant to minimize flight time, which is helpful for human missions.

In both cases, the Optimal Control Problem (OCP) aims to find a control law that extremes a specific index of merit by determining the inputs to the dynamical system under analysis that will allow it, while satisfying any constraints imposed on the system's motion. In this thesis, maximizing the final mass of the spacecraft was prioritized.

3.1 Compendium of Numerical Methods for OCPs

Numerical methods for solving optimal control problems date back as far as the 1950s, and from then until now, their complexity has undoubtedly increased, as has the variety of applications in which they are used (this is also due to the development of digital computers). Historically, low-thrust trajectory optimization problems have been formulated as Continous Optimal Control Problems (COCPs).

This section will review the most common methods for solving them, highlighting their differences and the reasons behind choosing one approach over another. For the sake of brevity, a quick overview of them will be given here. In the reference [**9**], Betts has published a detailed discussion of the various techniques available, where the author analyzes OCP numerical techniques with boundary and path constraints, giving an example of the general space applications.

All methods, however, aim to convert the low-thrust trajectory COCPs, which are very complex and governed by a set of Ordinary Differential Equation (ODE)s into a problem with a finite number of variables, by an operation called *transcription*. As a rule, there are two different approaches: analytic and numerical. Although the former provide closed-form resolution for the optimal trajectory, the possibility of obtaining it is reduced to particular cases only and are rarely feasible for most spacecraft trajectory optimization problems.

For these reasons, OCPs are mainly solved through numerical approaches, which can be categorized into two main types:

- Direct Methods, based on Karush-Kuhn-Tucker (KKT) optimality conditions. More informations can be found in [**10**];
- Indirect Methods, based on Pontryagin's Maximum Principle (PMP) (for a maximization problem, otherwise it is known as Pontryagin's minimum Principle, PmP) [**11**].

Interesting details on how such methods operate are described in references [**12**] and [**13**]. Below, the paragraph briefly highlights the salient points of the two approaches listed before.

On the one hand, in a direct method, the optimal solution is sought by transforming the infinite size optimization problem into a large size finite dimension problem. In detail, the state and/or control of the COCP is discretized in some way and the problem is transcribed into a Non Linear Programming (NLP) problem or *Non Linear Optimization Problem*, solved by appropriate optimization techniques in which the objective function is *directly* optimized. Such a transcription process requires the discretization of the control variables in a time-grid. The goal of the NLP will next be to determine a vector of unknown variables that satisfy a set of nonlinear constraints, including the equality and inequality conditions. The optimal solution of the NLP must satisfy first-order necessary optimality conditions, known as KKT conditions.

On the other hand, indirect methods solve the problem *indirectly* (hence the name) by converting the OCP into a Multi Point Boundary Values Problem (MPBVP): as a consequence of this, the solution of the optimality problem will be determined by solving a system of differential equations satisfying endpoint and/or interior point conditions. This approach, in essence, relies on the principle of Calculus of Variations (CoV) to find the first-order optimality conditions of the original OCP to be satisfied. Unlike the previous one, in the indirect method, a vector of co-states of the same size as the vector of states (to which these added variables are associated) is introduced, which respects the Euler-Lagrange equations. The problem, then, reduces to finding the initial values of the co-state vector to match the optimality necessary conditions, respecting the algebraic constraints by introducing Lagrange multipliers into the index of merit.

Anticipating already what will be covered in this chapter, the necessary conditions for optimality are obtained by setting the first derivative of the merit index to zero. The results come through the imposition of three systems:

1. Euler-Lagrange equations, which define the evolution of the co-states, i.e., the added variables;
2. Transversality conditions, translatable as algebraic conditions that define, explicitly or implicitly, the value that states and co-states take on the boundaries of the trajectory;
3. Optimality conditions for controls, namely, algebraic equations linking control variables with states and co-states at each time.

3.1.1 Comparison: Direct versus Indirect Methods

The references [**14-15**], recommended for a more comprehensive point of view, provide an exhaustive comparison of the two methods. The main difference between the two methods, as seen, is the introduction of the added variables associated with the states. In a very general line, one could say that in a direct approach, the OCP is first discretized and then optimized; conversely, indirect techniques involve first the derivation of the optimal condition and only then the discretization of the problem.

Direct methods are straightforward to code because there is no need to know Optimal Control Theory (OCT). In fact, the user has the advantage of not needing to derive the necessary first-order conditions. As a result, they are easy to initialize because of the large convergence domain and the fairly immediate physical meaning that the optimization variables take on.

However, to obtain an accurate solution, the mesh defining the discretized domain must be sufficiently dense, and this implies a conspicuous number of discrete nodes/points that greatly aggravate the computational cost. Therefore, related to this problem, and as a result of the large number of variables involved, is the slowness of solving the problem, and in addition, the results only approximate the solution (often referred to as suboptimal solution). Nevertheless, direct methods have been widely used in recent years because of their robustness/tolerance to a poor initial guess and the ability to easily handle complex control or state constraints.

On the other hand, indirect methods guarantee the fulfillment of first-order optimality conditions and offer an interesting theoretical insight into the physical and mathematical characteristics of the problem. To these must be added the fundamental strength of such approaches: the high accuracy with which the solution is obtained, even at minimal computational cost and time when compared with the direct counterpart. However, they are not as flexible methods as the previous ones, since one has to derive analytically and explicitly the expressions of the necessary optimum conditions and the equations of the required controls and co-states, which can be very complicated.

A skilled and experienced user is therefore required since this operation depends on the OCP considered, but not only that. Indeed, the convergence region of the solution is narrow, which is why they are highly sensitive to the initial guess of the solution (they are not very robust), and it is often necessary to know a priori the sequence of constrained and unconstrained arcs. All these details make indirect methods unsuitable for solving highly constrained spacecraft trajectory optimization problems, nor problems where flexibility and robustness are desired. In conclusion, it is intuitive how direct methods primarily need cost and time to be applied, while indirect methods require much specificity from users. Table (3.1) briefly summarizes the characteristics of the two approaches seen.

An interesting list of the various software programs that implement one method rather than the other can be found at [**15**]. What one observes is that, since their

Table 3.1: Direct vs. Indirect methods: advantages and problems.

Method	*Robustness*	*Flexibility*	*Optimality*
Direct	🟩	🟩	🟥
Indirect	🟥	🟥	🟩

inception, the working philosophy of the two methods has led to a dichotomy in the optimal control community: researchers who focus on indirect methods are more interested in differential equation theory, while those who invest in direct methods look more to optimization techniques.

Although at first glance they seem unrelated, the two approaches have much in common. In recent years, researchers have deepened the connections between indirect and direct forms, so much so that in many recent applications it is not unusual to apply an indirect technique downstream of a direct one to solve a problem. Therefore, it is anticipated that these two methods classes will merge as time goes on.

3.2 Optimal Control Theory

The OCP may be interpreted as an extension of the NLP problem to an infinite number of variables, and thus as an extension of CoVs.

Indeed, it is well known how the CoV deals with maximizing (or minimizing) a functional, that is, a function of functions that then associates a value with a function. The most classic example of CoV is the determination of geodesics, i.e., minimum-length curves between two points. The emergence of the CoV is typically associated with Johann Bernoulli's 1696 problem of the brachistochrone curve [**16**], namely, the search for a curve that allows a particle with a certain mass to move from an initial to a final point in the shortest possible time. Since the last century, one has begun to apply such OCT principles to space trajectory OCPs with increasing attention, becoming an intensively studied topic in the literature with a long and interesting history, exhaustively reported in [**17**].

As anticipated above, the OCP is concerned with the determination of the control law, among the existing ones, that evolves the system by optimizing a specific functional: in the domain of interest of space trajectories, the problem will determine the trajectory of the spacecraft within a dynamic model that satisfies specific initial and final conditions, which is conducting a required mission, while minimizing a quantity of interest. In this work, the object to be minimized is the required propellant or, equivalently, the fraction of the spacecraft that is not devoted to propellant is maximized.

Generally, the OCP is described by a control system consisting of a set of first-order ODEs written in the form:

$$\dot{\vec{x}} = \vec{f}(\vec{x}(t), \vec{u}(t), t) \tag{3.1}$$

which describes the evolution of the state variables vector of the system $\vec{x}(t) \in \mathbb{R}^n$ between initial time t_0 and final time t_f, where $\vec{u}(t) \in \mathbb{R}^m$ is the control variables vector, containing m different control variables. Please note that the time $t \in [t_0, t_f]$ represents the independent time variable, of which both x and u are functions, with t_0 and t_f extremal Boundary Conditions (BCs) at the beginning and the end of the trajectory: defined in this way, the problem in the previous equation is a Two Point Boundary Value Problem (TPBVP). In addition to time constraints, the problem could also have some initial conditions $\vec{x}(t_0) = \vec{x}_0$ and some terminal conditions $\vec{x}(t_f) = \vec{x}_f$ specified, thus having to satisfy q-dimensional BCs specified by the constraint vector

$$\vec{\mathcal{X}}(\vec{x}_0, \vec{x}_f, t_0, t_f) = 0 \tag{3.2}$$

where $\vec{\mathcal{X}} : [\mathbb{R}^n, \mathbb{R}^n, \mathbb{R}, \mathbb{R}] \to \mathbb{R}^q$.

The vector of controls $\vec{u}$ could also be constrained: depending on the controls chosen, some of them could be bounded in a specific range or assume a minimum and maximum value. As will be seen later, it will appropriately shrink $\vec{u} \in \mathcal{U}$. To evaluate the optimality of an OCP, one then needs a cost functional, which associates a cost with each possible behavior of the dynamic system considered. For a given initial data $(t_0, \vec{x}_0)$, the behaviors are parameterized by control functions u: thus, the cost functional assigns a cost value to each admissible control. In this thesis, the terms *merit index* and *cost functional* are sometimes used interchangeably and denoted $\mathcal{J}$.

The goal of optimization is to find the optimal trajectory $\vec{x^*}(t)$ among the admissible ones, subject to the optimal controls $\vec{u^*}(t)$, that extremes the value of $\mathcal{J}$, which can be written in the Bolza form as:

$$\mathcal{J} = \varphi(\vec{x}_0, \vec{x}_f, t_0, t_f) + \int_{t_0}^{t_f} [\Phi(\vec{x}(t), \vec{u}(t), t)] dt \tag{3.3}$$

Note that the objective function is entirely determined by the input function u, for a given dynamical system and initial conditions.

The one just posed is no more than a variational calculus problem, i.e., an optimization problem in which the unknown is a function instead of simply an unknown variable. A particular input/control $\vec{u^*}(t)$ is optimal if $\mathcal{J}(\vec{u^*}) \geq \mathcal{J}(\vec{u})$, for every $\vec{u} \in \mathcal{U}$, respecting the BCs. The expression of $\mathcal{J}$ in equation (3.3) is composed by the sum of two main terms: the integral of the Lagrangian formulation, which considers the progress of the state and control throughout the interval between

t_0 and t_f, and the scalar of the Mayer formulation, which calculates the values obtained from the state at a final time t_f. One often refers to these two quantities as *running cost* and *terminal cost*, respectively, and it is always possible to switch from one formulation to the other with the help of auxiliary variables : the equation (3.3) can then be rewritten either in Lagrange's formulation with $\varphi = 0$ or in Mayer's formulation with $\Phi = 0$. The latter formulation will be used in the thesis.

From here onward, the following notation is introduced for the sake of brevity:

$$\varphi \triangleq \varphi(\vec{x}_0, \vec{x}_f, t_0, t_f), \tag{3.4}$$

$$\mathcal{X} \triangleq \vec{\mathcal{X}}(\vec{x}_0, \vec{x}_f, t_0, t_f). \tag{3.5}$$

Next, manipulation of the equation (3.3) is carried out, which will allow the optimality problem to be posed in a different but mathematically equivalent way, so that the indirect methods principles can be applied.

Considering a simple problem with a single phase, the optimality conditions are found with the use of the Lagrande multipliers $\vec{\mu}$ by imposing an augmented performance index $\mathcal{J}^*$, which includes a measure of how much constraints and state quantities are respected. In addition to these Lagrange multipliers $\vec{\mu}$ associated with the BCs, $\vec{\lambda}(t)$ multipliers, referred to as *adjoint* or *costate variables* and associated with the state variables $\vec{x}(t)$, also appear in the formulation. Due to the above, it is obvious that $\vec{\lambda} \in \mathbb{R}^n$ and $\vec{\mu} \in \mathbb{R}^m$.

With such formulation, the augmented performance index $\mathcal{J}^*$ can be written as:

$$\mathcal{J}^* = \varphi + \vec{\mu}^T \vec{\mathcal{X}} + \int_{t_0}^{t_f} \Big[\Phi + \vec{\lambda}^T (\vec{f} - \dot{\vec{x}}) \Big] dt \tag{3.6}$$

Intuitively, from the (3.6) it follows that when BCs (3.2) and differential equation (3.1) are satisfied, then $\vec{\mathcal{X}} = 0$ and $\vec{f} = \dot{\vec{x}}$ (the solution is feasible): consequently $\mathcal{J} = \mathcal{J}^*$ for any choice of λ and μ.

Manipulating the (3.6) by integrating by parts[1], it is possible to eliminate the derivative of states $\dot{\vec{x}}$ and obtain a simpler expression:

---

[1] The integration by parts formula states:

$$\int_a^b f(x) g'(x) dx = \big[f(b) g(b) \big] - \big[f(a) g(a) \big] - \int_a^b f'(x) g(x) dx$$

$$\begin{aligned}\int_{t_0}^{t_f} -\left(\vec{\lambda}^T\dot{\vec{x}}\right)dt &= -\left[\vec{\lambda}_f^T\vec{x}_f\right] - \left[-\vec{\lambda}_0^T\vec{x}_0\right] - \int_{t_0}^{t_f} -\left(\dot{\vec{\lambda}}^T\vec{x}\right)dt = \\ &= -\left[\vec{\lambda}_f^T\vec{x}_f\right] + \left[\vec{\lambda}_0^T\vec{x}_0\right] + \int_{t_0}^{t_f}\left(\dot{\vec{\lambda}}^T\vec{x}\right)dt\end{aligned} \tag{3.7}$$

Therefore, substituting in the (3.6) the (3.7) gives:

$$\mathcal{J}^* = \varphi + \vec{\mu}^T\vec{\mathcal{X}} + \left[\vec{\lambda}_0^T\vec{x}_0 - \vec{\lambda}_f^T\vec{x}_f\right] + \int_{t_0}^{t_f}\left[\Phi + \vec{\lambda}^T\vec{f} + \dot{\vec{\lambda}}^T\vec{x}\right]dt \tag{3.8}$$

Then, it is useful to group some of the terms that appear in the (3.8) to define a fundamental function that will come in handy later: the Hamiltonian $\mathcal{H}$ of the system

$$\mathcal{H} = \Phi + \vec{\lambda}^T\vec{f} \tag{3.9}$$

that depends on $\vec{x}$, $\vec{u}$, t (although not always explicitly) through $\vec{f}$ and the costates $\vec{\lambda}^T$[2].

The behavior of $\mathcal{J}^*$ can be analyzed through the first-order expansion of the functional: in particular, the necessary condition for optimality requires that the functional $\mathcal{J}^*$ be stationary and, therefore, null. The problem is thus to choose $\vec{x}_0$, t_0, the control law $\vec{u}(t)$ and t_f, when considering the end-point constraints (constraints), which cancel the variation $\delta\mathcal{J}^*$:

$$\delta\mathcal{J}^* = \left(\frac{\partial\varphi}{\partial t_0} + \vec{\mu}^T\frac{\partial\vec{\chi}}{\partial t_0} - \mathcal{H}_0\right)\delta t_0 + \tag{3.10a}$$

$$+\left(\frac{\partial\varphi}{\partial t_f} + \vec{\mu}^T\frac{\partial\vec{\chi}}{\partial t_f} + \mathcal{H}_f\right)\delta t_f + \tag{3.10b}$$

$$+\left(\frac{\partial\varphi}{\partial\vec{x}_0} + \vec{\mu}^T\frac{\partial\vec{\chi}}{\partial\vec{x}_0} + \vec{\lambda}_0^T\right)\delta\vec{x}_0 + \tag{3.10c}$$

$$+\left(\frac{\partial\varphi}{\partial\vec{x}_f} + \vec{\mu}^T\frac{\partial\vec{\chi}}{\partial\vec{x}_f} - \vec{\lambda}_f^T\right)\delta\vec{x}_f + \tag{3.10d}$$

$$+\int_{t_0}^{t_f}\left[\left(\frac{\partial\mathcal{H}}{\partial\vec{x}} + \dot{\vec{\lambda}}^T\right)\delta\vec{x} + \frac{\partial\mathcal{H}}{\partial\vec{u}}\delta\vec{u}\right]dt, \qquad j = 1, ..., n_p \tag{3.10e}$$

---

[2] Since Mayer's formulation will be used in this paper, in the written expression Φ will be null. Consequently, the Hamiltonian reduces to the product between the vector of adjoint variables and the dynamics of the system: $\mathcal{H} = \vec{\lambda}^T\vec{f}$.

with n_p number of subarcs into which the trajectory was split.

The expression (3.10) allows the optimization problem to be stated in a general way as follows: the functional $\mathcal{J}$ is maximal and has an admissible (i.e., valid) solution if an infinitesimal variation of it $\delta\mathcal{J}$ is less than or equal to zero for every admissible variation of the state variable $d\vec{x}$.

$$\delta\mathcal{J} \leq 0 \quad \forall d\vec{x} \;\longrightarrow\; \mathcal{J} = \mathcal{J}_{max}$$

In this thesis work, the boundary condition of $\delta\mathcal{J} = 0$ will be considered for the functional to be maximal, for any perturbation of the initial conditions δt_0, δt_f, $\delta\vec{x}_0$, $\delta\vec{x}_f$, $\delta\vec{x}$, and $\delta\vec{u}$ controls while respecting the constraints $\vec{\mathcal{X}} = 0$ (3.2). Cancellation of $\delta\mathcal{J}$ is ensured through appropriate choice of the adjoint variables λ and Lagrange multipliers μ. Equation (3.10), moreover, makes it possible to derive a set of conditions useful in the search for the optimum.

Since $\delta\mathcal{J}$ must be null, when the multiplicative coefficients of (3.10a) and (3.10b) are null, one derives the so-called *transversality conditions*, that is, two algebraic conditions at the initial and final times. The nulling, on the other hand, of (3.10c) and (3.10d) returns the *optimality conditions* in number equal to $2n$ (one algebraic equation per each state quantity both at initial and final bounds), which allow special conditions to be placed on the co-state λ_{xi} from the known values of the x_i-th variable, as will be discussed in more detail in the next section. Finally, cancellation of the cofficient $\delta\vec{x}$ in (3.10e) returns the *Euler-Lagrange equations*, i.e., n-ODEs that govern the evolution of the adjoint variables, while m algebraic equations for the controls are obtained by placing $\delta\vec{u} = 0$ in the same line of the expression. Thus, the three necessary systems governing the resolution of the problem and allowing the search for the optimal solution among the existing ones were obtained, which will now be analyzed.

3.2.1 Transversality and Optimality conditions

Previously, expressions of the equation (3.10 defining the boundary conditions for optimality were introduced. In detail, they are compounded by a set of ODEs that control how times (2 transversality conditions) and states (2n optimality conditions) at the trajectory extremal points should behave [**18**].

By nullifying the respective multiplicative coefficients and reformulating the expressions, one obtains:

$$\mathcal{H}_0 = \frac{\partial \varphi}{\partial t_0} + \vec{\mu}^T \frac{\partial \vec{\mathcal{X}}}{\partial t_0} \tag{3.11a}$$

$$\mathcal{H}_f = -\frac{\partial \varphi}{\partial t_f} - \vec{\mu}^T \frac{\partial \vec{\mathcal{X}}}{\partial t_f} \tag{3.11b}$$

$$\vec{\lambda}_0^T = \frac{\partial \varphi}{\partial \vec{x_0}} + \vec{\mu}^T \frac{\partial \vec{\mathcal{X}}}{\partial \vec{x_0}} \tag{3.11c}$$

$$\vec{\lambda}_f^T = -\frac{\partial \varphi}{\partial \vec{x_f}} + \vec{\mu}^T \frac{\partial \vec{\mathcal{X}}}{\partial \vec{x_f}} \tag{3.11d}$$

First, an initial or final parameter is said to be *free* if it does not appear in the end-point constraint $\vec{\mathcal{X}}$. From the two transversality equations (3.11a - 3.11b) particular conditions on the Hamiltonian are obtained depending on whether time t is constrained or not. At the point when time is constrained, i.e., $t \in \vec{\mathcal{X}}$, it is desired that it does not change with respect, so the derivatives at the initial and final times are zero. Consequently, equations (3.11a) and (3.11b) do not exist/can not be written: therefore, having nothing to associate with $\mathcal{H}$, the Hamiltonian is said to be free and subject to optimization. Conversely, when time is admitted to be free and allowed to vary, it becomes an unconstrained variable and thus $t \notin \vec{\mathcal{X}}$. If it does not even appear in φ (but in this paper, it will always be considered $\varphi = m_f$), both derivatives cancel, the Hamiltonian is zero at that point, both for initial and final times, and the value of t is the object of optimization.

A useful example to understand this may be that of a mission in which there is a requirement to produce a given thrust T in a constrained time window Δt: since both the initial epoch t_0 and the final epoch $t_f = t_0 + \Delta t$ are fixed, it follows from (3.11a) and (3.11b) that $\mathcal{H}_0 \neq 0$ and $\mathcal{H}_f \neq 0$ respectively. Dually, if the presented scenario requires the same thrust T but without imposing a constraint on the time t at which it is to be supplied by the engine, t_0 is assigned (instant at which to start thrusting) and thus $\mathcal{H}_0$ free, while $\mathcal{H}_f = 0$ because t_f is unconstrained and the object of optimization.

Similarly, one reason for optimality conditions (3.11c) and (3.11d), which represent the variation of the merit function and constraints with respect to states, and $\vec{\lambda}$ also appear in them. If a constraint is imposed on the generic state variable x_i, it is wanted not to vary relative to any state x of the system, so the corresponding adjoint variable λ_{x_i} is undefined and free (there is nothing to be associated with it in the equation). Otherwise, if the considered state is not assigned ($x_i \notin \vec{\mathcal{X}}$) and does not appear in φ, both derivatives in the expression cancel out, and it is inferred that the associated adjoint variable is $\lambda_{xi} = 0$ at that point. A scenario that often recurs and helps to understand this is a Hohmann transfer from initial radius r_0 and final radius r_f, both fixed by mission requirements. As a consequence, one would have the respective λ_{ri} and λ_{rf} free variables.

Considering, for example, the final radius bound $r_f \in \vec{\mathcal{X}}$ from (3.11d) one has:

$$\lambda_{r_f} = \cancelto{0}{\frac{\partial m_f}{\partial r_f}} + \mu_{r_0} \cancelto{0}{\frac{\partial r_0}{\partial r_f}} + \mu_{\theta_0} \cancelto{0}{\frac{\partial \theta_0}{\partial r_f}} + ... + \mu_{r_f} \cancelto{1}{\frac{\partial r_f}{\partial r_f}} + ... = \ \mu_{r_f} \tag{3.12}$$

In which a spherical coordinate system was considered.

Since μ_{r_f} is an optimization object value, λ_{r_f} is a free variable. Once the solution has reached convergence, and thus the $\vec{\lambda}$ have been determined, ideally, one can find out what the Lagrange multipliers were that would have allowed the equations to be solved at the beginning. If, on the other hand, the radius is unconstrained and subject to optimization, the derivative $\partial r_f / \partial r_f$ would also be zero since $r_f \notin \vec{\mathcal{X}}$, and thus the associated $\lambda_{r_f} = 0$. Finally, it is essential to make a remark about the equations analyzed. (3.11c) and (3.11d) are *multiple* equations, so they will each be equal in number to those of the states of the system under consideration. Expressions (3.11a) and (3.11b), instead, are *scalars*: in fact, the Hamiltonian is nothing but a number derived as (3.9).

3.2.2 Controls and adjoint variables equations

The cancellation of the multiplicative coefficients in line (3.10e) of the equation (3.10) allows the extraction of the set of ODEs that close the necessary optimal conditions. Specifically, from the annulment of the δx coefficient, one derives the *Euler-Lagrange equations* for the adjoint variables:

$$\frac{d\lambda}{dt} = -\left(\frac{\partial \mathcal{H}}{\partial x}\right)^T \tag{3.13}$$

These equations express how the adjoint variables evolve over time t. Since they are uniquely associated with the states x of the problem, and since $x \in \mathbb{R}^n$, the (3.13) will also be equal in number to n: hence $\dot{\lambda} \in \mathbb{R}^n$. The newly derived set of ODEs will be coupled to the equations of dynamics (3.1). The adjoint variables play a crucial role in solving the OCPs: in fact, the pivotal problem of indirect methods is precisely to find the λ, which represent the *accelerators* of the state variables associated at the beginning of the trajectory (always remaining in the context of space trajectories optimization)[3].

---

[3] A costate variable is akin to a Lagrange multiplier and, as such, it is in the nature of a valuation variable, measuring the shadow price of an associated state variable.

However, understanding what initial values the costates take and, subsequently, how they evolve over time along the trajectory itself is very difficult, partly because it is not always possible to make a physical association with λ. These numerical problems are elegantly summarized in the following quote from [**19**]:

> *The main difficulty with these methods is getting started; i.e., finding a first estimate of the unspecified conditions at one end that produces a solution reasonably close to the specified conditions at the other end. The reason for this peculiar difficulty is the extremal solutions are often very sensitive to small changes in the unspecified boundary conditions. ... Since the system equations and the Euler-Lagrange equations are coupled together, it is not unusual for the numerical integration, with poorly guessed initial conditions, to produce "wild" trajectories in the state space. These trajectories may be so wild that values of x(t) and/or* $\lambda(t)$ *exceed the numerical range of the computer!*

In the same row as the (3.10), by canceling the δu coefficient, one finds the *equations for the controls*:

$$\left(\frac{\partial \mathcal{H}}{\partial u}\right)^T = 0 \tag{3.14}$$

Since the controls $u \in \mathbb{R}^m$, then there will exist m algebraic equations of the type (3.14). As mentioned previously, there may be cases of problems in which a constraint is placed on the control variable u, such as the restriction $u(t) \in \mathcal{U}$ for all $t \in [0, T]$, where $\mathcal{U}$ denotes some bounded control set. The control set can in fact be a closed, convex set and this means that corner solutions can be admitted: for example, a specific control variable u must be kept in a range of $u_{min} \leq u \leq u_{max}$ limit values, as might be the case for a satellite attitude angle or thrust T, which cannot take on negative values.

In the thesis work presented, $u \in \mathcal{U}$ is considered. In this scenario, the optimal control $u^* \in \mathcal{U}$ for the desired trajectory is the one that, per each point in the trajectory, extremizes the Hamiltonian in equation (3.9) in that specific point [**20**]. Such a concept is known as Pontryagin's Maximum Principle (PMP) (for a maximization problem, otherwise it is known as Pontryagin's minimum Principle (PmP), which is a particular Mayer problem. PMP is a collection of conditions that must be satisfied by solutions of an OCP, and it unifies many classical necessary conditions from the calculus of variations.

An overview of this principle is well described in [**21**]. Furthermore, the principle is valid whether the control is restricted within a region of validity $\mathcal{U}$ or not. In either case, the value of the optimal control must always be such that the Hamiltonian is maximized at every point on the trajectory so that the functional $\mathcal{J}$ is maximized, hence:

- If the control is bounded within a domain of admissibility $\mathcal{U}$, the law of the optimal control is that returned by the (3.13) equation;
- If the control is unbounded, the optimal value will be forced to be one of the two extremes of the interval $\mathcal{U}$ (either the maximum or the minimum).

Depending then on whether the $\mathcal{H}$ in equation (3.9) is linear or affine (i.e., first-order) with the control, the solution of (3.14) leads to two different case studies:

$$\frac{\partial H}{\partial u_i} = \begin{cases} K_{u_i} & \text{if } \mathcal{H} \text{ is affine with } u \\ f(u_i) & \text{otherwise} \end{cases} \tag{3.15}$$

Where K_{u_i} is a constant. If the Hamiltonian depends linearly on u_i, the latter disappears from the expression (3.14): the system is indeterminate and gives no information about the optimal control (except in the case where $K_{u_i} = 0$). Conversely, one would like to obtain an equality by which it is possible to understand how u should vary over time, but this is not possible when affine to u: the problem, therefore, becomes *bang-bang* and is precisely the case arising in the implemented OCP. Specifically, when $K_{u_i} \neq 0$, to comply with the PMP, the optimal control is extremized to maximize the Hamiltonian: if $K_{u_i} > 0$ then the maximum allowable control $u_i = \mathcal{U}_{i,max}$ is placed; while the minimum allowable control $u_i = \mathcal{U}_{i,min}$ is chosen when $K_{u_i} < 0$. The case that will be analyzed in section (3.5) will see the Hamiltonian affine to the thrust control variable T: deriving $\mathcal{H}$ with respect to T will result in a constant. Thus, *bang-bang control* is used where T will be allowed to vary between its maximum value T_{max} (maximum propulsive effort suppliable by the spacecraft engine) and minimum value T_{min} (i.e., 0, corresponding to the condition of engine off and coasting phase, since in space there is no concept of "*retro-thrust*", so T cannot be negative). The K_{u_i} discriminant, which will ensure maximization of the Hamiltonian by the optimal control, would be the so-called Switching Function ($\mathcal{S}_F$).

The limit scenario $K_{u_i} = 0$ will not be treated in this thesis for the sake of brevity and because it is not of interest. However, it can be said that this condition involves singular arcs and more details can be found in [**13**].

3.3 Multi-Point Boundary Value Problem

A MPBVP arises when it is necessary to impose constraints on the internal points of the trajectory (by fixing, for example, a thrust arc rather than a coasting arc) to segment the general problem into a series of smaller, easily solved sub-problems. Consequently, converting from a TPBVP to a MPBVP has the undoubted benefit of improving convergence and increasing the robustness of the code, thereby facilitating the computational model. This transition is performed by subdividing the trajectory into a number n_p of subintervals, commonly known as *arcs* (or *phases*), along which the variables are continuous. The subdivision is conveniently performed to set discontinuities and constraints of the computational domain at the edges between two adjacent arcs. Operating according to this procedure, the problem described in the equations by (3.1, 3.2, and 3.3) is converted into a MPBVP, whose schematic representation of the distribution domain is shown in the figure (3.1)[4].

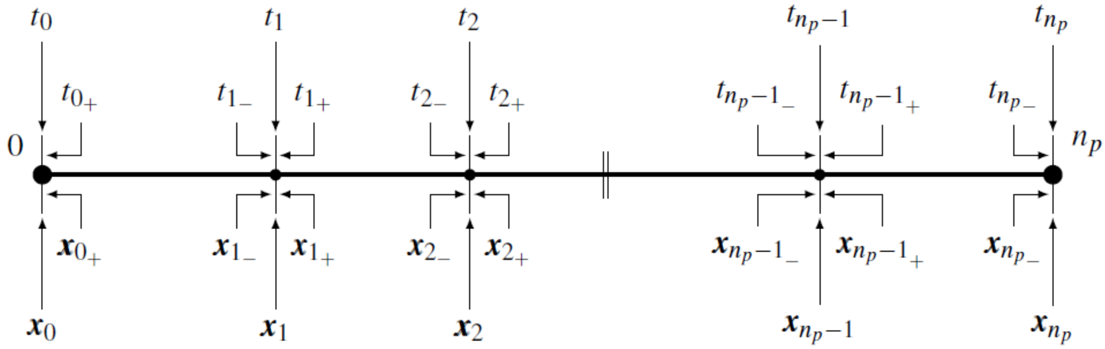

Figure 3.1: Trajectory discretization in n_p intervals in a MPBVP.

As can be seen, the *j-th* arc begins at $t_{(j-1)_+}$ and ends at $t_{(j)_-}$ and has a generic time extension of Δt_j, usually unknown and subject to optimization, which may also be different between one arc and another. Coincident with the same edges are the extremes of the vector of state variables in the form $x_{(j-1)_+}$ and $x_{(j)_-}$, where the notation + and - is used to indicate their values before and after a generic edge, respectively, while their values are continuous within each arc. However, it is important to emphasize once again that discontinuities may occur in the *internal boundaries* between two arcs.

Consequently, however, it is necessary to determine the vector of BCs equations on each border between a pair of adjacent arcs, as it can be a function of both state and time variables. This vector, which includes not only the internal points but also the external boundaries of the domain, can be reformulated as:

$$\mathcal{X}\left(\vec{x}_{(j-1)_+}, \vec{x}_{(j)_-}, t_{(j-1)_+}, t_{(j)_-}\right) = 0, \qquad j = 1, ..., n_p \tag{3.16}$$

and are Non-Linear (NL) and mixed conditions, in general. Similarly, the merit index introduced in (3.3), in a MPBVP takes the form:

---

[4] Source: Luigi Mascolo, *Low-Thrust Optimal Escape Trajectories from Lagrangian Points and Quasi-Periodic Orbits in a High-Fidelity Model*, PhD Thesis for Politecnico di Torino, 03 February 2023, page 93.

$$\mathcal{J} = \varphi\left(\vec{x}_{(j-1)_+}, \vec{x}_{(j)_-}, t_{(j-1)_+}, t_{(j)_-}\right) + \sum_{j=1}^{n_p}\int_{t_{(j-1)_+}}^{t_{(j)_-}} [\Phi(\vec{x}(t), \vec{u}(t), t)]dt \tag{3.17}$$

Note that the term associated with the Mayer formulation φ now depends on the values that the variables and time take on each border from $j_p = 0$ to $j_p = n_p$, both for the complete trajectory and for each arc. The sum of the integrals representing Lagrange's formulation remains identical to before, continuing to depend on the time evolution of the state variables, controls, and time itself: now, it takes into account how the solution evolves arc by arc.

The augmented index of merit of (3.6) in a MPBVP will be written as:

$$\mathcal{J}^* = \varphi + \vec{\mu}^T\vec{\mathcal{X}} + \sum_{j=1}^{n_p}\int_{t_{(j-1)_+}}^{t_{j-}}\left[\Phi + \vec{\lambda}^T(\vec{f} - \dot{\vec{x}})\right]dt \tag{3.18}$$

and intergrating by parts gives:

$$\mathcal{J}^* = \varphi + \vec{\mu}^T\vec{\mathcal{X}} + \sum_{j=1}^{n_p}\left(\vec{\lambda}^T_{(j-1)_+}\vec{x}_{(j-1)_+} - \vec{\lambda}^T_{j-}\vec{x}_{j-}\right) + \sum_{j=1}^{n_p}\int_{t_{(j-1)_+}}^{t_{j-}}\left[\Phi + \vec{\lambda}^T\vec{f} + \dot{\vec{\lambda}}^T\vec{x}\right]dt \tag{3.19}$$

Since the objective always remains the extremisation of $\mathcal{J}^*$ through the application of the first-order necessary condition for optimality $d\mathcal{J}^* = 0$, one has, for each arc:

$$\delta\mathcal{J}^* = \left(\frac{\partial\varphi}{\partial t_{(j-1)_+}} + \vec{\mu}^T\frac{\partial\vec{\chi}}{\partial t_{(j-1)_+}} - \mathcal{H}_{(j-1)_+}\right)\delta t_{(j-1)_+} + \tag{3.20a}$$

$$+\left(\frac{\partial\varphi}{\partial t_{j_-}} + \vec{\mu}^T\frac{\partial\vec{\chi}}{\partial t_{j_-}} + \mathcal{H}_{j_-}\right)\delta t_{j_-} + \tag{3.20b}$$

$$+\left(\frac{\partial\varphi}{\partial\vec{x}_{(j-1)_+}} + \vec{\mu}^T\frac{\partial\vec{\chi}}{\partial\vec{x}_{(j-1)_+}} + \vec{\lambda}^T_{(j-1)_+}\right)\delta\vec{x}_{(j-1)_+} + \tag{3.20c}$$

$$+\left(\frac{\partial\varphi}{\partial\vec{x}_{j_-}} + \vec{\mu}^T\frac{\partial\vec{\chi}}{\partial\vec{x}_{j_-}} - \vec{\lambda}^T_{j_-}\right)\delta\vec{x}_{j_-} + \tag{3.20d}$$

$$+\sum_{j=1}^{n_p}\int_{t_{(j-1)_+}}^{t_{j_-}}\left[\left(\frac{\partial\mathcal{H}}{\partial\vec{x}} + \dot{\vec{\lambda}}^T\right)\delta\vec{x} + \frac{\partial\mathcal{H}}{\partial\vec{u}}\delta\vec{u}\right]dt, \qquad j = 1, ..., n_p \tag{3.20e}$$

Nullifying (3.20) one obtains again the *transversality conditions* (4.19 a and b) and the *optimality conditions* (4.19 c and d) which, in the MPBVP domain, are

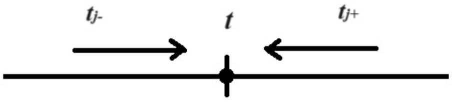

Figure 3.2: Detail on generic $j - th$ edge of the domain.

more efficient to express in relation to the $j - th$ border. Adopting the notation in the figure (3.2), (3.11) can be written as:

$$\mathcal{H}_{j_+} = \frac{\partial \varphi}{\partial t_{j_+}} + \vec{\mu}^T \frac{\partial \vec{\mathcal{X}}}{\partial t_{j_+}} \qquad j = 0, ..., n_p - 1 \tag{3.21a}$$

$$\mathcal{H}_{j_-} = -\frac{\partial \varphi}{\partial t_{j_-}} - \vec{\mu}^T \frac{\partial \vec{\mathcal{X}}}{\partial t_{j_-}} \qquad j = 1, ..., n_p \tag{3.21b}$$

$$\vec{\lambda}^T_{j_+} = \frac{\partial \varphi}{\partial \vec{x_{j_+}}} + \vec{\mu}^T \frac{\partial \vec{\mathcal{X}}}{\partial \vec{x_{j_+}}} \qquad j = 0, ..., n_p - 1 \tag{3.21c}$$

$$\vec{\lambda}^T_{j_-} = -\frac{\partial \varphi}{\partial \vec{x_{j_-}}} + \vec{\mu}^T \frac{\partial \vec{\mathcal{X}}}{\partial \vec{x_{j_-}}} \qquad j = 1, ..., n_p \tag{3.21d}$$

Note how relations (3.21c and 3.21d) refer to the boundaries after and before an interval: when several sub-arcs are present, they are also valid at the intervals of the arcs and become *continuity equations*. Furthermore, time t is never present in (3.21c and 3.21d): when they are time-independent and the final time is assigned, (3.21a and 3.21b) are meaningless (do not exist/can not be written) and, consequently, the Hamiltonian is *free*. When, on the other hand, even for a single arc, the time is allowed to vary ($t_f \notin \mathcal{X}$), it means that it is subject to optimization by the code: equations will have to be added, which will be derived from (3.21a and 3.21b), because in the differential system, there is no constraint that indicates how the time varies optimally, so the Hamiltonian is *null*.

A note worthy of attention, moreover, is the following: equations (3.21c and 3.21d) are *multiple* because they are one for each state variable. Thus, if, for example, the state of the problem is described by seven variables (considering for illustrative purposes a spherical reference system r, θ, ϕ, u, v, w, m), then there will be seven equations in (3.21c) and seven equations in (3.21d). Expressions (3.21a) and (3.21b), on the other hand, are *scalar* since the Hamiltonian $\mathcal{H}$ is a scalar number, analogous to what was seen in section (3.2.1). The considerations on the Euler-Lagrange equations for added variables and controls formulated in section (3.2.2) also hold true in the MPBVP.

3.4 Boundary Value Problem implementation

This section will outline the implementation of the Boundary Value Problem (BVP), under the OCT, also highlighting the techniques used to cope with the computational complexity. The problem of a low-thrust spatial trajectory subject to gravitational influence in a more or less articulated model requires the application of precise control and optimization procedures of the indirect method, so that an adequate robustness of the code can face possible numerical instabilities that may arise and thus achieve convergence of results.

The problem, therefore, is highly non-linear in nature. To avoid these criticalities, a BVP is formulated using OCT: in detail, the initial BVP is converted into an augmented dual one in which some values of the initial state may be unknown. Although this strategy leads to the formulation of a dimensionally more complex problem, it allows, on the other hand, the imposition of the conditions previously seen to guarantee the optimality of the solution. Accordingly, the initial state vector is identical to before but extended with the vector of adjoint variables:

$$y_0^* = \left\{ (x^*)^T \quad (\lambda^*)^T \right\}^T \tag{3.22}$$

Generally speaking, solving the BVP consists in using an indirect single-shooting method that, through an iterative generation of a series of initial guesses, determines the optimal initial conditions of the state variables (3.22) that allows reaching the desired final state y_f^* (obviously within a certain numerical tolerance), respecting all BCs, both the imposed and the optimality ones. As is immediately apparent, the result will depend heavily on the initial guesses, a typical feature of indirect methods, which is why care must be taken to guide the solution correctly to avoid errors in convergence. First of all, since the time extension Δt between two arc boundaries is unknown, it is convenient to introduce a new independent non-dimensional time variable to fix the extremes of the integration interval of each *j-th* arc:

$$t_\varepsilon = j - 1 + \frac{t - t_{j-1}}{t_j - t_{j-1}} = j - 1 + \frac{t - t_{j-1}}{\Delta t_j} \tag{3.23}$$

where:

$$\Delta t_j \triangleq t_j - t_{j-1} \qquad j = 1, ..., n_p \tag{3.24}$$

With Δt_j unknown and subject to optimization. This strategy simplifies the solution of the problem by making it more flexible and robust. The generic form of the complete set of ODEs of the indirect method is reformulated as:

$$\dot{y} = \left\{ f\left(y(t), t\right) \right\} \tag{3.25}$$

which is written in the dimensionless form:

$$\dot{\breve{y}} = f\left(\breve{y}(t_\varepsilon), t_\varepsilon\right) \tag{3.26}$$

including state and adjoint variables. An OCP may also contain some constant variables. Therefore, a new vector is introduced:

$$\vec{z} = \left\{ \vec{y}^T \quad \vec{c}^T \right\} \tag{3.27}$$

to account for the vector of constants $\vec{c}$. Through (3.23), the set ODEs can be reformulated as:

$$\dot{\breve{z}} = \frac{d\breve{z}}{dt_\varepsilon} = f\left(\breve{z}(t_\varepsilon), t_\varepsilon\right) \tag{3.28}$$

with

$$\dot{\breve{c}} = \frac{d\breve{c}}{dt_\varepsilon} = 0 \tag{3.29}$$

The new set of BCs will be satisfied if

$$\mathcal{X}(\breve{s}) = 0 \tag{3.30}$$

with $\breve{s}$ vector containing the value of the variables at both the inner and outer edges in the discretized domain,

$$\hat{s} = \left\{ \breve{y}_0{}^T \quad \breve{y}_1^T \quad .... \quad \breve{y}_{n_p-1}^T \quad \breve{y}_{n_p}^T \quad \breve{c}^T \right\} \tag{3.31}$$

Once the problem has been set, therefore, it is necessary to determine the optimal guesses that allow the desired final state to be reached within the constraints imposed: the *single-shooting* procedure, thus, must find the optimal initial state $\breve{q}_0^*$ that satisfies the BCs $\mathcal{X}(\breve{q}^*) = 0$. This will be performed iteratively. Having fixed a generic initial guess $\breve{q}_r = \breve{z}_0$ as the initial vector of variables, at each *r-th* iteration, the deviation on the BCs $\mathcal{X}(\breve{q}_r) = \mathcal{X}_r$ will be calculated (from now on, this less burdensome notation will be used).

The aim is to annul this difference to obtain the desired final state. This was done using a *differential correction* through a first-order truncated Taylor series expansion of the vector of constraints, thanks to which it was possible to update the initial state:

$$\mathcal{X}_{r+1} = \mathcal{X}_r + \frac{\partial \mathcal{X}_r}{\partial \breve{q}_{r+1}}(\breve{q}_{r+1} - \breve{q}_r) \tag{3.32}$$

The BCs at the next iteration, therefore, from (3.32), are a function not only of the BCs at the previous step but also of the state vector at the previous *r-th* one. In (3.32), in particular, there appears the partial derivative of the constraints vector concerning the forward in-time free-variable vector called *Jacobian matrix* $\breve{\mathfrak{J}}$ (henceforth referred to as 3.33). This matrix is no more than a partial mapping of the derivative of the constraints $\mathcal{X}_r$ with respect to the variables of the problem q_{r+1}, explicitly stated in (3.34).

$$\breve{\mathfrak{J}}\left(\mathcal{X}_r\right) \triangleq \breve{\mathfrak{J}}\left(\mathcal{X}_r, \breve{q}_{r+1}\right) \tag{3.33}$$

$$\breve{\mathfrak{J}} = \begin{bmatrix}
\frac{\partial \mathcal{X}_1}{\partial q_{01}} & \frac{\partial \mathcal{X}_1}{\partial q_{02}} & \frac{\partial \mathcal{X}_1}{\partial q_{03}} & \frac{\partial \mathcal{X}_1}{\partial q_{04}} & \frac{\partial \mathcal{X}_1}{\partial q_{05}} & \frac{\partial \mathcal{X}_1}{\partial q_{06}} & \frac{\partial \mathcal{X}_1}{\partial q_{07}} \\
\frac{\partial \mathcal{X}_2}{\partial q_{01}} & \frac{\partial \mathcal{X}_2}{\partial q_{02}} & \frac{\partial \mathcal{X}_2}{\partial q_{03}} & \frac{\partial \mathcal{X}_2}{\partial q_{04}} & \frac{\partial \mathcal{X}_2}{\partial q_{05}} & \frac{\partial \mathcal{X}_2}{\partial q_{06}} & \frac{\partial \mathcal{X}_2}{\partial q_{07}} \\
\frac{\partial \mathcal{X}_3}{\partial q_{01}} & \frac{\partial \mathcal{X}_3}{\partial q_{02}} & \frac{\partial \mathcal{X}_3}{\partial q_{03}} & \frac{\partial \mathcal{X}_3}{\partial q_{04}} & \frac{\partial \mathcal{X}_3}{\partial q_{05}} & \frac{\partial \mathcal{X}_3}{\partial q_{06}} & \frac{\partial \mathcal{X}_3}{\partial q_{07}} \\
\frac{\partial \mathcal{X}_4}{\partial q_{01}} & \frac{\partial \mathcal{X}_4}{\partial q_{02}} & \frac{\partial \mathcal{X}_4}{\partial q_{03}} & \frac{\partial \mathcal{X}_4}{\partial q_{04}} & \frac{\partial \mathcal{X}_4}{\partial q_{05}} & \frac{\partial \mathcal{X}_4}{\partial q_{06}} & \frac{\partial \mathcal{X}_4}{\partial q_{07}} \\
\frac{\partial \mathcal{X}_5}{\partial q_{01}} & \frac{\partial \mathcal{X}_5}{\partial q_{02}} & \frac{\partial \mathcal{X}_5}{\partial q_{03}} & \frac{\partial \mathcal{X}_5}{\partial q_{04}} & \frac{\partial \mathcal{X}_5}{\partial q_{05}} & \frac{\partial \mathcal{X}_5}{\partial q_{06}} & \frac{\partial \mathcal{X}_5}{\partial q_{07}} \\
\frac{\partial \mathcal{X}_6}{\partial q_{01}} & \frac{\partial \mathcal{X}_6}{\partial q_{02}} & \frac{\partial \mathcal{X}_6}{\partial q_{03}} & \frac{\partial \mathcal{X}_6}{\partial q_{04}} & \frac{\partial \mathcal{X}_6}{\partial q_{05}} & \frac{\partial \mathcal{X}_6}{\partial q_{06}} & \frac{\partial \mathcal{X}_6}{\partial q_{07}} \\
\frac{\partial \mathcal{X}_7}{\partial q_{01}} & \frac{\partial \mathcal{X}_7}{\partial q_{02}} & \frac{\partial \mathcal{X}_7}{\partial q_{03}} & \frac{\partial \mathcal{X}_7}{\partial q_{04}} & \frac{\partial \mathcal{X}_7}{\partial q_{05}} & \frac{\partial \mathcal{X}_7}{\partial q_{06}} & \frac{\partial \mathcal{X}_7}{\partial q_{07}}
\end{bmatrix} \tag{3.34}$$

Understanding this matrix is crucial to fully grasp how *differential correction* operates, as it linearly traces final variations to initial conditions, or vice versa, and multiplies the term $(\breve{q}_{r+1} - \breve{q}_r)$. Thus, it offers significant insights, both quantitative and qualitative, into how little variations in $\breve{q}_r$ can affect the evolution of the problem and, consequently, the guess correction at each iteration.

If a solution exists, then $X_{r+1} = 0$ and the iterative solution takes the form

$$\mathcal{X}_r + [\breve{\mathfrak{J}}\left(\mathcal{X}_r\right)](\breve{q}_{r+1} - \breve{q}_r) = 0 \tag{3.35}$$

and, by inverting, one determines the state of the design vector q_r at each iteration and the update value of the constraint vector X_r

$$\breve{q}_{r+1} = \breve{q}_r - [\breve{\mathfrak{J}}\left(\mathcal{X}_r\right)]^{-1}\mathcal{X}_r \tag{3.36}$$

in which the Jacobian matrix is computed by a *forward finite difference* approximation as

$$\breve{\mathfrak{J}}\left(\mathcal{X}_r\right) = \frac{\mathcal{X}_r^p - \mathcal{X}_r}{\Delta} \tag{3.37}$$

where $\mathcal{X}_r^p$ represents the vector of constraints associated with the perturbation vector q^p (the notation p stands for *perturbed*), while Δ is the magnitude of the perturbation, in this work set to a value of $\Delta = 1 \times 10^{-7}$.

$$\mathcal{X}_{ir}{}^{p} \triangleq \mathcal{X}(q_{ir}{}^{p}) \tag{3.38a}$$

$$q_{ir}{}^{p} \triangleq q_{ir} + \Delta \tag{3.38b}$$

Inevitably, the *differential correction* procedure described introduces a certain level of approximation in the calculation of the solution, but it is a compromise that one is willing to accept to make the analysis faster and more flexible and, above all, it helps to have some stability in a problem where one is varying the initial conditions with different constraints and BCs.

At this stage, the OCP thus formulated as a TPBVP can be resolved by determining the optimal initial state z_0^* that allows the trajectory to evolve towards the desired final state $z_f^*(z_0^*(t), t)$, respecting the BCs. For this purpose, a simultaneous integration of the set of system principal ODEs, given below, is performed:

$$\dot{z} = f\left(z(t), t\right) \tag{3.39}$$

The integration of the 3.39) took place numerically in a Python environment thanks to the utilization of the LSODA package precompiled in C++ [**22**], which implements the Adams-Moulton method of order 13 (adaptive step with variable order from 1 to 13). This choice is based on the pursuit of an optimal balance between code efficiency and calculation speed was pursued: since the integration part takes place in a precompiled code, a percentage improvement over the execution time of the *scipy.solve ivp* package of 59510.7% was estimated (approximately 60 thousand times faster) while still maintaining the flexibility and simplicity of the *Python* environment.

Finally, it was mentioned earlier how the iterative procedure of *differential correction* can induce divergences and compromise the convergence of the solution. Two strategies involving the application of two relaxation factors were used to refine the calculation process and avoid these criticalities, as described below:

1. A relaxation factor k_1 introduced during the update of the new guess initial condition at each iteration, which ensures the convergence of the solution:

   $$z_{r+1} = z_r - k_1 \cdot \left[\mathcal{J}\left(\mathcal{X}_r\right)\right]^{-1} \mathcal{X}_r \tag{3.40}$$

   Where $k_1 = [0.1 - 1]$. Typically, low values of k_1 are set during the first row guess for unknown values, while high values of k_1 are suitable when the solution is reasonably close to the optimum.

2. A control factor k_2 on the subsequent error with respect to the errors on the boundary conditions of the previous step:

$$E_{max,r+1} < k_2 E_{max,r} \tag{3.41}$$

   Where $E_{max} = norm_i(\mathcal{X}_i)$ is the code required accuracy and $k_2 = [2 - 3]$, but if the error should become significantly high then a bisection method is performed on the correction of k_2 up to 5 times, and the (3.41) is not satisfied. This parameter is suitable for helping the first step of the iterative process to converge, establishing the correct direction of optimality in the search space. It is essential to note how the correction is performed on the *error norm*.

The table (3.2) summarises the values used in the calculation procedure.

Table 3.2: Parameters used in the calculation procedure.

Integrator	LSODA
Factor k_1	0.01
Factor k_2	2
Delta Δ	1×10^{-7}

3.5 OCP for spacecraft trajectory optimization

This section shows how the OCT discussed above applies to the trajectory optimization problem of a spacecraft. Considering the latter in a 2-body system in the absence of perturbative accelerations, its dynamic is described by the following set of ODEs:

$$\frac{d\vec{r}}{dt} = \vec{v} \tag{3.42a}$$

$$\frac{d\vec{v}}{dt} = \vec{g} + \frac{\vec{T}}{m} \tag{3.42b}$$

$$\frac{dm}{dt} = -\frac{\vec{T}}{c} \tag{3.42c}$$

Which explicitly written by projecting them along the three Cartesian axes of an Earth-Centred Earth-Fixed (ECEF) RF become:

$$\frac{dx}{dt} = v_x \tag{3.43a}$$

$$\frac{dy}{dt} = v_y \tag{3.43b}$$

$$\frac{dz}{dt} = v_z \tag{3.43c}$$

$$\frac{dv_x}{dt} = -\frac{\mu_\oplus}{r^{3/2}}x + \frac{T_{v_x}}{m} \tag{3.43d}$$

$$\frac{dv_y}{dt} = -\frac{\mu_\oplus}{r^{3/2}}y + \frac{T_{v_y}}{m} \tag{3.43e}$$

$$\frac{dv_z}{dt} = -\frac{\mu_\oplus}{r^{3/2}}z + \frac{T_{v_z}}{m} \tag{3.43f}$$

$$\frac{dm}{dt} = -\frac{T}{c} \tag{3.43g}$$

with $\mu_\oplus$ gravitational parameter of the Earth. At this point, the OCT aims to integrate the (3.43) to derive the optimal control law that allows maximizing the objective index, i.e., the final mass of the spacecraft (and thus minimize propellant consumption) at the end of the mission under study. This is because, as already mentioned, Mayer's formulation was preferred in this thesis, setting the Lagrangian term Φ in Bolza's general definition (3.3) to zero:

$$\mathcal{J} = \varphi = m_f \tag{3.44}$$

Starting from the definition of the state vector, although it is convenient to use the classical orbital parameters (and thus the Gauss planetary equations)

$$x_{kepl} = \{a, e, i, \Omega, \omega, \nu\}^T \tag{3.45}$$

from the perspective of targeting the desired orbits, this choice would prove to be mathematically unsuccessful since it is unknown how the target on an orbital parameter translates as a condition on the adjoint variables λ. Hence, one opts for the definition of a state vector $x(t) \in \mathbb{R}^n$ expressed in Cartesian coordinates:

$$x_{cart} = \{x, y, z, u, v, w, m\}^T \tag{3.46}$$

which proves to be more efficient for targeting transversality, with$m$ the mass of the spacecraft. Let $x_{cart} \triangleq x(t)$ be denoted henceforth for simplicity of notation.

It is known, then, from OCT that each of the variables in (3.46) is associated with its corresponding adjoint variable, thus being able to define the augmented state vector $y(t) \in \mathbb{R}^{2n}$:

$$y = \Big\{x, y, z, u, v, w, \lambda_x, \lambda_y, \lambda_z, \lambda_{v_x}, \lambda_{v_y}, \lambda_{v_z}, \lambda_m\Big\}^T \tag{3.47}$$

From the explicit set of ODEs (3.43) the derivation of the Hamiltonian $\mathcal{H}$ is immediate:

$$\begin{aligned}
\mathcal{H} = \vec{\lambda}^T\vec{f} = \sum_{i=1}^{2n}\lambda_i f_i = \lambda_x u + \lambda_y v + \lambda_z w + \\
+\lambda_u\left[-\frac{\mu_\oplus}{r^{3/2}}x + \frac{T}{m}\frac{\lambda_{v_x}}{\lambda_V}\right] + \\
+\lambda_v\left[-\frac{\mu_\oplus}{r^{3/2}}y + \frac{T}{m}\frac{\lambda_{v_y}}{\lambda_V}\right] + \\
+\lambda_w\left[-\frac{\mu_\oplus}{r^{3/2}}z + \frac{T}{m}\frac{\lambda_{v_z}}{\lambda_V}\right] + \\
+\lambda_m\frac{T}{c}
\end{aligned} \tag{3.48}$$

This can be rewritten in compact form by grouping the *thrust-to-mass ratio* terms to define what is referred to as the Switching Function ($\mathcal{S}_F$) (whose expression is given in 3.50), which plays a crucial role in optimal trajectory control:

$$\mathcal{H} = \lambda_{v_x}u + \lambda_{v_y}v + \lambda_{v_z}w - \frac{\mu_\oplus}{r^{3/2}}(x\lambda_u + y\lambda_v + z\lambda_w) + T\mathcal{S}_F \tag{3.49}$$

$$\mathcal{S}_F = \frac{\vec{\lambda}_V}{m} - \frac{\lambda_m}{c} \tag{3.50}$$

Note in (3.50) the presence of the term $\vec{\lambda}_V$ which groups the adjoint variables associated with the three velocity components:

$$\vec{\lambda}_V = \begin{Bmatrix} \lambda_{v_x} \\ \lambda_{v_y} \\ \lambda_{v_z} \end{Bmatrix}, \qquad \lambda_V = \|\vec{\lambda}_V\|. \tag{3.51}$$

and called *primer vector*, which is useful for defining the optimal thrust direction. The result of Lawden's work in 1963 [**23**], tells how the costates velocity vector must be aligned (parallel) to the velocity state vector, i.e. it finds a correlation between the norm of λ_{v_x}, λ_{v_y}, and λ_{v_z} and the norm of u, v, w. Basically, the optimal thrust angle will always be a function of the λ of velocities; in particular, the optimal thrust direction is that which maximizes the $\mathcal{S}_F$ in (3.50), which in turn maximizes the Hamiltonian $\mathcal{H}$ in equation (3.49).

The control vector $\vec{u}(t)$ is composed of the magnitude of the thrust T and its direction $\vec{u}(t) = T, \alpha$. From this, the importance of $\mathcal{S}_F$ is evident. In fact, from the (3.49) it is clear how the Hamiltonian is affine with the control T, i.e., deriving $\mathcal{H}$ with respect to the thrust, one obtains a constant and has no information on how T should vary since the control is linear.

$$\frac{\partial \mathcal{H}}{\partial T} = 0 \rightarrow 0 + \frac{1}{m}\left(\lambda_V^T - \frac{\lambda_m}{c} m\right) - 0 = 0 \tag{3.52}$$

The problem that arises, therefore, is a *bang-bang* one, i.e., to comply with PMP, the optimal control $\vec{u}^*$ is the one that maximizes the Hamiltonian $\mathcal{H}$ and the index of merit for the trajectory. In this context of maximization, the importance of $\mathcal{S}_F$ manifests itself: when $\mathcal{S}_F > 0$, then the thrust will be maximum $T = T_{max}$, while it will be null $T = 0$ when $\mathcal{S}_F < 0$ in that Δt integration interval, which will be called the *coasting arc.*

The switching function in (3.50) can then be rewritten in compact form as:

$$\mathcal{S}_F = \lambda_V - \lambda_m \frac{m}{c} \tag{3.53}$$

As regards the control of *thrust angles*, with reference to the figure (3.3), two angles are defined: an α_t angle denoting the direction of T in the orbital plane and a β_t angle defining the component in the direction perpendicular to the plane. On this basis, the thrust T can be rewritten by decomposing it into its components along the three directions:

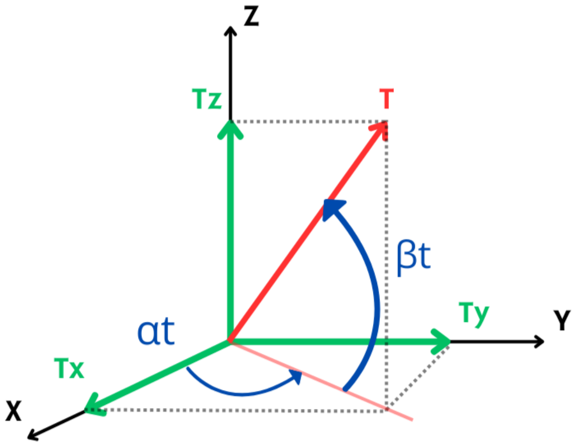

Figure 3.3: Thrust angles in the Cartesian reference frame.

$$\vec{T} = \left\{ \begin{array}{c} T_{v_x} \\ T_{v_y} \\ T_{v_z} \end{array} \right\} = T \left\{ \begin{array}{c} \sin \alpha_T \\ \cos \alpha_T \cos \beta_T \\ \cos \alpha_T \sin \beta_T \end{array} \right\}, \qquad T = \|\vec{T}\|. \tag{3.54}$$

One wants to find the optimal values of α_t and β_t that maximize the Hamiltonian $\mathcal{H}$. Accordingly, the first derivative of the latter with respect to the two angles is determined and set equal to zero, obtaining:

$$\frac{\partial \mathcal{H}}{\partial \alpha_T} = 0 = \lambda_{v_x} \cos \alpha_T - \Big(\lambda_{v_y} \cos \beta_T + \lambda_{v_z} \sin \beta_T \sin \alpha_T \Big) \tag{3.55a}$$

$$\frac{\partial \mathcal{H}}{\partial \beta_T} = 0 = -\lambda_{v_y} \sin \beta_T + \lambda_{v_z} \cos \beta_T \tag{3.55b}$$

By manipulating (3.55) appropriately, α_t and β_t are made explicit:

$$\sin \alpha_T = \frac{\lambda_{v_x}}{\lambda_V} \tag{3.56a}$$

$$\cos \alpha_T \cos \beta_T = \frac{\lambda_{v_y}}{\lambda_V} \tag{3.56b}$$

$$\cos \alpha_T \sin \beta_T = \frac{\lambda_{v_z}}{\lambda_V}, \tag{3.56c}$$

which are the cosine directors of the primer vector and also correspond to the components of the thrust vector described in the equation (3.54).

Through (3.56), therefore, the in-plane and out-of-plane angles for the optimum thrust direction are determined. The *control equations* of the problem are thus derived. Finally, the relationships for the adjoint variables specific to the case study are derived through the Euler-Lagrange equations, partially deriving the Hamiltonian as seen in the (3.13), and given in the appendix (A).

As posed, the problem is completely defined. Although its nature may seem relatively straightforward, one must take into account any discontinuities in the thrust that may occur in a moderately complex dynamic model. This could lead to very slight fluctuations around zero in the sign of the switching function, causing cascading numerical instability problems. Although this was not the case, given the relative simplicity of the adopted 2-body model and the modelised gravitational field, one way of dealing with such a critical issue could be to pre-set the structure of the $\mathcal{S}_F$ a priori. By pre-assigning a sequence of thrust and coasting arcs, obviously, with due rationality and experience, it is possible to improve stability and aid convergence, increasing the robustness of the code. However, handling push discontinuities is a typical and frequent drawback of indirect optimization.

3.6 Reduced Transversality conditions

Based on the various critical points discussed above, a long-standing challenge in optimal guidance for space trajectories is how to reduce the transversality conditions in an OCP. The reasons for doing this are mainly twofold:

- such a reduction would eliminate Lagrange multipliers (even unknown ones) from the problem, which significantly weaken the robustness of the code;
- such transversality conditions involving Keplerian parameters would allow for better and smoother targeting of orbits during trajectories, as mentioned in the previous section.

More details on this reduction can be found in [**24**]. Basically, taken the vector of Keplerian orbital parameters:

$$\vec{K} = \{a, e, i, \Omega, \omega, \nu\}^T \in \mathbb{R}^6 \tag{3.57}$$

Given the $K_i - th$ free element that does not appear in the constraint vector, in the case of $K_i = \nu$, at the final time t_f it will be:

$$\frac{\partial \psi}{\partial K_i} = \frac{\partial \psi(\vec{S_f})}{\partial \vec{S_f}} \frac{\partial \vec{S_f}}{\partial K_i} = 0, \qquad i \in \mathcal{I} \tag{3.58}$$

With $\vec{S_f}$ final state obtained from the vector of Keplerian orbital elements, ψ vector of constraints and $\mathcal{I}$ is the set of indices of the K_i free elements. Applying these reduced to optimal conditions in equation (3.11d), one introduces a vector $\vec{y}$ such that:

$$\left(\frac{\partial \psi(\vec{S_f})}{\partial \vec{S_f}} \right) \vec{y} = 0 \tag{3.59}$$

With y_i a set of linearly independent solutions of the system and $i = 1, ..., n$ and n number of free K. Equation (3.11d) can then be rewritten as

$$\vec{y}(x_f) \cdot \vec{\lambda_f} = 0 \tag{3.60}$$

and obtain $(6 - n)$ *reduced transversal conditions*:

$$\frac{\partial \vec{S_f}}{\partial K_i} \cdot \vec{\lambda_f} = 0 \tag{3.61}$$

A solution for a free-time, free-attachment orbital insertion must include the seven initial costates, the time to maneuver and the final true anomaly. Nine total unknowns require 9 boundary conditions, which are:

- **Maximum final mass**, from the *optimality condition* in equation (3.11d):

$$\lambda_{m_f} = 1 \tag{3.62}$$

- **Free-time**, from the *transversality conditions* in equation (3.11b):

$$\mathcal{H}_f = 0 \tag{3.63}$$

- **Free-attachment**, from the *reduce transversality conditions* (3.61):

$$\vec{v}_f \cdot \vec{\lambda}_{r_f} - \frac{\mu}{r_f^3}\vec{r_f} \cdot \vec{\lambda}_{v_f} = 0 \tag{3.64}$$

- **Final state BCs**:

$$\vec{r}_f = \vec{r}_f^* \tag{3.65a}$$

$$\vec{v}_f = \vec{v}_f^* \tag{3.65b}$$

where $\vec{r}_f^*$ and $\vec{v}_f^*$ indicate the desired final state, obtained by updating the required final keplerian elements with a new final true anomaly in every new iteration.

Chapter 4

Case study: LEO debris retrieval mission in 2BP

Chapter 4 illustrates the case study selected in this thesis, presenting the assumptions underlying the analyses performed and justifying these choices with appropriate criteria. In detail, in addition to discussing the succession of ideas according to which the mission's target debris was selected, the logical principles that guided the decisions in the problem definition phase will be set out, both in terms of the spacecraft's propulsive parameters and the assumptions regarding the dynamic model. The discussion will also extend to the strategies adopted to determine and optimize the trajectory, which made it possible to establish an effective methodological path. This approach facilitated the achievement of the desired results by maintaining a relatively simple calculation model without significantly increasing processing times or the complexity of the code developed.

4.1 Debris selection progress

Section 1.4 has already presented the reasons that led to the selection of the SSO orbital belt as the region of investigation for an ADR mission and will not be reported here for the sake of brevity. Coupled with this research opportunity was the intention to align with the current requirements of the major companies in the sector, with the aim of giving the work produced practical relevance and preparing it as a basis for future feasibility analysis. Therefore, it has been decided to contextualize this thesis within the ESA *Clearspace-1* initiative, which foresees the development of the first mission dedicated to the removal of a space debris fragment from its orbit by rendezvous, capture, and subsequent safe atmospheric re-entry. The debris in question is a Vega Secondary Payload Adapter (VESPA) weighing around 100 kg, which was used for the release of satellites into space after launch aboard the Italian Vettore Europeo di Generazione Avanzata (Vega) launcher in 2013. The mission is scheduled to be launched by 2026 and will have a demonstration character for the removal of space debris, thus representing a significant step towards the creation of a sustainable commercial space ecosystem. It was precisely these potential implications in terms of space sustainability and consequent reductions in risks for access to space that were decisive in the selection of this debris.

The orbital parameters for the debris were extracted from SpaceTrack's (SATellite CATalog (SATCAT) [**25**]. Since these parameters vary over time, it was necessary to establish a specific date from which to start the transfer simulation. This date, together with other information relevant to characterizing the state of the debris, is given in the table (4.1). It also includes data on the mass and dimensional characteristics of the debris, retrieved by consulting the ESA DISCOSweb database [**26**], and helpful for the analysis concerning re-entry.

Table 4.1: VESPA Upper Part Debris characteristics.

DISCOS ID	39159
Name	VESPA Upper Part
SATNO	39162
Object Class	Rocket Mission Related Object
Mass	100 kg
Maximum Cross Section	4.41 m^2
Date	2024 Jul 08 - 13:29:48.829

It should be noted that, within the 2BP model, the debris was modelled as a point mass equivalent to the real one, despite its specific geometric characteristics. Its maximum cross-section was considered to be equal to that indicated in the table. Its Keplerian parameters will then represent the final state to be reached by the spacecraft (figure 4.1).

4.2 Boundary conditions

4.2.1 Spacecraft propulsion system

This section analyses the propulsive characteristics of the spacecraft, considered within the dynamic model in which it moves as a point mass, similar to the debris. Furthermore, important considerations are made regarding the thrusters equipped by the spacecraft, which will determine the amount of thrust required to execute the orbital transfer maneuver. Section (1.2) of Chapter 1 examined in detail the potential benefits of using electric propulsion to overcome the physical limitations

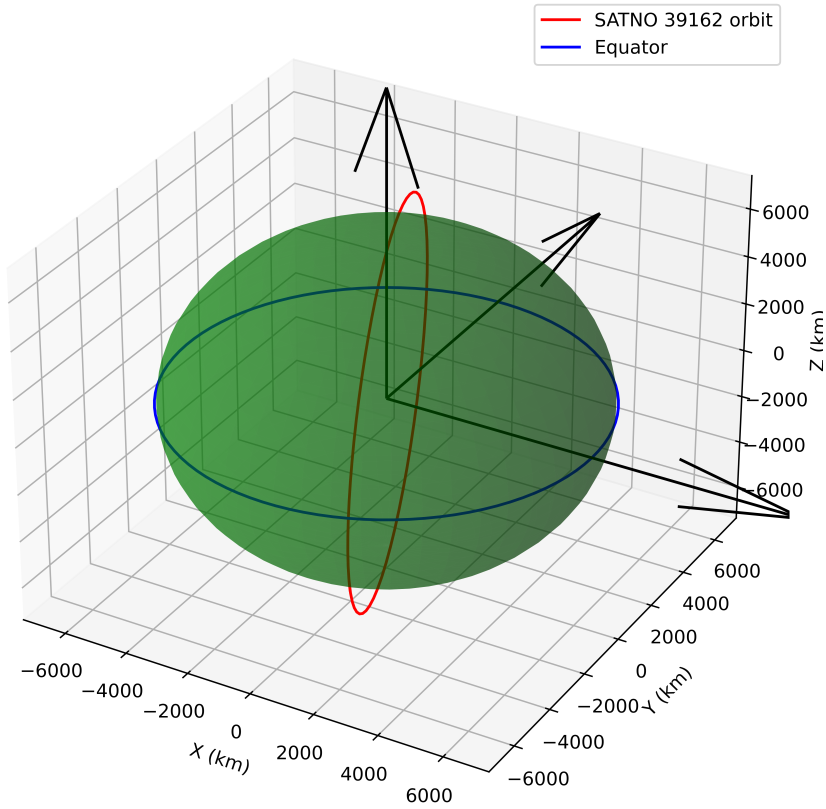

Figure 4.1: Debris Orbit.

imposed by conventional chemical propulsion systems. These benefits are associated with high specific impulses (I_{sp}), which can reach the order of thousands of seconds, although this results in lower thrusts and, consequently, longer mission times. However, since the main objective of the work is to save propellant, it was decided to opt for electric propulsion (EP), as the efficiency of the thruster is a crucial element for mission success.

For this reason, different types of electric propulsion were analyzed in order to identify the most suitable one for the mission in question; however, none of them have been selected as their performance allowed only rather limited maneuver corrections. Consequently, in order to ensure the completion of the mission within a reasonable timeframe, an electrostatic thruster with optimistic performance was chosen. Firstly, with the aim of remaining in the low-thrust domain, it has been decided to operate with a thrust ratio T_{ratio} of 25 mN per 150 kg, which allows acceleration values in the order of magnitude between $[10^{-4} - 10^{-6}]$ m/s^2 while maintaining a decent level of efficiency. Therefore, the thrust set is $T = 0.08$ N, obtained assuming a configuration of four thrusters of 0.02 N each. The available energy allows the mission to be completed, taking into account that the thrusters are only used during the approach phase to the debris when the batteries are fully charged. The specific impulse was set at a value of $I_{sp} = 1800$ s. All these assumptions discussed are summarised in the table (4.2), which also shows the initial mass of the spacecraft. All these assumptions discussed are summarised in the table (4.2), which also shows the initial mass of the spacecraft.

Table 4.2: Spacecraft characteristics.

Propulsion type	Electric propulsion
T_{ratio}	25 mN per 150 kg
Thrust T	0.08 N (4 x 0.02 N)
Specific Impulse I_{sp}	1800 s
Mass	60 kg

Thrust and specific impulse are considered constant throughout the duration of the mission (assumed total absence of throttling), resulting in the bang-bang control discussed in Section 1.2. The assumption of a relatively small spacecraft mass is justified by the specific type of mission envisaged. In fact, since the main task consists of capturing the debris and then deorbiting it by atmospheric re-entry, it does not carry any significant payload (such as advanced chambers or special sensors) except for a debris recovery system and a camera capable of providing information on the relative position of the two bodies. These elements do not significantly affect the overall weight.

In this regard, it is essential to make an important observation: in the current study, no debris removal system is assumed. At the current time, no solution has really emerged. However, not specifying a removal system does not change the current study, as it focuses primarily on the transfer to debris and not the actual de-orbiting operation. Lastly, for simplification, eclipse conditions are not considered. They increase the complexity of the transfers and generally affect the power system, and in the case of solar electric propulsion, it is typically not possible to thrust during eclipse phases.

4.2.2 Initial conditions

In order to ensure the correct execution of the transfer under analysis, it is necessary to appropriately define the initial state (starting conditions) and final state (arrival conditions) of the spacecraft. While the final conditions are well known and will be discussed in the next section, the determination of the initial conditions represents one of the main challenges of the optimization method. However, in this thesis, during the pre-simulation phase, the initial state, consisting of the three position components and the three velocity components, was defined as an equivalent state described by the six classical orbital parameters, which allows for more accurate orbit targeting. In particular, the orbit used in study [**27**] was adopted as the starting orbit, as its orbital elements are advantageously close to the initial orbit of the selected debris, both of which are shown below.

Table 4.3: Initial Keplerian elements of spacecraft and debris.

Orbit	a [km]	e [/]	i [°]	Ω [°]	ω [°]	ν [°]
Initial S/C	$R_\oplus$+700.14	0.00	97.89	121.50	36.98	346.67
Initial debris	$R_\oplus$+784.50	0.0090889	98.7245	121.42	16.57	58.8-237.67

with $R_\oplus$ mean Earth radius. Concerning the orbital parameters of the starting orbit, a clarification should be made: the Right Ascension of the Ascending Node (RAAN) shown in the table (4.3) differs from the one given in the reference paper [**27**], whose value is 268.18°. This variation was introduced to reduce the computational load and avoid excessive complexity in the calculations. The RAAN variation maneuvers, in fact, imply an orbital plane rotation, which not only requires a considerable propulsive effort but is also exceedingly time-consuming. Consider, for example, that to vary the orientation of the orbital plane by just 15°, it would require 270 days. For this reason, as there were not enough computational resources available to analyze a scenario with a variation of RAAN equal to $\Delta\Omega = 268.18° - 121.42° = 146.76°$, it was decided to slightly modify the initial orbit, opting for a RAAN that would allow for easier optimization, as shown in the figure (4.2).

A further related comment concerns the exact point at which the spacecraft will be released from the launcher. The problem lies in the fact that the entity responsible for transporting the payload into space will inevitably have other payloads to release into orbit. Generally, the practice is to calculate the arithmetic mean of the required RAANs and leave the payload in an intermediate position. However, if the release occurs in the vicinity of one of the extreme RAANs, maneuvers to change the RAAN would be particularly onerous. Thus, it is reasonable to hypothesize that, at a stage prior to the study presented here, a preliminary analysis of the satellite's commissioning phase may have been carried out, during which it drifted to the desired RAAN by exploiting the J2 perturbation due to the Earth's non-sphericity, thanks to the precession phenomenon illustrated in the section 2.4.1.

In addition to the initial state of the spacecraft given in the table (4.3), which results in a set of initial positions and velocities in Cartesian coordinates through the transformations illustrated in the section (2.1.4), it is also necessary to assign

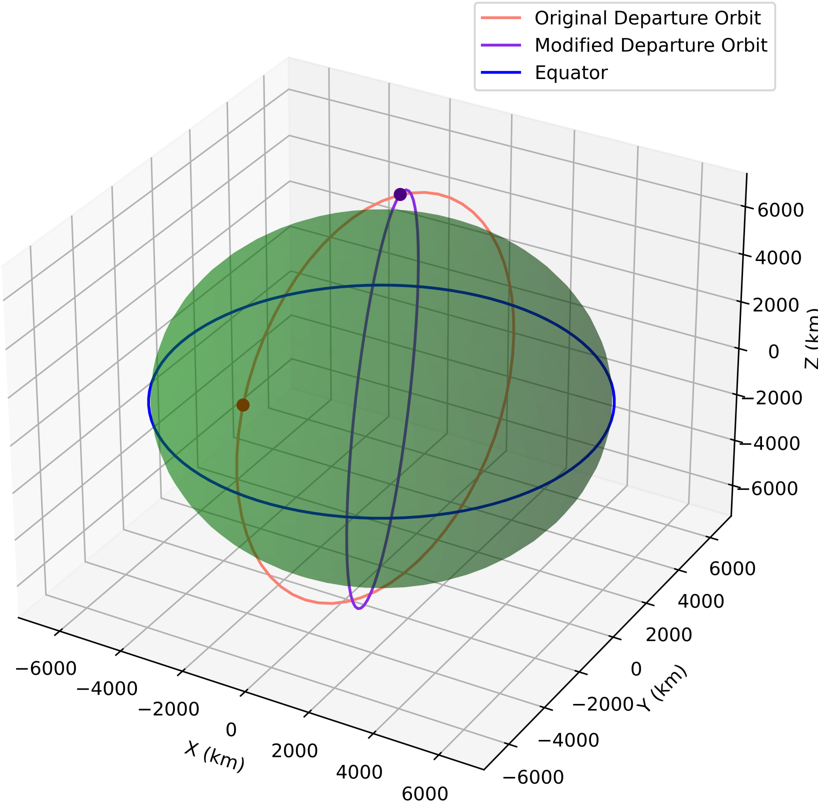

Figure 4.2: Comparison between original and modified departure orbit after $\Delta\Omega$.

the associated initial costates, i.e the additional variables of the problem that characterize the indirect method:

$$\Lambda_0 = \{\lambda_x, \lambda_y, \lambda_z, \lambda_u, \lambda_v, \lambda_w, \lambda_m\}^T \tag{4.1}$$

For convergence to be optimally achieved, it is essential to provide sufficiently plausible and consistent initial guesses. The values determined, which resulted in the convergence of the solution in both mission scenarios, can be found in Chapter 5 and are not reported here to avoid redundancy. As discussed in Chapter 3, the initial guess is somewhat of an accelerating factor for the associated state variables. For example, the position constants quantify the influence of positional coordinates on the evolution of the trajectory, and the values in the three directions x, y, and z indicate the tendency of the spacecraft to move in a specific direction in the dynamic model. The variables associated with velocity, on the other hand, indicate whether the spacecraft is accelerating (positive values) or decelerating (negative values) during a phase of the orbital journey; their modulus represents the magnitude of acceleration in the specific direction. Of the three, the one with the highest modulus will determine the main direction of thrust, which will be prioritized over the others.

The optimal quantities to be taken by the constates are not known a priori and, therefore, must be determined iteratively by trial and error. As initial guesses, non-zero values of less than unity, generally around 10^{-2}, are entered and then gradually refined to facilitate convergence of the solution. The last costate of the expression is associated with the mass trend. Since the mission involves thrust phases, it is to be expected that the propellant mass will decrease from its initial value. Consequently, λ_m will be between $[0 \div 1]$ and not too far from unity, since the mission objective is a transfer with minimum propellant consumption (values too far from unity would, in fact, indicate high consumption). Due to the fact that the transfer has been divided into two phases, the above considerations are valid for both phases, with the final state of the first one constituting the initial conditions of the second one. However, as the manoeuvring strategy changes in the second phase to allow the approach to the debris, costates will be different, although the conceptual observations described above will remain the same.

4.2.3 Terminal conditions

The final position to be reached by the spacecraft will, predictably, correspond to the orbit of the debris, and the transfer phase will be considered complete when these final conditions are met. In such a scenario, this will indicate that the spacecraft will have completed insertion into the desired orbit and completed rendezvous with the debris.

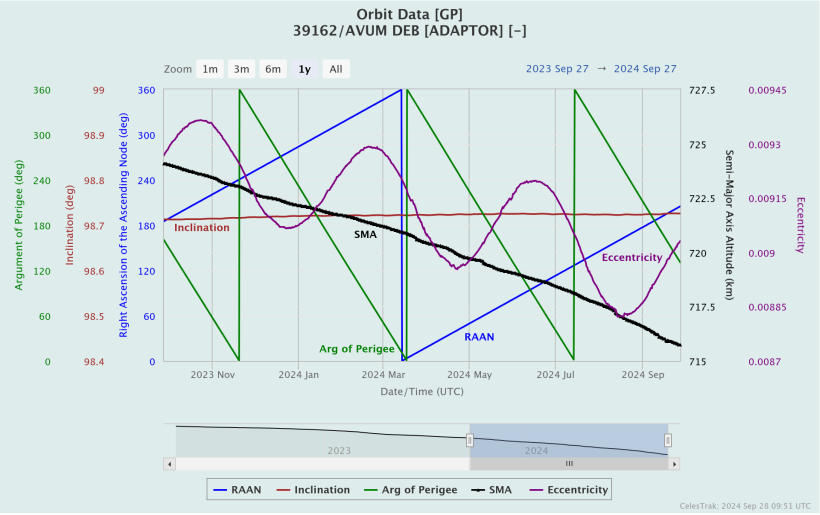

Figure 4.3: Changes in the orbital elements of the debris during the year 2024.

A note regarding debris parameters refers to the significant variations they undergo over time, as evidenced by the figure (4.3). For the complete definition of the state of the debris within the model, the 08 July 2024 date was chosen as the reference, where the Keplerian parameters of the debris are as shown in the table (4.3). For simplification, it was assumed that the target was in this configuration at the initial starting time t_0. This assumption is not particularly restrictive since, by observing the trends shown in the figure (4.3), the orbital parameters show a certain cyclicity and constancy over time, with the exception of eccentricity and semi-major axis, which are decreasing. However, considering that the mission would take some time to complete, slight variations in the calculations were taken into account. In fact, in parallel with the optimization of the trajectory, a Keplerian propagation of the parameters shown in the table (4.3) was performed for a period equal to that required for the spacecraft to approach the debris. The new final condition is summarised in the following table (4.6) and plotted in figure (4.4) and (4.5) for both the first and second convergence phases, as will be detailed in the next chapter.

Table 4.4: Final debris orbital elements after propagation.

Orbit	a [km]	e [/]	i [°]	Ω [°]	ω [°]	ν [°]
Final debris 1	$R_\oplus$+783	0.009085	98.7250	121.418	16.40	233.25
Final debris 2	$R_\oplus$+782.663	0.009068	98.7245	121.418	16.33	72.08

This analysis revealed that, during the ascent and approach phase of the spacecraft to the target, the latter undergoes a slight loss of altitude, with a reduction in the semi-major axis of about 2 km. The other parameters remain almost unchanged, with the exception of a minor change in the periapsis argument ω. Since the mission completion times differ for the two convergence phases studied, it is to be expected that the arrival anomalies, i.e., the time at which the satellite will intercept the debris, will be different. As an anticipation of what will be discussed later, the approach adopted for the study, through the reduced transversality conditions described in section 3.6, provided that the final arrival anomaly, ν_f, was treated as a *free* parameter, allowing the code to determine the final insertion point optimally.

The choice of initial guess time t_{guess} is also non-trivial. If this is too low, the spacecraft will not have enough time to reach the targeted orbit and, as a result, the code will most likely return an all-positive $\mathcal{S}_F$ in the output, meaning that although thrust is maintained throughout the imposed duration, the goal of reaching the debris is not achieved. On the other hand, if the t_guess is too high, then it would result in mission times longer than necessary, which would perhaps involve additional thrust phases or excessive coasting phases that would

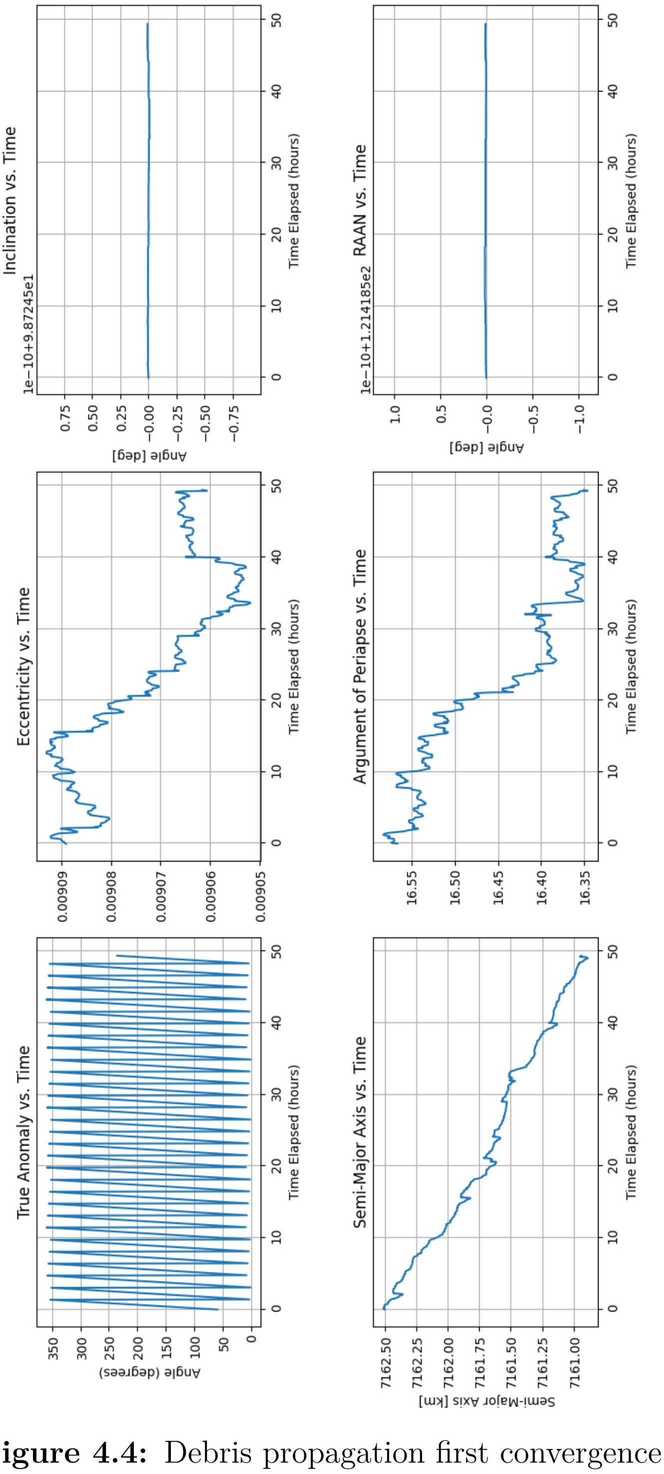

Figure 4.4: Debris propagation first convergence.

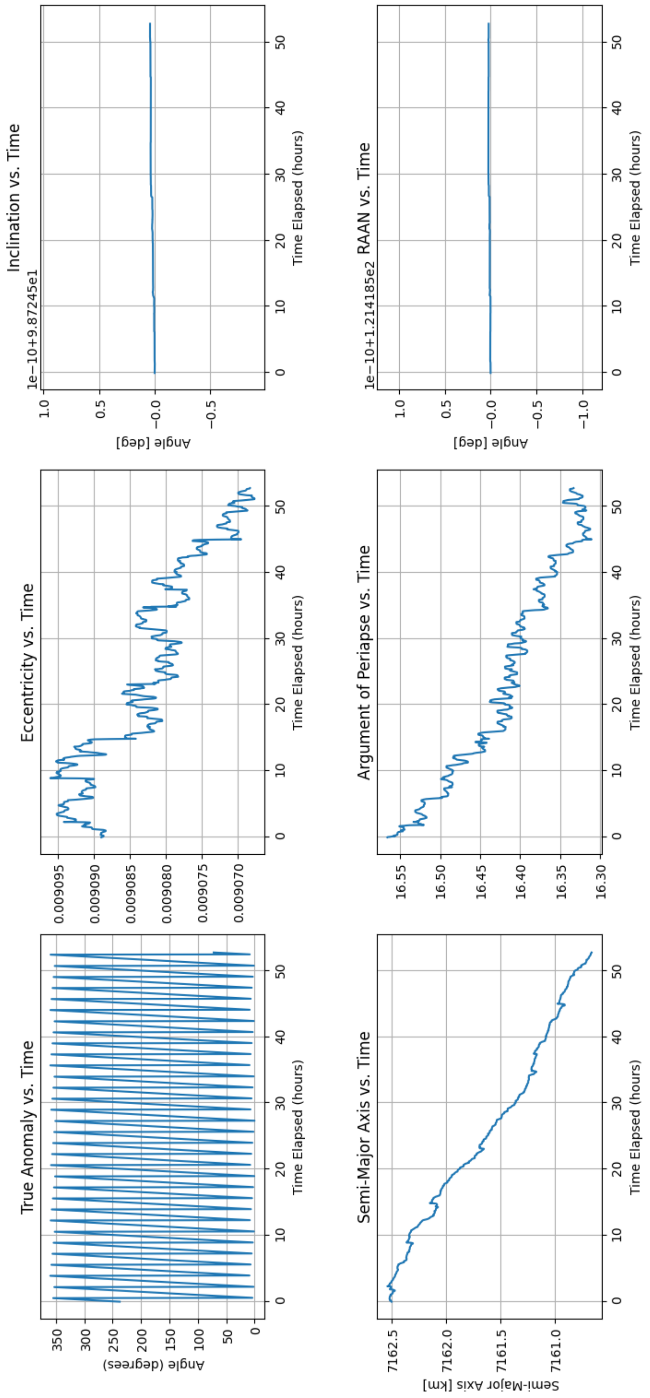

Figure 4.5: Debris propagation second convergence.

not make the mission as a whole efficient. What can be done a priori, then, is to set the thrust T and carry out the mission with continuous thrust until the target is reached. The time taken to trace this ‘spiral’ will constitute the lower limit of the mission: for example, if this strategy takes ten days to reach the debris, the real mission cannot last less since, in reality, there will surely be coasting phases that will dilute the total time. Once this lower limit is determined, one can slowly increase it by trying to converge the solution to lower the $\mathcal{S}_F$ overall by coasting.

As can be deduced from these last observations, there were two strategies on which the code was played to arrive at a result:

- *Free time - free* ν strategy: used for first row guesses to figure out around which time t_{guess} the code would be placed to seek convergence, as well as at which anomaly the spacecraft would try to fit into the final orbit. Under these conditions, the Jacobian matrix will have dimension 9x9;

- *Fixed time -free* ν strategy: implemented once the t_{guess} tends to settle around a particular value. Essentially, the spacecraft has reached the target, but the code is too sensitive to converge with both parameters free. Then, by fixing the time, it is allowed to search for the optimal true anomaly for insertion into the target orbit. In this second case, as there is no need to compute the final Hamiltonian having fixed the time, the size of the Jacobian matrix will scale to an 8x8, losing the last row and column.

Further information on these two strategies can be found in [**28**].

During the search for the solution, however, a severe problem arose in connection with numerical stability and convergence times, which were the result of the reasonable simplicity of the code developed. The limited computing power and robustness, in fact, did not allow the entire trip to be analyzed: the high sensitivity due to the proximity to Earth and the delicacy of the maneuvers made it necessary to divide the trip into two distinct phases. As mentioned above, the first phase of orbit raising with variation of the global parameters was followed by a second phase in which the inclination and eccentricity of the orbit were varied very carefully. It was precisely the variation of the latter, during the various simulations, that turned out to be what made convergence very sensitive and slow, together with the variation of RAAN (the way in which it was dealt with, however, has already been discussed in the previous section).

As a result, the problem was converted from a TPBVP to an MPBVP, with the two phases described representing two distinct mission arcs. This operation proved to be extremely useful for the reasons described and for the computational advantages derived from it, as well as favoring a greater understanding of the code's response to the input, making it plainer.

Finally, the last remark concerns the perturbations that have been included in the dynamic model described in the chapter 2. The issues addressed up to this point have already shown that the code developed is extremely sensitive to more or less complex variations from initial to final state. This led to the decision not to include the perturbations related to the non-sphericity of the Earth and atmospheric drag, at least as far as the part of the study concerning the optimization of the transfer is concerned, since this would considerably complicate the differential equations and, not having suitable computing power available, compromise the achievement of a solution. In essence, the problem was approached as a 2BP without perturbations.

Once, however, the debris has been captured, and the de-orbiting of the spacecraft plus debris system is to begin, then these perturbations can be included without any problems. In fact, as will be better addressed in the next chapter, the re-entry will be characterized by a thrust T reduced to 0.02 N continuously directed in the opposite direction to the velocity. Since nothing needs to be optimized at this stage, the equations of motion straightforwardly need to be integrated so the inclusion of the two perturbations within them does not create numerical problems of any kind (they are merely additional terms in the spacecraft dynamics equations). The resulting trajectory will be a *constant downward spiral* until the reaching of a threshold altitude of 100 km (chosen as the point of final atmospheric re-entry) after a given number of days. On the other hand, including atmospheric drag in the re-entry analysis is advantageous, as it is a term that plays into the goal of lowering the system's orbit.

4.3 Non-dimensionalizing values adopted

This subsection discusses the adimensionalization strategy adopted to lighten the code in the calculation process due to the quite marked differences between the various quantities within the Jacobian matrix. If within this matrix there are significant discrepancies between the orders of magnitude of the elements that compose it (for example, between the positions and the velocities) when the rows and columns of the Jacobian are perturbed to operate the differential correction method, this can cause high numerical instability. Instead, dimensionalizing the state variables present to reduce them to numbers with orders of magnitude comparable between them undoubtedly benefits the robustness of the code. In detail, the dimensionless quantities used in the 2BP are:

Referring to the table (4.5), the Earth radius is used to dimensionless render the satellite position components, while the velocity, obviously, is used for the respective three components and evaluated as:

Table 4.5: Non-dimensionalizing values.

Physical constant	Value
Length unit	6378 km
Mass unit	60 kg
Time unit	806.785 s
Velocity unit	7.90545 m/s

$$v_{adim} = \sqrt{\frac{\mu_{\oplus}}{l_{adim}}} \tag{4.2}$$

and corresponds to the first cosmic velocity (since $l_{adim} \equiv R_{\oplus}$).
The time, instead, is calculated according to the expression:

$$t_{adim} = \frac{l_{adim}}{v_{adim}} \tag{4.3}$$

The dimensionless mass, finally, is equal to the initial one, so that the dimensionless value that it can assume is between 0 and 1, with the first representing the case of complete consumption of propellant, while the second with mass is unchanged compared to the starting condition. A sought result will be to try to stay close to the unit to have a low consumption.

4.4 Straightforward LEO transfer example

The example reported here serves to make what was said above understandable and has the purpose of illustrating the results that the method allows to obtain. In particular, a satellite of equal mass to that supposed for the studied ADR mission has been considered, which must make a transfer between two circular orbits in low LEO characterized by the Keplerian parameters:

Table 4.6: Initial and final orbital parameters LEO transfer orbits example.

Orbit	a [km]	e [/]	i [°]	Ω [°]	ω [°]	ν [°]
Departure	$R_{\oplus}$+450	0	0	0	0	0
Target	$R_{\oplus}$+460	0	0.01	0	0	112.53

Also, the engine performances in terms of specific impulse I_{sp} and thrust T remained unchanged compared to the case under analysis. The strategy to pursue the convergence, then, is the same as that described in section (4.2.3), fixing the time at a certain point and leaving the true anomaly free to allow the optimal insertion on the target orbit.

The results obtained are shown below.

The figure (4.6) shows the trends for the first three parameters. First of all, it is specified that the blue sections indicate a phase in which the engine is on and is pushing with a constant thrust T; the red sections, instead, indicate a coasting phase in which the engine is off. In fact, it is observed how there is a rise of the semi-major axis and an increase in the inclination right along the blue sections, while the eccentricity will vary because it is entering more or less eccentric transfer trajectories. However, it is noteworthy to observe how the developed code is able to bring the final eccentricity back to zero, recirculating the orbit again. During the red coasting section, on the other hand, it is clearly seen how the parameters do not undergo variations.

The $\mathcal{S}_F$ trend is indicative of the thrust and coasting phases just observed: it is immediately noticeable how the mass decreases during the former and remains constant during the latter, but the overall reduction is minimal. The graphs of α and β angles are interesting to analyze. The in-plane thrust angle α has an excursion between $\pm 55°$ approximately, meaning that the spacecraft always pushes to climb, with the thrust not aligned with the speed to have short maneuver times. However, the fact of having maneuvers with an average zero α confirms that one is climbing, and this is correct due to increasing the semi-axis and, therefore, the altitude of the orbit. On the other hand, the out-of-plane thrust angle β assumes positive or negative values, approximately $\pm 180°$, depending on where the spacecraft is located: this means that there is a vector composition of the thrust components that is always vertical, useful for changing the inclination. Following this, it is expected that formally similar trends will also be obtained in the case study.

Finally, in the figure (4.9), the entire trajectory performed in this illustrative example is reported.

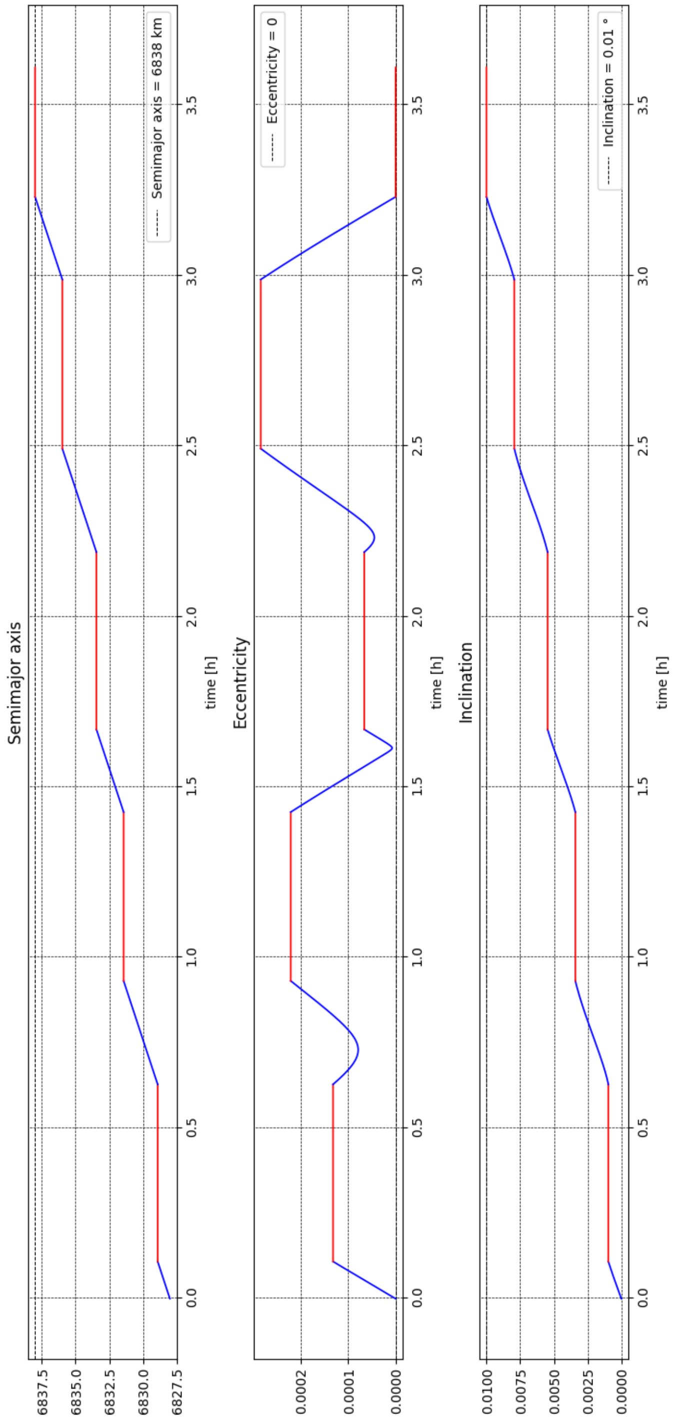

Figure 4.6: Semi-major axis, eccentricity and inclination during the LEO transfer.

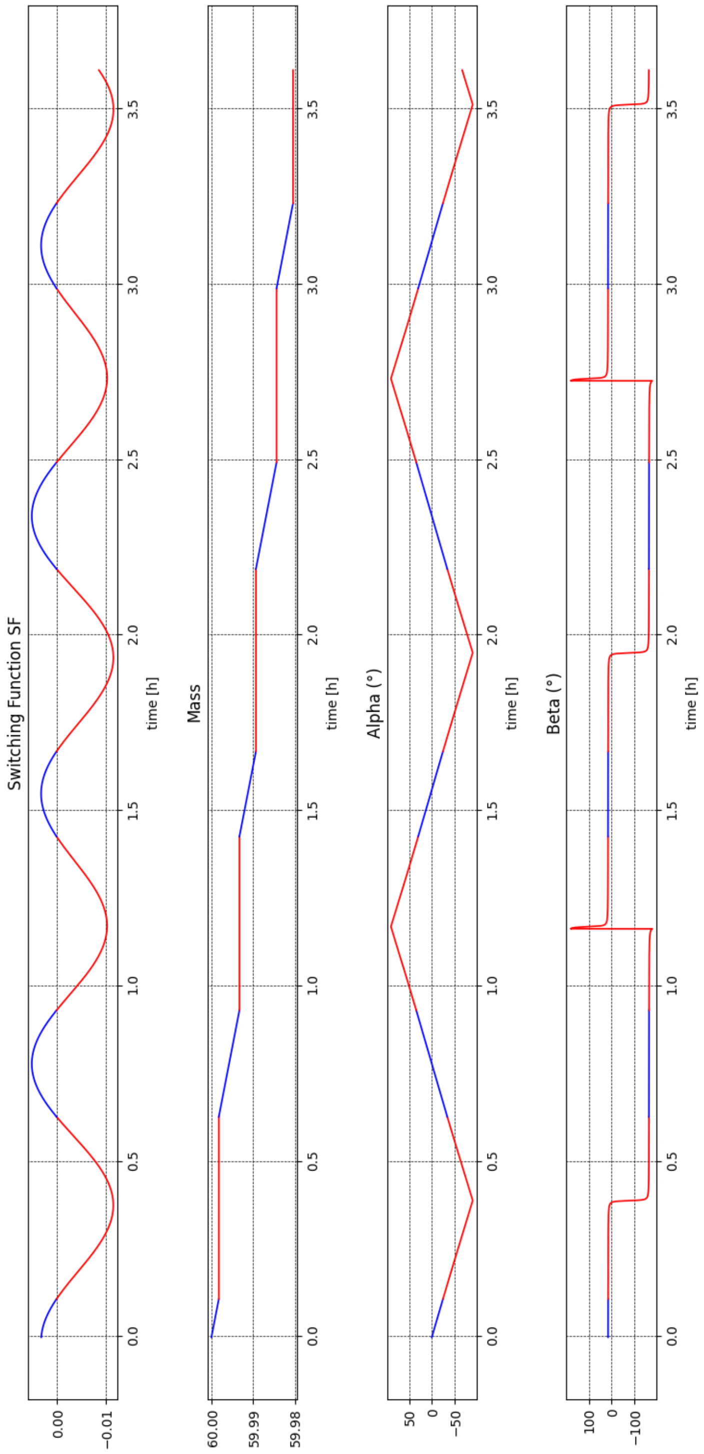

Figure 4.7: $\mathcal{S}_F$, mass, α and β angles during the LEO transfer.

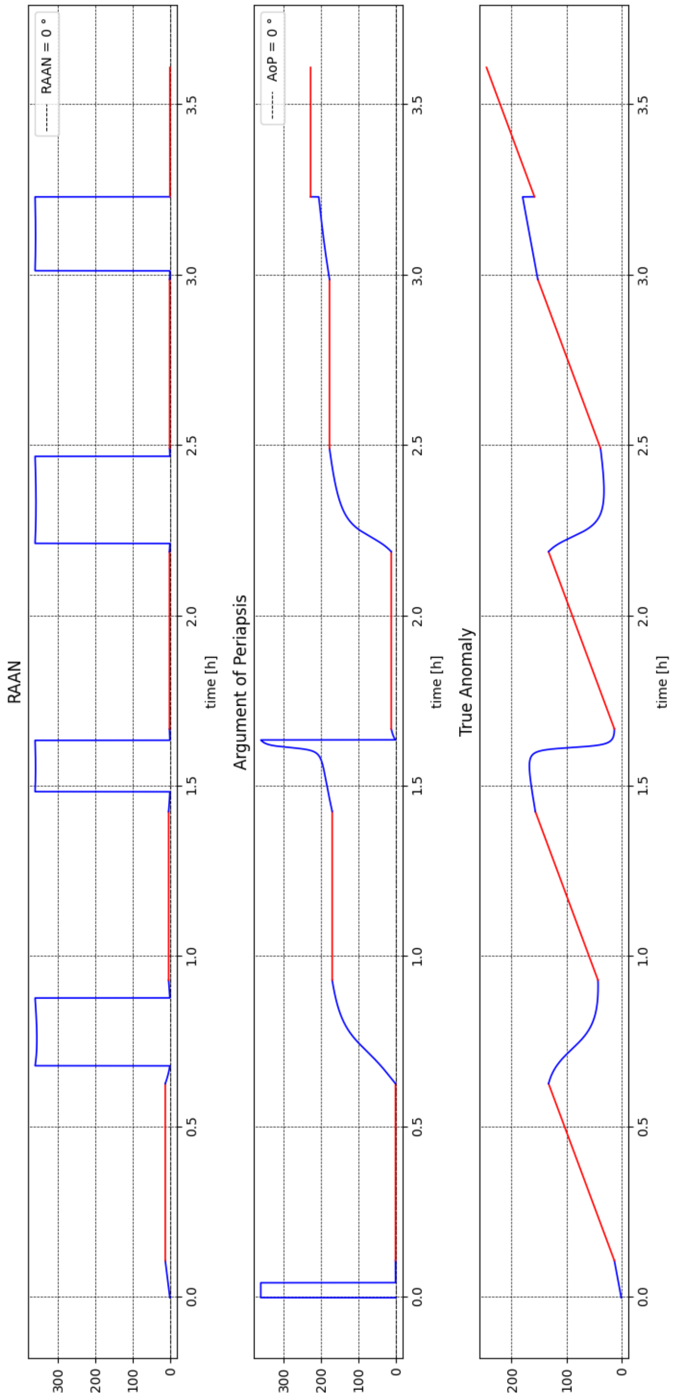

Figure 4.8: RAAN, Argument of Periapsis and true anomaly during LEO transfer.

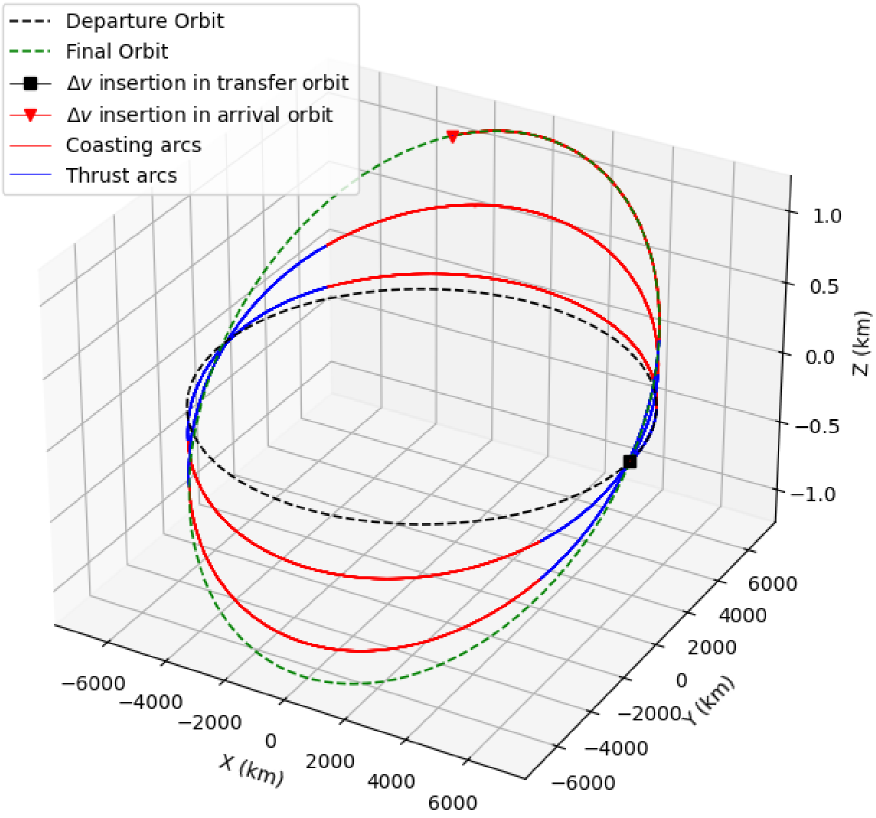

Figure 4.9: Transfer trajectory between the two LEO orbits example.

Chapter 5

Results

Chapter 5 describes all the results of the optimal trajectories obtained from the analysis described in the previous chapter. All trajectories shown below are determined using the 2BP Equations of Motions presented in Chapter 2. Two main sections will be illustrated: the first phase of actual debris targeting and the second phase of debris de-orbiting. Then, in both, two possible convergences of the solution from the periastrum or apoasto of the respective orbits were analyzed. It should be noted in particular, as mentioned earlier, that the first phase of the mission was investigated without accounting the perturbations illustrated in Chapter 2, while the re-entry includes them.

5.1 Trajectories from departure to debris orbit

First of all, the results obtained for the first part of the mission are outlined: by departing from the initial orbit, the target orbit of the debris is reached. For both cases, in addition to the corresponding graphs, the adjoint variables vector of the initial state variables that allowed convergence to be achieved are shown.

The analysis of two scenarios with departures from the two extremes of the line of the apsides derives from the intention to investigate, albeit in a preliminary form, which is the optimal starting point for the beginning of the transfer maneuver. These two specific points were chosen because, in line with the principles of orbital mechanics, it is known that the periastrum represents the position at which the spacecraft reaches maximum velocity, while the apoastro corresponds to the point of minimum velocity. From this perspective, the choice of starting from one or the other could have a significant impact on the overall deltaV required for the transfer maneuver. Similarly to what was mentioned in Chapter 4, in the graphs below, the blue strokes indicate a thrust arc, while the red ones indicate a coasting arc where the engine is off.

5.1.1 Case 1: departure from the perigee

Global orbital parameter variation

This first sub-stage of the transfer is characterized by a maneuver whose purpose is to raise the semi-major axis to the target value, coupled with an analogous variation of the RAAN and the periastrum argument, both of which will be reduced to the final values of the debris orbit to be reached. The transfer is summarised in the following table, showing the initial and final parameters of this first sub-phase.

Table 5.1: Initial Keplerian elements of spacecraft and debris case 1.

Orbit	a [km]	e [/]	i [°]	Ω [°]	ω [°]	ν [°]	m [kg]
Departure	$R_\oplus$+700.14	0.00	97.89	121.50	36.98	346.67	60
Intermediate	$R_\oplus$+783	0.001	98.31	121.42	16.39	225	59.74

The costates values of the state variables that allowed the transfer to be optimally calculated in the table (5.1) are as follows:

$$\Lambda_0 = \{0.100278, 0.360076, 0.079338, 0.476474, 0.136241, 0.252503, 0.994497\}^T$$

It is interesting to point out that among these, the highest value is assumed by λ_u: in essence, at this stage, when a large variation of the orbit semi-major axis a (gaining approximately 83 km) must be performed, the code prioritizes the acceleration along the outgoing radial direction. This will serve to raise the altitude of the spacecraft. On the other hand, the thus reduced λ_z indicates that, at least in this first mission segment, no importance is given to pushing in the z-direction, or at least it is done to a lesser extent than in the others.

Pushing along z would mean changes in the orbital plane, which, as will be seen, will be emphasized more in the second sub-phase. It is no coincidence, indeed, that fairly modest variations in eccentricity e and inclination i are initially obtained, as can be seen in the figure (5.1).

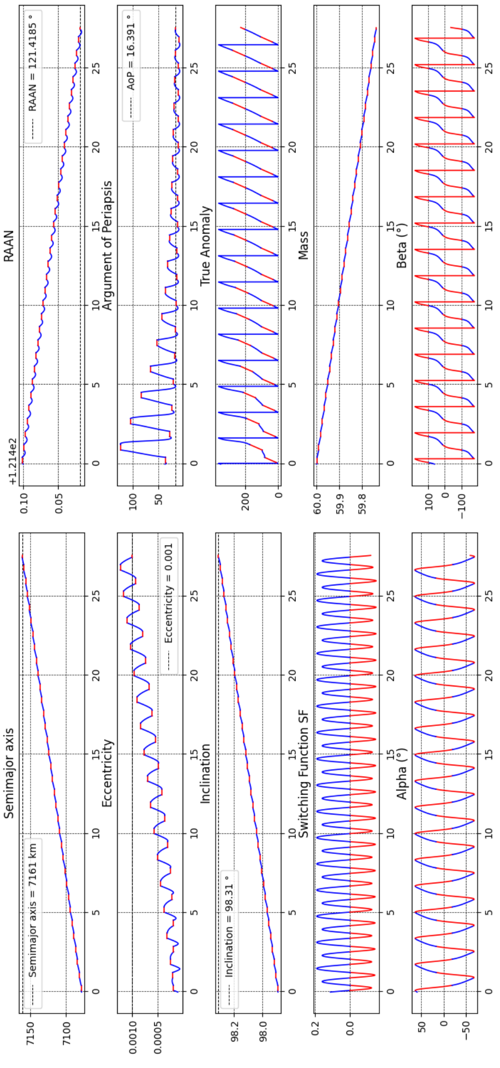

Figure 5.1: Keplerian elements first sub-phase case 1.

The figure (5.1) also confirms what was said in the section (4.4) on the expected trends of the α and β thrust angles, which were discussed in the aforementioned section and not shown here for the sake of brevity. The argument of periastrum and the RAAN, on the other hand, decreases to the final target values.

Rendezvous phase

At the end of the first sub-phase, when the spacecraft has reached the desired altitude, the second one of approaching the debris to capture it takes place. It is specified how, of course, the engagement of the debris will require a certain amount of time for its completion. However, since it is not the purpose of this thesis to study the way this operation takes place, this detail is neglected, assuming that by the time the spacecraft reaches the debris, this activity will be completed in a reasonably short time. The final parameters to be reached are those in the first row of the table (4.6). The maneuver will act on the orbital parameters of the spacecraft as shown in the figure (5.2).

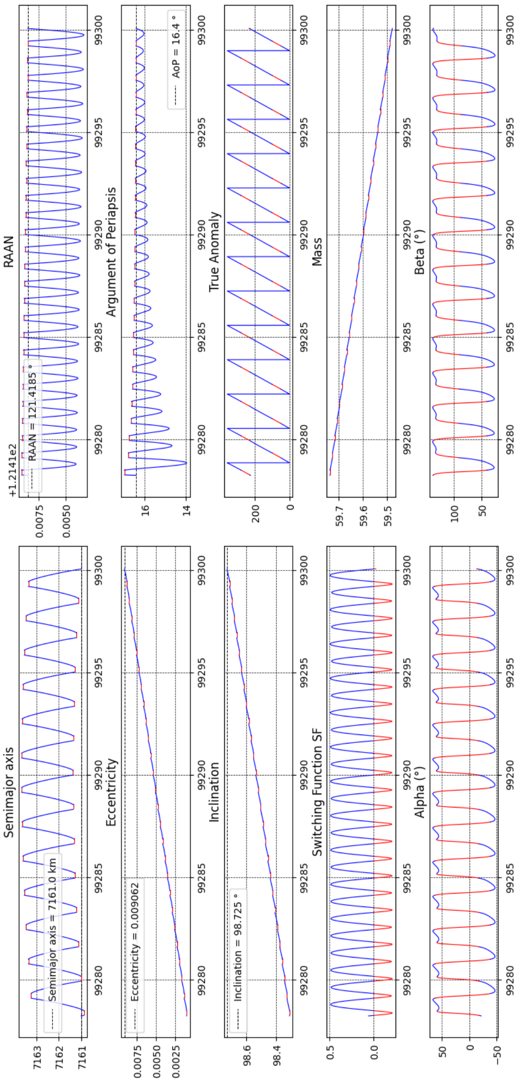

Figure 5.2: Keplerian elements second sub-phase case 1.

Thus, starting from the initial state of the previous sub-step, the method realizes that to obtain the desired eccentricity e and inclination i variations, it needs to change its transfer strategy. In fact, the in-plane α and out-of-plane β thrust angles not only have different trends than before (e.g., β now remains positive until the rendezvous is complete), but also the ranges of values they assume during the thrust phase differ from what was seen previously. A cross-check of the $\mathcal{S}_F$ thrust arcs with the trend of the true anomaly shows how the thrust phases are located at the periastrum and apoastro, which is typical when a maneuver characterized by a large eccentricity variation must be performed.

Then, it is interesting to note the behavior of the semi-major axis a: even though the mission target value has already been reached, the code realizes that it is necessary to maneuver with small altitude overshoots for the spacecraft to vary eccentricity and inclination (and at the same time insert itself at the optimum anomaly ν in the final orbit). These small variations, for the same reason, also affect the RAAN and the argument of periastrum.

The vector of adjoint variables, in this case, will obviously be different:

$$\Lambda_0 = \{-0.487872, -0.348960, 0.249497, -0.185183, -0.345693, 0.311743, 0.992669\}^T$$

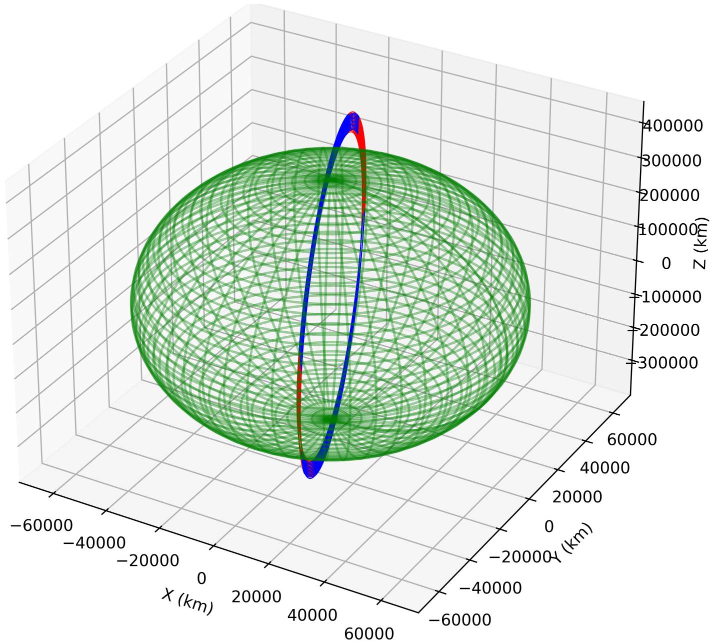

Figure 5.3: Case 1 transfer trajectory.

and notice how importance is also given to the direction of thrust along z, so as to tilt the orbital plane of the trajectory to the desired value. Focusing precisely on velocities, it is evident from the figure (5.4) that the performed rendezvous allowed the debris to be reached with the same velocity components, rightly intercepting it.

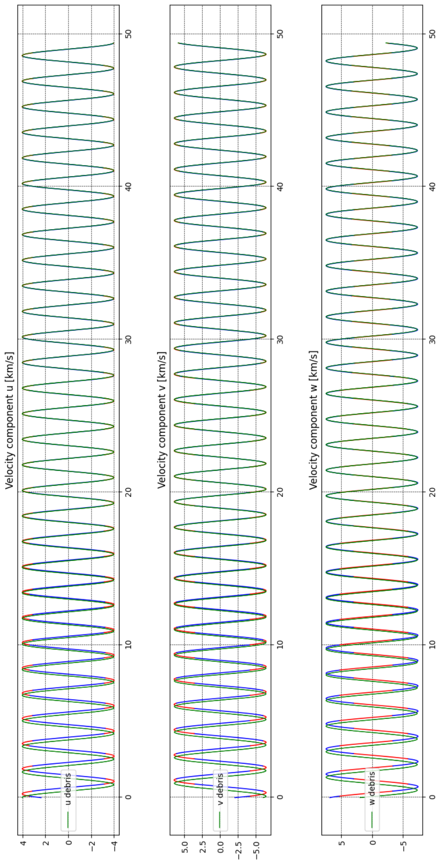

Figure 5.4: Evolution u, v, w during strategy case 1.

Finally, the complete trajectory that the spacecraft followed in this first convergence is shown in the figure (5.3)[1], although one is aware that the plot is not very exhaustive as the spirals of the trajectory are nested together.

Appendix B then shows the complete graphs of the entire mission with the two sub-phases executed in sequence. Finally, the trend of the spacecraft's vector radius with respect to the debris radius has also been plotted (5.5): it is suggestive to observe how, as the spacecraft gradually intercepts the debris, with the trajectories overlapping qualitatively in a similar way to the velocities in the figure (5.4).

---

[1] Please note how, to visualize the trajectory minimally more clearly, a scaling factor along z of value $z_{scale} = 55$ was applied to "stretch" the nested spirals.

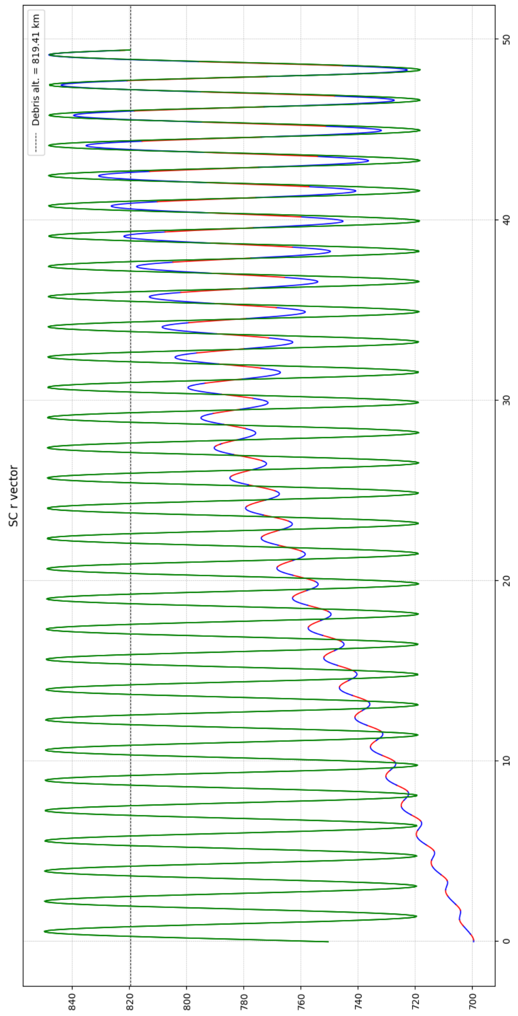

Figure 5.5: Spacecraft case 1 vector radius trend.

The total travel time for Case 1 is $t_1 = 177843.12157$ s $= 49.40087$ h.

5.1.2 Case 2: departure from the orbit apogee

Global orbital parameter variation

In the second case, the procedure remains the same as before, so for the sake of brevity and clarity, it is avoided to repeat the same observations as above. Starting now from the apoastro of the departure orbit, however, the spacecraft is slower on average than before: it is therefore expected that the code will search for a different transfer strategy from the previous one, downstream of which it is then possible to make a comparison between them. In this case, therefore, the transfer is summarised by the table (5.2) below.

Table 5.2: Initial Keplerian elements of spacecraft and debris case 2.

Orbit	a [km]	e [/]	i [°]	Ω [°]	ω [°]	ν [°]	m [kg]
Departure	$R_\oplus$+700.14	0.00	97.89	121.50	36.98	160	60
Intermediate	$R_\oplus$+783	0.0015	98.35	121.42	16.39	34.39	59.72

It is readily apparent that since the mission strategy is different, the final propellant mass will also be different. The initial costates by which convergence was achieved for this sub-phase are:

$$\Lambda_0 = \{-0.064272, -0.301608, -0.041476, -0.461037, -0.196718, -0.180862, 0.994332\}^T$$

What instantly stands out are the negative values of the adjoint variables associated with the positional coordinates x, y, and z and the three velocity components. In summary, the code realizes that the starting position, compared to the first convergence, is not advantageous, so it immediately tries to find a more convenient position from which to raise the semi-major axis of the orbit. This can also be seen from the radically different trends of the two thrust angles α and β, shown in the figure (5.6), together with the trends of the other parameters.

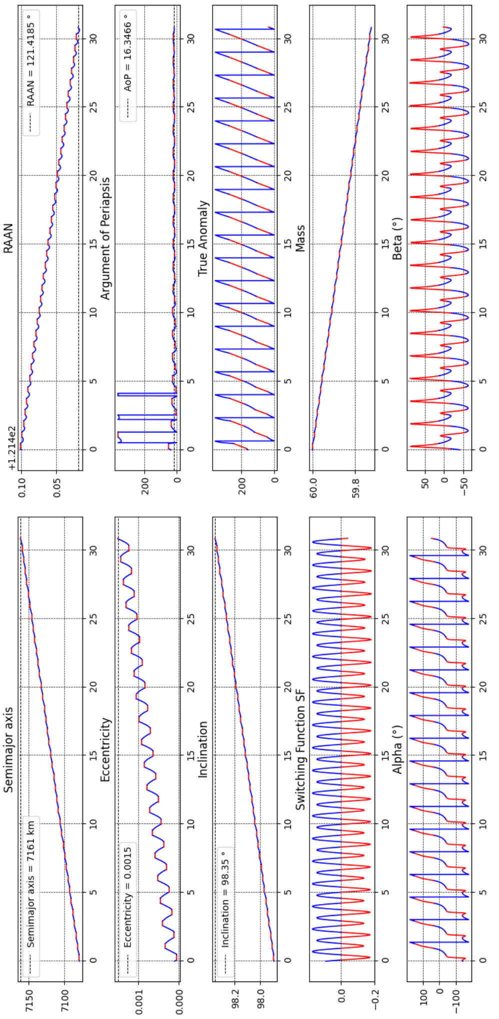

Figure 5.6: Keplerian elements first sub-phase case 2.

Except for the two angles, the trends follow the same philosophy as described above, with the only notable difference being the rather abrupt way in which the argument of the periastrum is brought down, undergoing a sharp reduction.

5.1.3 Rendezvous phase

As before, once the first sub-phase is completed, the outputs produced are entered as initial conditions for carrying out the second sub-phase leading to the debris. Again, the time required for the effective capture of the debris is disregarded.

The final parameters to be achieved are those shown in the second row of the table (4.6).

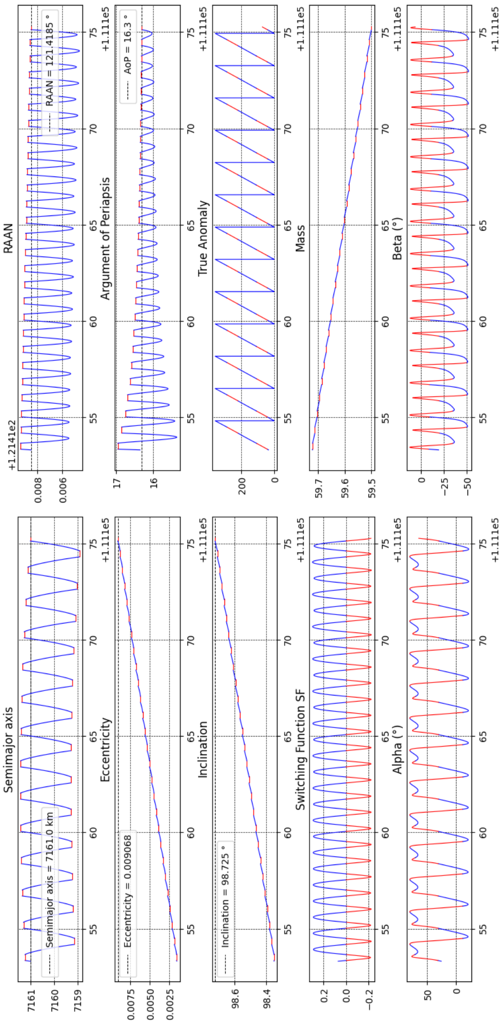

Figure 5.7: Keplerian elements second sub-phase case 2.

The figure (5.7) shows what was seen for the rendezvous sub-phase of the first convergence: to be able to vary eccentricity and inclination, the code is forced to gently modify the semi-axis to maneuver, this time decreasing it slightly with each impulse. The argument of the periastrum and the RAAN follow the same trends, while the in-plane angle α and the out-of-plane angle β vary entirely from the previous strategy, with the latter always being negative when the engine is turned on. In this case, the costates vector found iteratively is as follows:

$$\Lambda_0 = \{0.372786, 0.270152, 0.083657, 0.466328, 0.049123, 0.207423, 0.994669\}^T$$

The values are markedly different from those associated with the first convergence, demonstrating the difference between the two mission strategies pursued by the code by simply varying the starting point with the same end conditions to be achieved and propulsive performance. Again, the trends of the three velocity components with their gradual overlap with the debris velocity components are plotted in the figure (5.8), indicating the correct completion of the rendezvous.

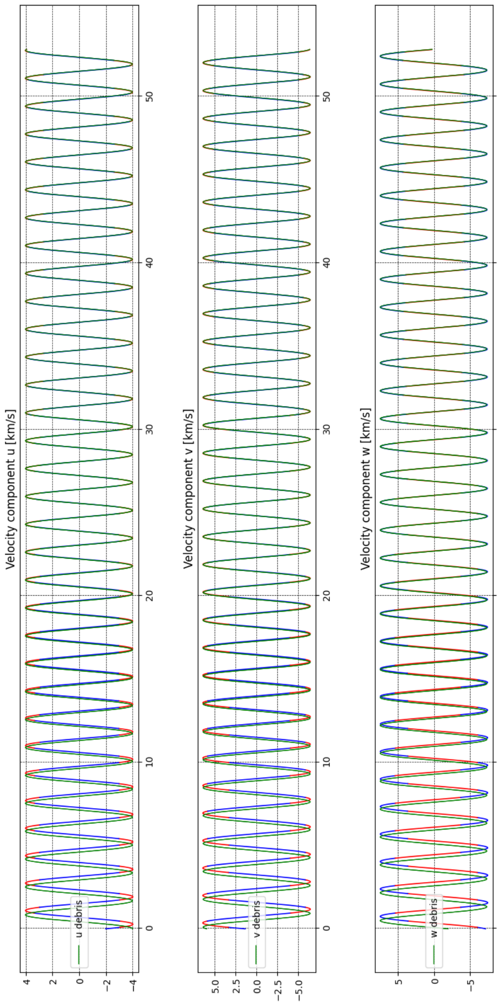

Figure 5.8: Evolution u, v, w during stratergy case 2.

The complete trajectory of the transfer determined by the second convergence is shown in the figure (5.9).

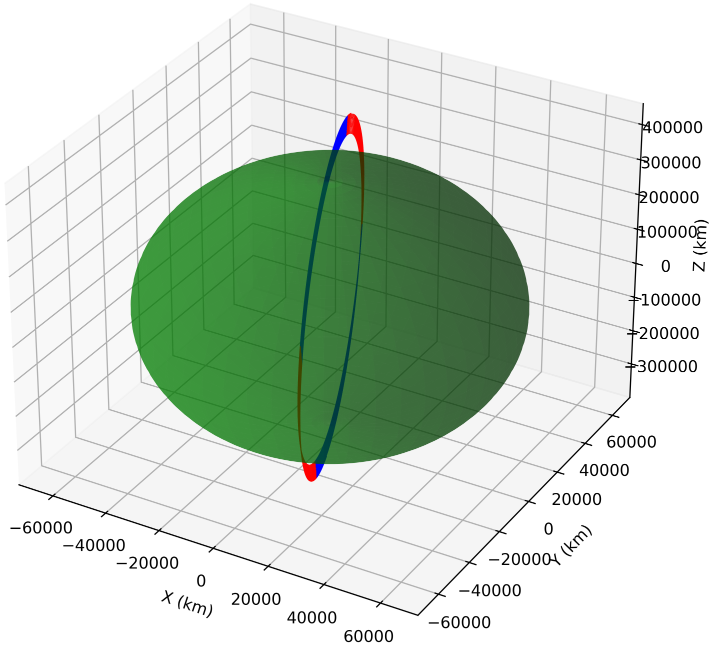

Figure 5.9: Case 2 transfer trajectory.

The trend of the spacecraft vector radius compared with that of the debris (5.10) is also formally identical to that seen before.

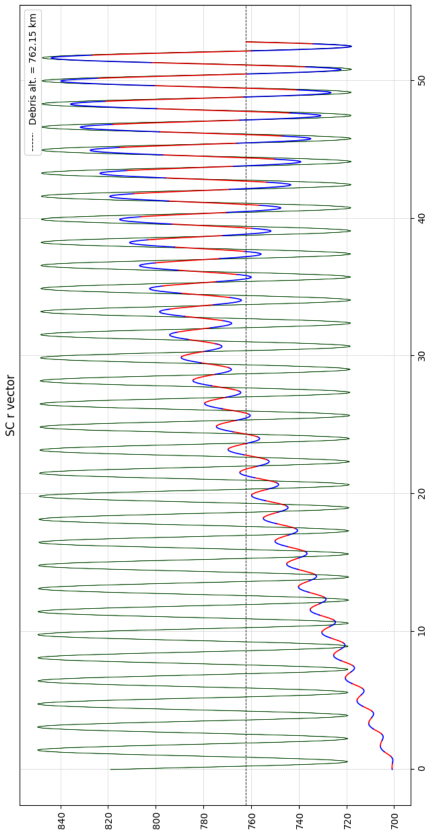

Figure 5.10: Spacecraft case 2 vector radius trend.

The total travel time for Case 2 is $t_2 = 190150.005943$ s $= 52.81944$ h. Appendix C shows the graphs obtained by running the two codes in succession with each other to plot the complete mission trends.

5.2 Deorbit manoeuvre from debris orbit

Once the spacecraft has intercepted the debris, the second part of the mission takes over, namely that of deorbiting it, following the various regulations discussed in Chapter 1. First of all, it should be noted that the altitude to which the debris must be reduced for it to be considered re-entered into the atmosphere has been set at 100 km.

As mentioned earlier, moreover, this final stage does not involve optimization of any kind, which is why the determination of the trajectory will be the product of a simple integration of the problem's equations of motion. In addition, however, there will be perturbative contributors related to the non-sphericity of the Earth J2 and the atmospheric resistance D, both of which do not complicate the computational calculation. Therefore, the respective acceleration components that are added to those already present in the system are given here: for J2, one has

$$a_{J2x} = \frac{3}{2} J2 \mu_{\oplus} \frac{r^2}{\bar{r}^4} t_x$$

$$a_{J2y} = \frac{3}{2} J2 \mu_{\oplus} \frac{r^2}{\bar{r}^4} t_y$$

$$a_{J2z} = \frac{3}{2} J2 \mu_{\oplus} \frac{r^2}{\bar{r}^4} t_z$$

dove:

$$\bar{r} = \sqrt{x^2 + y^2 + z^2}$$

$$t_x = \frac{x}{\bar{r}} \left(\frac{5z^2}{r^2 - 1} \right)$$

$$t_y = \frac{y}{\bar{r}} \left(\frac{5z^2}{r^2 - 1} \right)$$

$$t_z = \frac{z}{\bar{r}} \left(\frac{5z^2}{r^2 - 3} \right)$$

Whereas for drag D one has:

$$a_D = -\frac{1}{2} \cdot v_{rel} \cdot \bar{v}_{rel} \cdot \rho \cdot C_D \cdot \frac{A}{m}$$

with v_{rel} relative velocity of the spacecraft with respect to the Earth's rotational velocity at the point where it is located and $\bar{v}_{rel}$ the norm of relative velocity. In addition, there are two other coefficients within the expression:

- The drag coefficient C_D, which is a dimensionless parameter used to quantify the drag of an object moving within a fluid. A typical reference value of 2.2 was chosen;

- The area of the exposed front surface A. In this case, the maximum cross-section of the debris of 4.41 m^2 was selected as the reference value. In reality, the contribution of the area of the spacecraft should also be taken into account in this term, but it is modeled here as a point mass: as a first approximation, since the mass of the debris is higher than the spacecraft one, this assumption can be considered valid.

Thus, for the de-orbiting analysis, the information needed is summarised in the table (5.3).

Table 5.3: Parameters characterising de-orbiting.

	Case 1	*Case 2*
C_D	2.2	2.2
A	4.41 m^2	4.41 m^2
Deorbiting altitude	100 km	100 km
Initial mass	159.48 kg	159.50 kg
Perturbations	J2 and D	J2 and D

Finally, since there is no interest from either a fuel economy or a timing point of view in deorbiting the debris in the immediate future, the thrust value T of the motor was lowered from 0.08 N to 0.02 N. Therefore, the direction of T is kept constantly in the opposite direction to the velocity, allowing for a braking effect: as a result, the kinetic energy of the spacecraft will decrease and the orbit, overall, will lower, losing energy.

5.2.1 Case 1: departure from the orbit periastrum

Assuming that the initial state of the system consists of the debris plus spacecraft combination, one first case is studied in which the deorbiting *Deltav* is given at the periastrum of the orbit. The motivation behind this is similar to that described for the first part of the mission: namely, to investigate whether the different initial velocity at the time of the first maneuvering impulse can subsequently define one strategy better than another. By setting the propagator with the information and data discussed in the previous section, the results obtained are reported below. Since the time required to reach the lower limit altitude is longer than in the first part of the mission, the trends of the orbital parameters in the figure (5.11) will be intricate and cannot be clearly distinguished. The figure (5.12) zooms in on these trends to better show the fluctuations that the elements undergo due to both deorbit and the influence of perturbations.

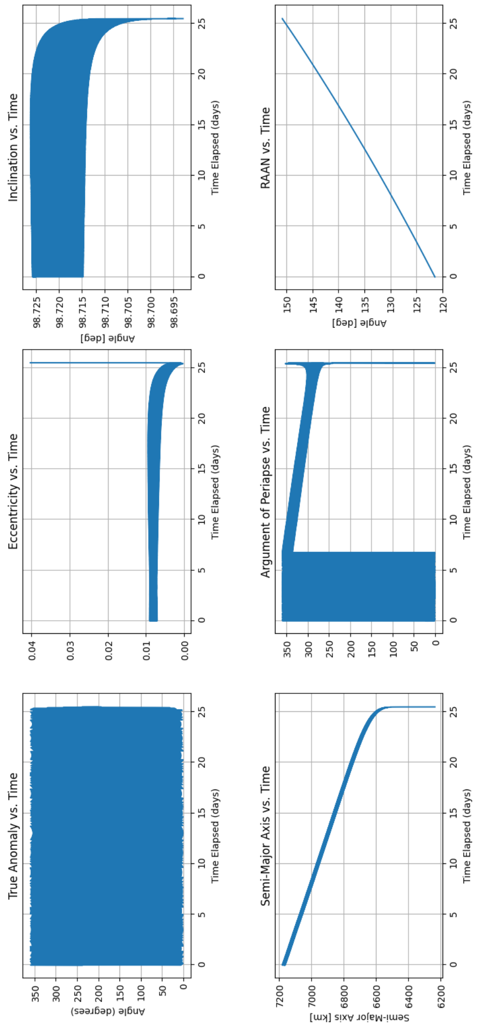

Figure 5.11: Keplerian elements during case 1 deorbiting.

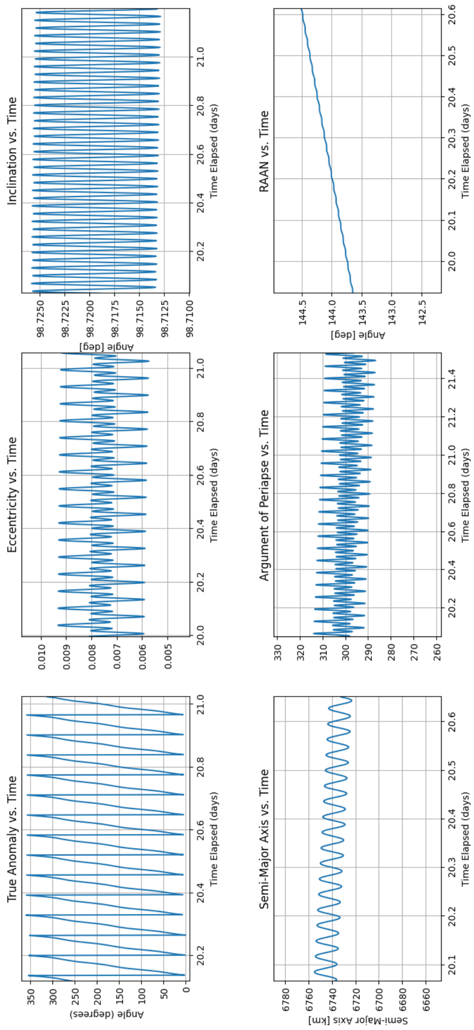

Figure 5.12: Zoomed Keplerian elements during case 1 deorbiting.

Due to the contribution of drag, the semi-major axis gradually decreases with small oscillations. Eccentricity is also subject to quite noticeable fluctuations that initially keep it roughly constant at the starting value. Later, when the drag contribution becomes significant at the lower altitudes, the trajectory decays much more rapidly and turns strongly eccentric, which explains the immediate vertical asymptote at the end of the graph. Interesting to observe, then, the influence of J2 on the trends of RAAN and periastrum argument: net of slight fluctuations for both, the effects of regression of the node line are evident, as the periastrum argument decreases globally, and that of the precession of the line of the apsides, with the RAAN increasing (no longer having control over how the orbital plane should be oriented in space, this will vary uncontrollably under the effect of the forces present within the dynamic model). All this leads to a rather intricate and somewhat complex deorbiting trajectory in the figure (5.13).

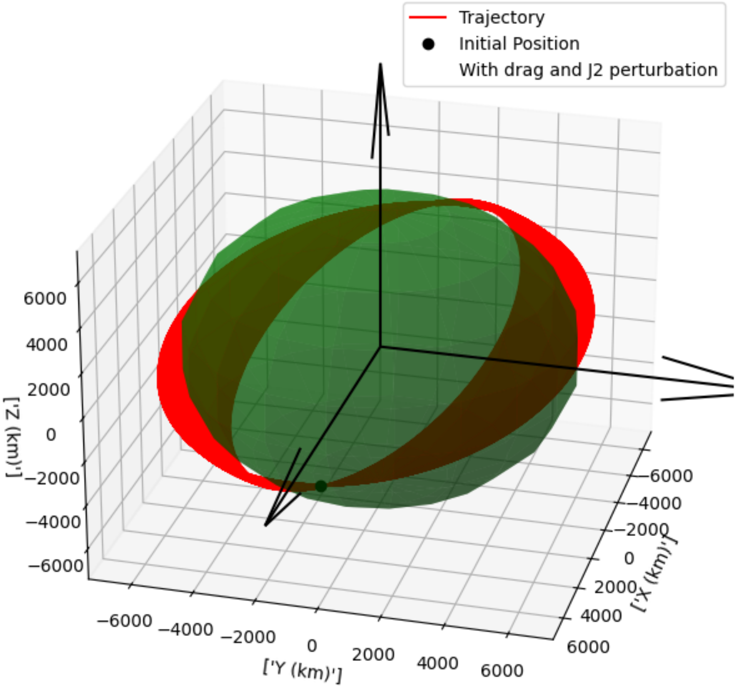

Figure 5.13: Deorbit trajectory case 1.

The 100 km altitude at which the debris is considered to have re-entered the Earth's atmosphere is reached approximately 26 days after departure. In the figure (5.14) it is shown how, cyclically, during this time interval, the periastrum and apostro of the orbit will gradually lower until they even take on a negative value, signifying that a suborbital ellipse has been reached, which will lead the system to crash into the ground in the future.

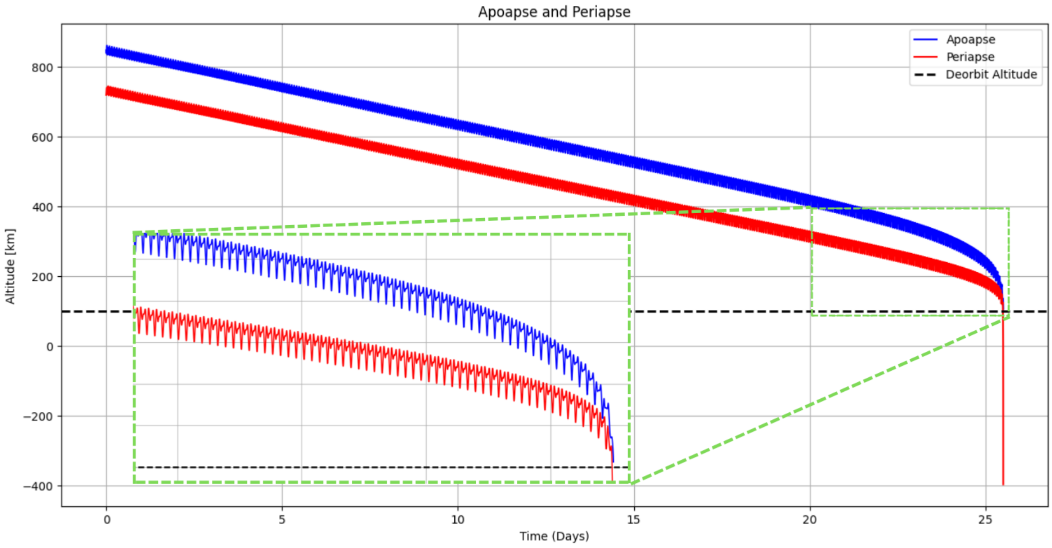

Figure 5.14: Periastrum and apoastro trend during case 1 deorbiting.

In a qualitatively similar way, the same trend associated with the altitude of the orbit can be traced, as shown in the figure (5.15).

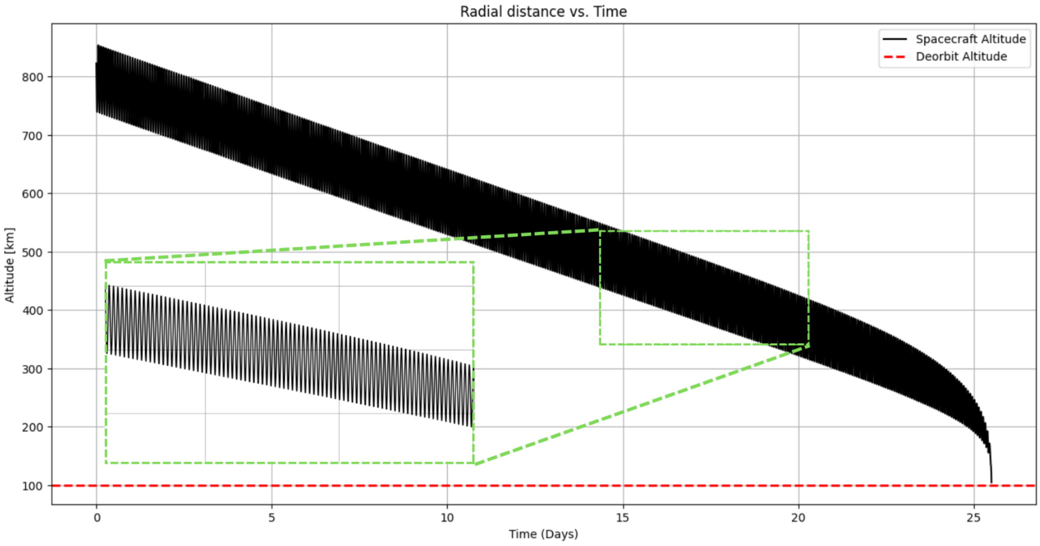

Figure 5.15: Spacecraft plus debris altitude during case 1 deorbiting.

Thus, the spacecraft plus debris system gradually loses more and more altitude until a sudden decay below 300 km, where the density begins to be higher, and the braking contribution from atmospheric drag becomes increasingly relevant.

5.2.2 Case 2: departure from the orbit apoastro

The dual case to the previous one is now studied: always assuming the system to be composed of spacecraft plus debris, the deorbiting trajectory is investigated this time if the Δv impulse to do so is initially given at the orbit apoasto, where the system is slower. All other conditions being equal, the evolution to reach the target altitude will be slightly different from the former. Propagating the equations of motion, the trends of the orbital parameters for this second case are as shown in the figure (5.16), with (5.17) showing a zoom in detail to capture the fluctuations related to the perturbations.

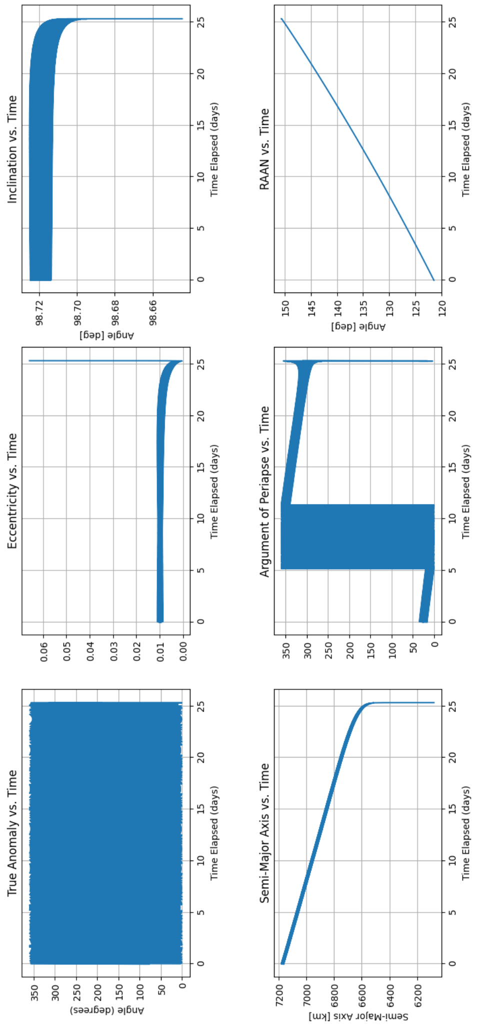

Figure 5.16: Keplerian elements during case 2 deorbiting.

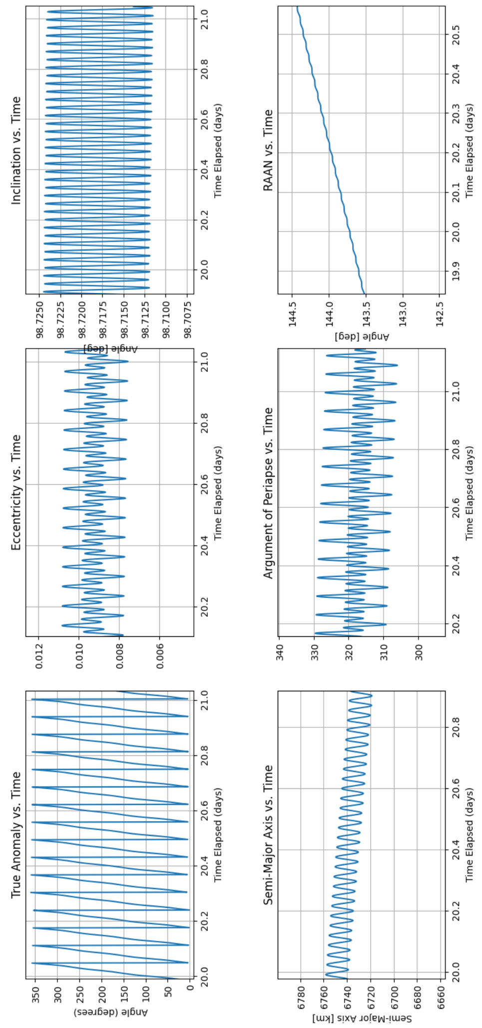

Figure 5.17: Zoomed Keplerian elements during case 2 deorbiting.

The patterns shown are formally identical to those (5.11), and the same considerations are valid, which are not shown here to avoid repetition and confusion. There are also no significant observations to be made for the trajectory derived from integration, as it is very similar to that seen for case 1.

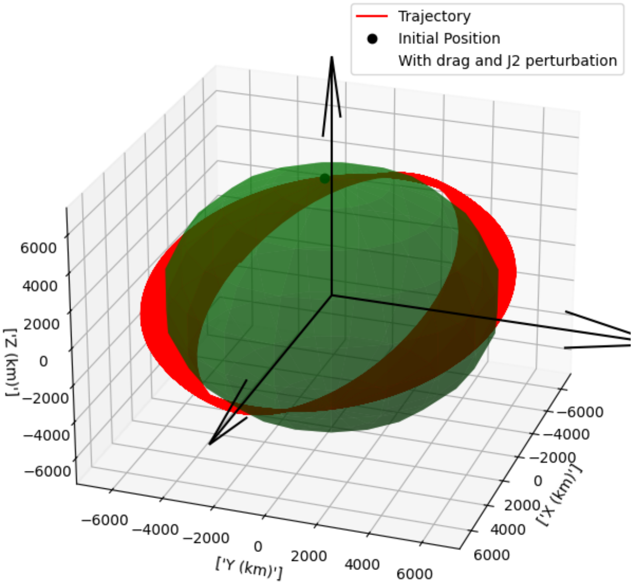

Figure 5.18: Deorbit trajectory case 2.

Even with this strategy, the debris will return to the atmosphere after a period of approximately 26 days. Consequently, this result showed that case 1 and case 2 are interchangeable in terms of timing, with neither proving to be advantageous over the other. This is also evident from the behavior of the periastrum and apoastro over time (5.19) and of the altitude of the spacecraft plus debris system (5.20), which are essentially identical to those of case 1.

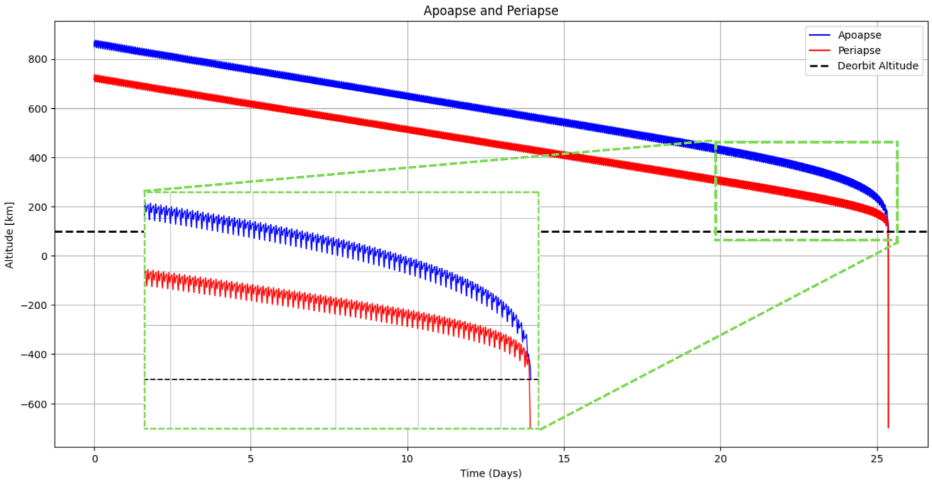

Figure 5.19: Periastrum and apoastro trend during case 2 deorbiting.

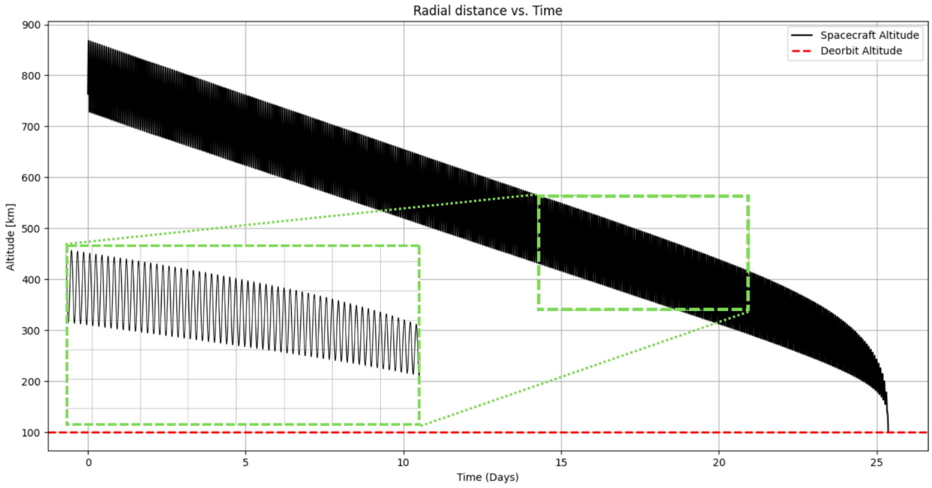

Figure 5.20: Spacecraft plus debris altitude during case 2 deorbiting.

The same considerations as above apply to both.

Chapter 6

Concluding remarks

This thesis serves as a starting point or preliminary study for a possible feasibility analysis of an Active Debris Removal (ADR) mission to the Sun-Synchronous Orbit (SSO) region through the formulation of a low-thrust minimum-propellant trajectories problem in a discretely simple 2-body dynamical model. The growing interest of the scientific community in the potential of exploiting SSO orbits is one of the aspects of interest in the work produced. Together with this, the potential of this work, if applied, in contributing to the creation and realization of an environmentally sustainable space environment and improving the sustainability of access to space is one of its main strengths.

Downstream of the results obtained and the analyses performed, the primary objective of the work carried out to develop an optimization and propagation code in the Python language, based on the use of an indirect method, can be regarded as widely achieved. Precisely, this class of numerical methods proved to be the most appropriate for solving the Hamiltonian Boundary Value Problem (HBVP) arising from the application of the Optimal Control Theory (OCT) to the space trajectory optimization problem. Pontryagin's Maximum Principle (PMP) was instrumental in defining the optimal control strategies necessary for minimizing propellant consumption. Given the particularly delicate nature of indirect methods, this criticality was addressed by strengthening the analysis, which was achieved by dividing the mission into two phases and defining a Multi Point Boundary Values Problem (MPBVP). In this context, the initial attempt values were determined through an iterative procedure, with the primary objective of maximizing the final mass of the spacecraft, thereby minimizing the propellant consumption required to complete the proposed mission.

Considering the pioneering nature of the topic under discussion, it is evident that in order to fully understand the potential of a mission scenario towards a SSO, such as the one examined, in-depth analysis and study of the dynamics of such orbits and missions is indispensable. This approach is fundamental not only to acquire a deeper awareness of the specific characteristics of these trajectories but also to refine and perfect the optimization methodologies of the trajectories aimed at reaching this orbital region, with the goal of improving the overall efficiency of the mission and guaranteeing the optimal use of available resources.

The study conducted showed, based on the two convergences obtained for the ascent phase towards the target debris, how both allow the mission to be completed while respecting all the constraints and boundary conditions imposed. Both mission case 1 and mission case 2 investigated lead to substantially identical propellant consumption, with the former characterized by a final mass of 59.48 kg and the latter by a final mass of 59.50 kg: from the consumption point of view, neither strategy prevails over the other. In detail, however, scenario 1, where the first Δv is delivered at the departure orbit periastrum, leads to the completion of the targeting phase in a time of about 49 h. The dual scenario with departure at the apoastro, on the other hand, takes slightly longer, lasting around 53 h to reach the final orbit of the selected debris. From a mission timing perspective, therefore, Case 1 would seem to be the optimal one to pick.

Even from the deorbiting standpoint, there is no difference in choosing a departure from the periastrum rather than from the apoastro of the orbit since, in both solutions, the system consisting of debris plus spacecraft will decay into the atmosphere at an altitude of 100 km in about 26 days, with the same propulsive performance of the chosen engine. Obviously, according to the section analyzing this phase, optimizing propellant consumption for deorbit is not of interest, which is why the final mass with which the system will arrive at the threshold altitude will not be a discriminating factor in choosing one strategy over the other. Deeper analysis, perhaps, might reveal the convenience of when and where to initiate the deorbiting maneuver, taking into account a possible phasing with an uninhabited zone to which the system will re-enter.

6.1 Future research

Although the objectives set before this thesis work were broadly achieved, after the study was completed, various possibilities for further developments were investigated, thanks to which the analysis carried out could be improved further. First of all, it was realized during the development of the code and the subsequent convergence study that one of the main limitations was the reduced computing power available to perform the various analyses, which stretched the time required to find a solution, as well as not allowing the implementation of a more complex and faithful dynamic model than the one used. Consequently, it is immediately apparent that with higher computing power, together with the use of correct numerical stability techniques, there would have been no need to split the trajectory into two sub-phases, but it would have been possible to simulate and optimize the entire journey. This would have allowed a discrete reduction in the time required to find the initial guesses for convergence, as only one set of initial guesses had to be determined in this hypothesis.

From the dynamic model's point of view, on the other hand, this also translates into the possibility of analyzing the transfer starting from the initially set RAAN before adopting the trick seen, simulating the commissioning phase to arrive at the actual RAAN from which to depart with the first mission Δv. Linked to this, the possible stiffening and stabilization of the code would have opened up the possibility of including additional perturbations within the dynamic model, such as solar radiation pressure or the effect of the third body, to increase its fidelity.

Finally, observations can also be made concerning re-entry, which can be used as a starting point for further investigation. In particular, once the 100 km altitude at which the return had been set has been reached, two strategies could be pursued:

1. Feasibility study on other possible debris that can be reached with the residual propellant in the vicinity of the orbital region where the system decays at an altitude of 100 km. If this strategy were to be followed, then one would speak of a multi-retrieval debris mission;

2. De-orbiting the spacecraft into the atmosphere together with the captured debris. This rather delicate phase must be carefully investigated to comply with international regulations on satellite re-entry, which must take place over unpopulated areas. An interesting tool that could be used to conduct this study would be ESA Debris Risk Assessment and Mitigation Analysis (DRAMA).

Appendix A

Euler-Lagrange equations

$$
\begin{aligned}
\frac{d\lambda_x}{dt} &= \left(\frac{\mu_\oplus}{r^{3/2}} - \frac{3\mu_\oplus}{r^{5/2}}x^2\right)\lambda_u\left(\lambda_v y + \lambda_w z\right) \\
\frac{d\lambda_y}{dt} &= \left(\frac{\mu_\oplus}{r^{3/2}} - \frac{3\mu_\oplus}{r^{5/2}}y^2\right)\lambda_v\left(\lambda_u x + \lambda_w z\right) \\
\frac{d\lambda_z}{dt} &= \left(\frac{\mu_\oplus}{r^{3/2}} - \frac{3\mu_\oplus}{r^{5/2}}z^2\right)\lambda_w\left(\lambda_u x + \lambda_v y\right) \\
\frac{d\lambda_u}{dt} &= -\lambda_x \\
\frac{d\lambda_v}{dt} &= -\lambda_y \\
\frac{d\lambda_w}{dt} &= -\lambda_z \\
\frac{d\lambda_m}{dt} &= -T\frac{\lambda_V}{m^2}
\end{aligned} \tag{A.1}
$$

Appendix B

Transfer Case 1

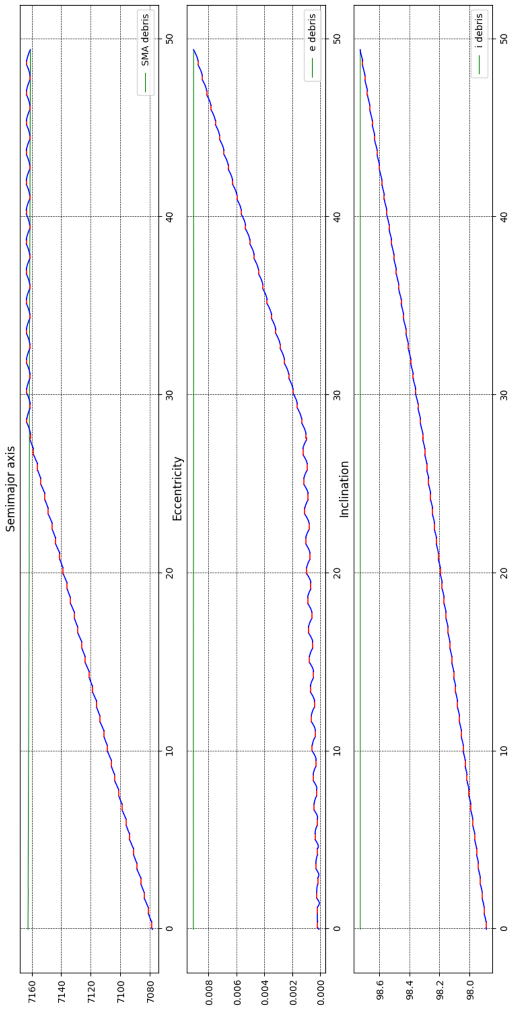

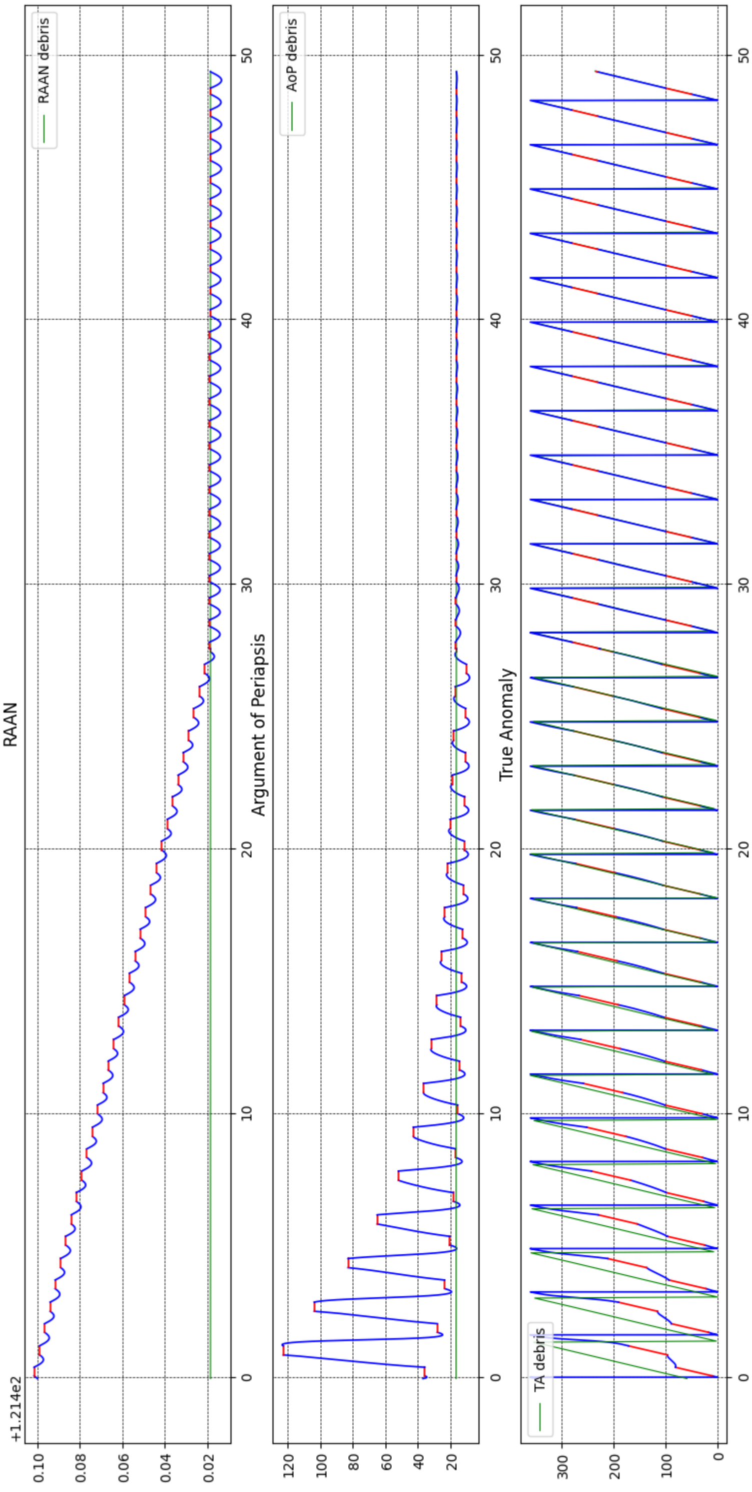
RAAN
RAAN debris
+1.214e2
0.10
0.08
0.06
0.04
0.02
0
10
20
30
40
50
Argument of Periapsis
AoP debris
120
100
80
60
40
20
True Anomaly
TA debris
300
200
100
0

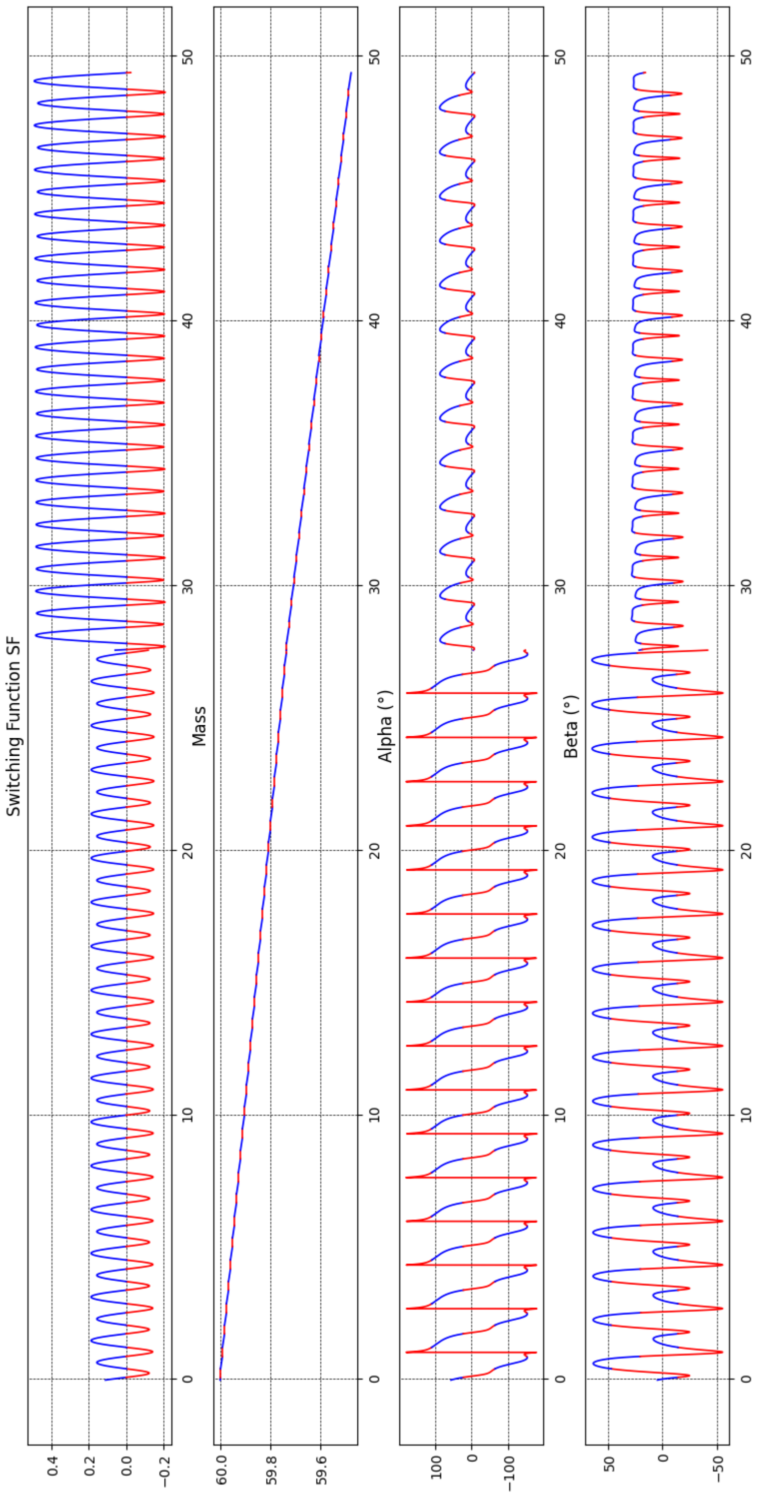
Switching Function SF
0.4
0.2
0.0
−0.2
Mass
60.0
59.8
59.6
Alpha (°)
100
0
−100
Beta (°)
50
0
−50
0
10
20
30
40
50

Appendix C

Transfer Case 2

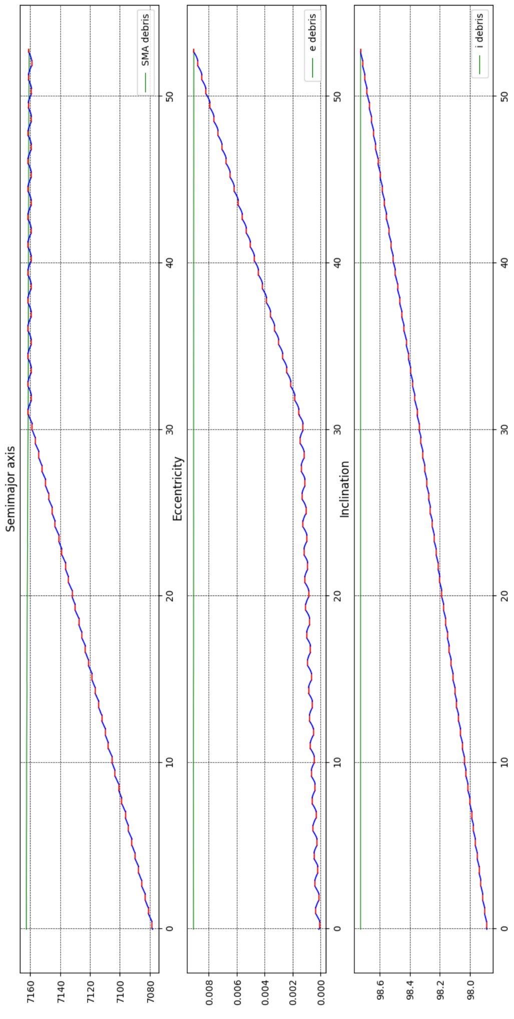

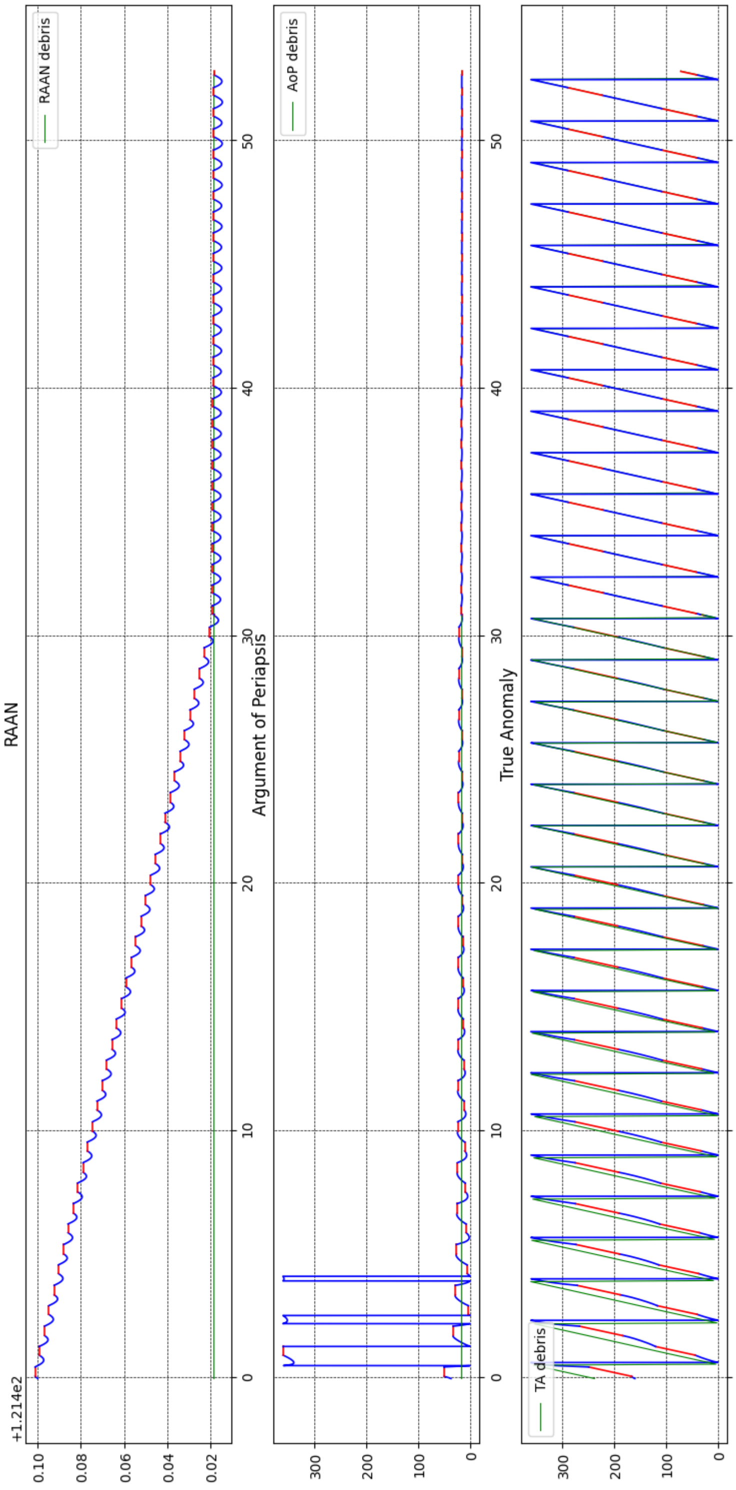
RAAN
RAAN debris
+1.214e2
0.10
0.08
0.06
0.04
0.02
Argument of Periapsis
AoP debris
300
200
100
0
True Anomaly
TA debris
300
200
100
0
0
10
20
30
40
50

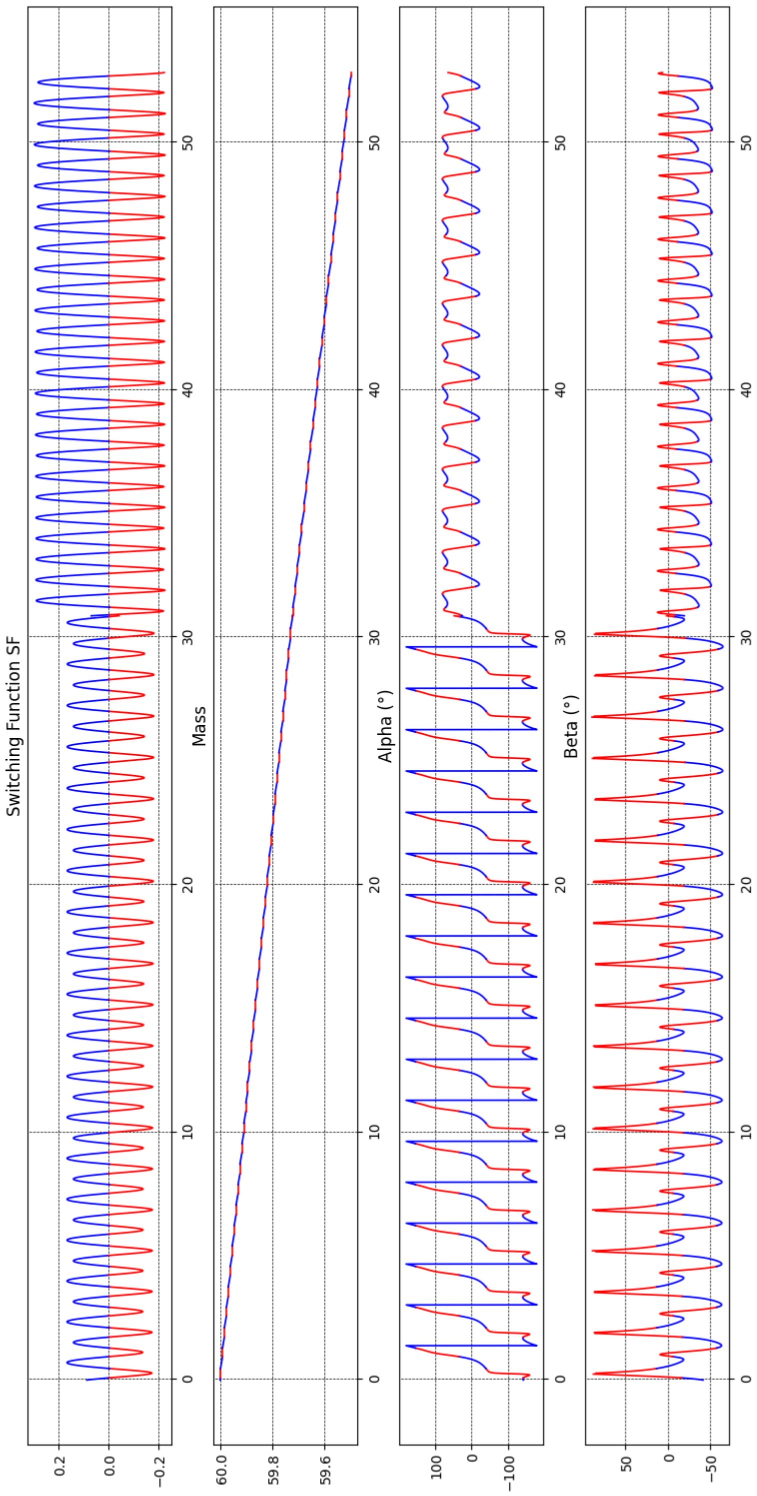
Switching Function SF
0.2
0.0
−0.2
Mass
60.0
59.8
59.6
Alpha (°)
100
0
−100
Beta (°)
50
0
−50
0
10
20
30
40
50

Bibliography

[1] Flury, Walter. *The space debris environment of the earth.* Earth, Moon, and Planets 70.1 (1995): 79-91.

[2] National Aeronautics and Space Administration (NASA), *State-of-the-Art of Small Spacecraft Technology*, URL `https://www.nasa.gov/smallsat-institute/sst-soa/deorbit-systems/`, (13 Feb 2024): 382-386. (Retrieved: 25-03-2024).

[3] Macauley, Molly K. *The economics of space debris: Estimating the costs and benefits of debris mitigation.* Acta Astronautica 115 (2015): 160-164.

[4] Flury, W. *European activities on space debris.* Second European Conference on Space Debris. Vol. 393. 1997.

[5] WG, ESA Space Debris Mitigation, *ESA Space Debris Mitigation Compliance Verification Guidelines*, ESA, (14 Feb 2023): 21.

[6] Hakima, Houman, and M. Reza Emami. *Prioritizing orbital debris for active debris removal missions.* 2017 IEEE Aerospace Conference. IEEE, 2017.

[7] ESA Space Debris Office, *ESA's Annual Space Environment Report*, ESA, (12 Sep 2023), `https://www.sdo.esoc.esa.int/environment_report/Space_Environment_Report_latest.pdf`

[8] Rex, Dietrich. *Space debris mitigation and space systems design.* Acta astronautica 41.4-10 (1997): 311-316.

[9] Betts, John T. *Survey of numerical methods for trajectory optimization.*, Journal of guidance, control, and dynamics 21.2 (1998): 193-207.

[10] Kuhn, Harold W., and Albert W. Tucker. *Nonlinear programming.* Traces and emergence of nonlinear programming. Basel: Springer Basel, 2013. 247-258.

[11] Pontryagin L., *In Mathematical Theory of Optimization Processes.* CRC Press Raton, 1962.

[12] Rao, Anil V. *A survey of numerical methods for optimal control.* Advances in the astronautical Sciences 135.1 (2009): 497-528.

[13] Betts, John T. *Practical methods for optimal control and estimation using nonlinear programming.* Society for Industrial and Applied Mathematics, 2010: 127-129.

[14] Conway, Bruce A. *A survey of methods available for the numerical optimization of continuous dynamic systems.* Journal of Optimization Theory and Applications 152 (2012): 271-306.

[15] Morante, David, Manuel Sanjurjo Rivo, and Manuel Soler. *A survey on low-thrust trajectory optimization approaches.* Aerospace 8.3 (2021): 88.

[16] *Acta eruditorum*, Volume 15, Christoph Günther, 1696

[17] Martins, Joaquim RRA, and Andrew Ning. *Engineering design optimization.* Cambridge University Press, (2021): 33-45.

[18] Mascolo, Luigi. *Low-Thrust Optimal Escape Trajectories from Lagrangian Points and Quasi-Periodic Orbits in a High-Fidelity Model.* PhD thesis, Diss. Tesi di dott. Torino: Politecnico di Torino, 2023.

[19] Bryson, Arthur Earl., and Ho Y.C. *Applied optimal control: optimization, estimation and control.* Taylor and Francis Group (1975): 214.

[20] Vinter, Richard. *Optimal control and Pontryagin's maximum principle.* Encyclopedia of systems and control. Cham: Springer International Publishing, 2021. 1578-1584.

[21] McDanell, James Phillip, and William Francis Powers. *Necessary conditions joining optimal singular and nonsingular subarcs.* SIAM Journal on Control 9.2 (1971): 161-173.

[22] https://pypi.org/project/numbalsoda/

[23] Lawden, D.F. *Optimal Trajectories for Space Navigation*, Butterworths, London, 1963.

[24] Pan, Binfeng, et al. *Reduced transversality conditions in optimal space trajectories.* Journal of Guidance, Control, and Dynamics 36.5 (2013): 1289-1300.

[25] SPACE-TRACK.ORG, `https://www.space-track.org/#catalog`.

[26] DISCOSweb, `https://discosweb.esoc.esa.int/objects/39159`.

[27] Zhao, Shuge, et al. *Target sequence optimisation for multiple debris rendezvous using low thrust based on characteristics of SSO.* Astrodynamics 1 (2017): 85-99.

[28] Sarcletti, Giacomo, *Indirect optimization of low-thrust collision avoidance trajectories in LEO with bang-bang control laws.* Diss. Politecnico di Torino, 2024